X-ray and Electron Spectroscopy of the Chemical and Electronic Structure of Ga_2O_3 – Bulk, Surfaces, and Interfaces

Zur Erlangung des akademischen Grades einer
DOKTORIN DER NATURWISSENSCHAFTEN (Dr. rer. nat.)

von der KIT- Fakultät für Physik des

Karlsruher Instituts für Technologie (KIT)

angenommene

DISSERTATION

von

M.Sc. Elizaveta Pyatenko

Tag der mündlichen Prüfung: 15.12.2023

1. Referent: Prof. Dr. Tilo Baumbach

2. Referent: Prof. Dr. Clemens Heske

Declaration of Authorship

I herewith affirm that I wrote the current thesis on my own and without the usage of any other sources or tools than the cited ones and that this thesis has not been handled neither in this nor in equal form at any other official commission.

Erklärung der Selbstständigkeit

Hiermit versichere ich, die vorliegende Arbeit selbstständig angefertigt zu haben und keine Hilfsmittel jenseits der kenntlich gemachten verwendet zu haben. Weiterhin habe ich weder diese noch eine äquivalente Version dieser Arbeit bei einer anderen Prüfungskommission vorgelegt.

Ort, Datum   Unterschrift

Eggenstein-Leopoldshafen, den 01.11.2023

Abstract

In this thesis, the chemical and electronic structure of Ga_2O_3 is investigated by means of electron and x-ray spectroscopic techniques. Ga_2O_3 has a wide bandgap (4.4 - 4.9 eV), which means that it does not absorb visible light. It belongs to two classes of materials: the ultrawide-bandgap (UWBG) semiconductors, and the transparent conductive oxides (TCOs). The wide bandgap and optical transparency make Ga_2O_3 attractive for usage in a variety of applications, e.g., in electronics and photovoltaics.

In the multilayer structure of $Cu(In,Ga)Se_2$ (CIGSe)-based thin-film solar cells, a buffer layer is needed for the formation of a p-n junction, as well as to separate the absorber from the transparent front contact. Ga_2O_3 has shown promising potential as buffer layer material, offering several advantages, including its high bandgap for reduced visible light absorption and in-vacuum processability for optimal integration in an inline solar-cell production process. Understanding the chemical structure of this layer and its interface with the absorber is crucial for further optimization of the device performance of the corresponding thin-film solar cells. In the first part of this thesis, the chemical structure of the interface between a sputter-deposited Ga_2O_3 buffer layer and the CIGSe absorber prepared with a state-of-the-art RbF postdeposition treatment, is studied in detail. Particular focus is placed on understanding the impact of the RbF postdeposition treatment and an ammonia-based rising step on the chemical structure of the Ga_2O_3/CIGSe interface. Using a combination of synchrotron-based hard x-ray photoelectron spectroscopy (HAXPES), and laboratory-based x-ray photoelectron spectroscopy (XPS) and x-ray excited Auger electron spectroscopy (XAES), a detailed and depth-varied picture of the chemical structure is painted. It is found that the ammonia-based rinse has a significant impact on the chemical structure, partially removing Rb and completely removing F, as well as removing Ga-F, Ga-O, and In-O surface bonds, and reducing the Ga/(Ga+In) ratio at the absorber surface. After Ga_2O_3 deposition, the formation of In oxides is identified, and the diffusion of Rb and small amounts of F into/onto the Ga_2O_3 buffer layer is observed.

The electronic properties at the surface, i.e., the positions of the valence band maximum (VBM) and conduction band minimum (CBM) with respect to the Fermi level (E_F), the band alignment

at the Ga_2O_3/CIGSe interface, and the bandgap (E_g), directly influence the charge transport, and hence the efficiencies of devices. Thus, understanding the electronic structure of Ga_2O_3 is equally (if not even more) important as understanding its chemical structure. In the next part of the thesis, the valence bands of three differently prepared Ga_2O_3 surfaces are investigated. The solar cell samples with the highest thickness of Ga_2O_3 were taken as a model of nanocrystalline Ga_2O_3, and β-Ga_2O_3 single crystals were prepared in two different ways: one sample was cleaved under ultra-high vacuum (UHV) to obtain a clean β-Ga_2O_3 single crystal surface, while another underwent a mild Ar^+-ion treatment to introduce defects, such as oxygen vacancies to the surface. By measuring the valence bands for all three samples with photoelectron spectroscopy (PES) at a wide range of photon excitation energies (70 eV - 6.3 keV), both the surface and the near-bulk electronic structure of the samples could be investigated. Density functional theory (DFT)-based calculations were performed for β-Ga_2O_3, for a better understanding of the experimental results. While the VBM for the UHV-cleaved β-Ga_2O_3 is determined as 4.8 ± 0.1 eV, independent of the photon excitation energy, the VBM of the nanocrystalline Ga_2O_3, and the Ar^+-ion treated β-Ga_2O_3 single crystal samples are significantly different depending on whether the bulk or the surface is being probed. Strong tails in the VBM of the surface-sensitive measurements, likely induced by surface defects, and a downwards shift of the VBM from E_F with increasing photon excitation energy, likely due to surface adsorbate-induced band-bending, are observed in the latter two samples.

In the last part of this thesis, the electronic structure of the bulk of the β-Ga_2O_3 single crystals are studied by means of x-ray emission spectroscopy (XES), x-ray absorption spectroscopy (XAS), and resonant inelastic x-ray scattering (RIXS) at the oxygen K edge. β-Ga_2O_3 is highly anisotropic, so its optical and electronic properties are expected to change depending on the orientation of the crystal with respect to the polarization of the incoming x-ray beam. Polarization-dependent measurements allow to selectively excite different regions within the band structure as well. Thus, polarization-dependent measurements were performed by rotating differently oriented β-Ga_2O_3 single crystals with respect to the incoming x-ray beam. In addition to DFT calculations for the ground state, calculations for the excited system with a core/valence exciton in XAS and RIXS were performed using the Bethe-Salpeter Equation (BSE) method. The BSE calculations are able to capture all the main features of the calculated spectra correctly. There are clear differences in the measured spectra depending on the polarization direction,

which are all reproduced in the calculated spectra as well. Evidence for core-exciton formation are observed in all the experimental RIXS spectra. Finally, an electron-photon scattering lifetime could be determined from the RIXS spectra as 3 ± 2 fs, in agreement with literature results.

Contents

1. Introduction

The immense progress in electronics over the last 70 years would not have been possible without the invention of the transistor by John Bardeen, Walter Brattain, and William Shockley in 1947, for which they received a Nobel prize in 1956.[1] The ubiquitous use of semiconductor devices in nearly all modern electronics means that the search for new semiconductor materials, as well as the improvement of existing semiconductors continues to be a very active and exciting area of research. One of the most important parameters characterizing the optical and electronic properties of a semiconductor is its bandgap (E_g), the minimum energy required to promote an electron from the valence to the conduction band. Currently, the most commonly used semiconductor is Si, with a bandgap of 1.12 eV,[2] followed by GaAs, with a bandgap of 1.42 eV.[3]

Semiconductors with a wide bandgap can operate at higher temperatures, voltages, and frequencies than their Si counterpart, expanding their uses dramatically. While wide bandgap semiconductors such as GaN (bandgap 3.4 eV[4]) have been extensively studied, a rather new area of research is to investigate the ultrawide-bandgap (UWBG) semiconductors, defined as having a bandgap larger than 3.4 eV.[4] Some UWBG materials are Al-based nitrides, boron nitride, diamond, and Ga_2O_3. Photons must have an energy greater than the bandgap to be absorbed by the material, so wide bandgap semiconductors have reduced (compared to Si) or no absorption in the visible light range. This is particularly important for applications in photovoltaics: in $Cu(In,Ga)Se_2$ (CIGSe)-based thin-film solar cells, light is incident on the front contact (also known as a high-resistive layer), travels through the buffer layer, and is absorbed in the CIGSe absorber. Therefore, absorption of visible light should be minimized in both front contact and buffer layer to maximize absorption in the CIGSe.

Although Ga_2O_3 has been studied for more than 60 years, interest in it was low until the first Ga_2O_3 field-effect transistor (FET) was successfully made in 2011.[5] Since then, in addition to using it as an FET,[5–7] several other applications have been found, including solar-blind UV detectors[8–11] and gas-sensing devices.[12–14] Although it is known that Ga_2O_3 has a wide bandgap, a large range of bandgap values have been reported in literature: 4.4-4.9 eV.[15–21] Ga_2O_3 also belongs to the transparent conductive oxides (TCOs), with a good electrical conductivity and

transparency in the UV- visible light region. Ga_2O_3 must contain charge-transport states at or near the Fermi energy to be a TCO.[22] Taking the bandgap as 4.5 eV, this means that Ga_2O_3 absorbs light of wavelengths < 276 nm. This makes it an attractive candidate for use as a buffer layer or high-resistive layer in CIGSe based thin-film solar cells.[23] It even potentially allows usages in space-based applications.[23, 24]

Most of the applications mentioned above use crystalline β-Ga_2O_3. In comparison to other UWBG materials, such as diamond and Al-based nitrides, large amounts of high-quality β-Ga_2O_3 single crystals have been produced using various growth methods.[26–30] The commercial availability of samples facilitates the study and potential applications of Ga_2O_3. Much of the experimental research has focused on the crystal growth, as well as measuring the optical and electronic properties such as optical absorption (transmittance and reflectance as well)[18,19,31–33], and the transport properties (electrical and thermal conductivity).[31,34–37] Amorphous or nanocrystalline Ga_2O_3 has also found applications in solar-blind UV detectors[11] and gas-sensing devices[12], and an insulator-metal transition has been observed in amorphous Ga_2O_3, with potential applications in storage devices.[38] The goal of this thesis is to elucidate the chemical and electronic structure of Ga_2O_3 by using a variety of electron and x-ray spectroscopic methods.

In the first part of the thesis, the application of thin-films of Ga_2O_3 as buffer layers in $Cu(In,Ga)Se_2$ (CIGSe)-based thin-film solar cells is investigated. Traditionally, CdS is used as a buffer layer in CIGSe-based film solar cells. However, the wet chemical bath used for its deposition is toxic and disrupts the vacuum-based in-line production process. Thus, alternative buffer layers such as In_xS_y,[16,39–42] $Zn(O,S,OH)$,[42–44] $(Zn,Mg)O$,[45–47] $Zn_{1-x}Sn_xO_y$,[48,49] HfO_x,[50] Al_2O_3,[42,51,52] Ga_2O_3,[16,53,54] $Sn_{1-x}Ga_xO_y$,[55] $(In,Ga)_2O_3$,[53] and $(Al,Ga)_2O_3$[53] have been investigated. The industrially-relevant solar cell samples investigated in this thesis were manufactured by the Zentrum für Sonnenenergie-und Wasserstoff-Forschung Baden-Württemberg (ZSW), where sputter-deposited Ga_2O_3 was used as a buffer layer for CIGSe absorbers.

Ultimately, manufacturers of the solar cells focus on the power conversion efficiency, device stability, and cost. For further optimization of the thin-film solar cell devices, a detailed understanding of the chemical and electronic structure of the various surfaces and interfaces in the solar cell is essential. Insights into the chemical structure, such as the effect of surface treatments, and diffusion/segregation processes are important in improving the device

performance. Here, the goal was to shed light on the chemical structure of the CIGSe and Ga_2O_3 surfaces, as well as the Ga_2O_3/CIGSe interface. The CIGSe samples were exposed to a state-of-the-art RbF post-deposition treatment and an ammonia-based rinsing step, as used in corresponding thin-film solar cells. The samples were investigated using laboratory-based x-ray photoelectron spectroscopy (XPS), x-ray excited Auger photoelectron spectroscopy (XAES), as well as synchrotron-based hard x-ray photoelectron spectroscopy (HAXPES). Employing several surface-sensitive photoelectron spectroscopy techniques allows to take advantage of their respective strengths and obtain detailed and complimentary results. By measuring detailed regions of core-level peaks with a wide range of kinetic (and binding) energies, and by using higher excitation energies in HAXPES as compared to laboratory XPS, a depth-resolved picture of the Ga_2O_3/CIGSe interface can be obtained.

Although understanding the chemical structure is important for improving the device performance, the electronic structure at the interface, i.e., the positions of the valence band maximum (VBM) and conduction band minimum (CBM) with respect to the Fermi level (E_F), the band alignment at the interface, and the bandgap (E_g), directly influence the charge transport, and hence the efficiencies of devices. Thus, it is important to investigate the electronic properties of the Ga_2O_3 surface. In the next part of the thesis, the VBM of Ga_2O_3 was investigated in detail. Many factors can affect the electronic structure and hence the VBM and the E_g values, such as the morphology (i.e., whether the Ga_2O_3 is amorphous, nanocrystalline, or a single crystal),[56] the crystal structure (there are five polymorphs of Ga_2O_3),[57] and how the sample surface was prepared (cleaving, any surface treatments such as annealing, Ar^+-ion treatment, or some rinsing procedure)[58–61] .Our group has previously reported defect-induced states responsible for the electrical conductivity in TCOs, which appear as a foot/tail present at the valence band spectral onset.[22] The presence of this "foot" is likely due to surface defect states. It can show up differently in spectra measured at different photon excitation energies, i.e., depending on whether the measurements are more bulk or surface-sensitive. (HAX)PES measurements at the X-SPEC beamline[62] at the KIT synchrotron can be performed at a wide range of photon excitation energies, thus allowing to investigate the role the photon excitation energy can play in the determination of the VB and VBM.

Here, the goal was to understand how the various above-mentioned factors affect the valence band, and for this purpose three different types of samples were investigated: the Ga_2O_3/CIGSe samples described above with the thickest buffer layer, β-Ga_2O_3 single crystals cleaved in ultra-high vacuum, and β-Ga_2O_3 single crystals that underwent a mild Ar^+-ion treatment. The Ga_2O_3/CIGSe samples served as a model of nanocrystalline Ga_2O_3, while one β-Ga_2O_3 single crystal sample was cleaved to obtain a clean surface, and another underwent a mild Ar^+-ion treatment to introduce defects, such as O vacancies to the surface. To obtain depth-varied information, the samples were investigated with (HAX)PES using a wide range of photon excitation energies: 70 eV – 6.3 keV. Density Functional Theory (DFT) calculations were performed to better understand the photon excitation energy dependence of the spectra, and to have a comparison with the measurements for the cleaved β-Ga_2O_3 single crystal.

In the last part of the thesis, the focus was on understanding the bulk electronic structure of the β-Ga_2O_3 single crystals, which was investigated using several x-ray spectroscopic techniques at the O K edge: x-ray emission spectroscopy (XES), x-ray absorption spectroscopy (XAS), and resonant inelastic x-ray scattering (RIXS). Utilizing a combination of x-ray spectroscopic techniques allows to obtain information on both the occupied (XES, RIXS), and unoccupied (XAS, RIXS) electronic states. In addition, XES, XAS, and RIXS are local spectroscopic techniques: the spectral intensities are proportional to the dipole transition matrix elements, which depend on the local geometry, i.e., how the O atoms are bonding with their neighboring Ga atoms (the inequivalent O atoms) in the crystal structure of β-Ga_2O_3, as well as the crystal orientation with respect to the incident x-ray polarization. Due to the anisotropy of the crystal structure of β-Ga_2O_3, one can expect differences in the spectra depending on which inequivalent O atom is excited. By controlling the crystal orientation with respect to the incident x-ray polarization, different regions within the band structure can be probed as well. Thus, in the last part of the thesis, the goal was to explore the polarization dependence through both measured and calculated oxygen K edge XES, XAS, and RIXS spectra. The polarization-dependent measurements could be performed by rotating the samples with respect to the incident x-ray beam. While ground-state DFT calculations were performed for the XES spectra, the Bethe-Salpeter Equation (BSE) method was used in the OCEAN code[63] to calculate the XAS and RIXS spectra with the core and valence excitons taken into account.

The thesis is thus constructed as follows:

Chapter 2 provides the necessary background to understand the underlying theory of this thesis, as well as background on CIGSe solar cells, and the crystal structure, Brillouin zone, and band structure of Ga_2O_3.

Chapter 3 explains the experimental setups that were used for the measurements presented in this thesis.

Chapter 4 presents the study of the chemical structure of the Ga_2O_3/CIGSe interface in thin-film solar cells.

Chapter 5 explores the valence band maxima of different Ga_2O_3 samples.

Chapter 6 presents a polarization-dependent XAS, XES, and RIXS study of the β-Ga_2O_3 single crystals.

Chapter 7 finally summarizes the results of Chapters 4-6, and gives an outlook on potential future work.

2. Background

2.1 Spectroscopic Methods

2.1.1 Electron Spectroscopies

2.1.1.1 X-ray photoelectron spectroscopy

X-ray photoelectron spectroscopy (XPS), originally called Electron Spectroscopy for Chemical Analysis (ESCA), was first developed by Kai Siegbahn and his group in Uppsala, Sweden in the 1950s-1960s,[64–66] for which Siegbahn received the Nobel Prize in Physics in 1981.[67] It is based on the photoelectric effect: the investigated material is irradiated with x-rays, and emits photoelectrons, with kinetic energy E_{kin} given by:

$$E_{kin} = h\nu - E_{bin} - \phi, \tag{2.1}$$

where $h\nu$ is the x-ray photon energy, E_{bin} is the binding energy of the electrons, and ϕ is the work function of the sample. Figure 2.1 shows a schematic of the photoelectric effect.
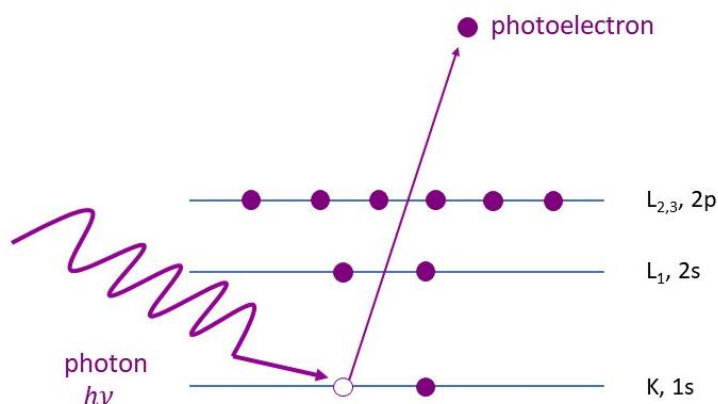
Figure 2.1. Illustration of the photoelectric effect. A photon ejects an electron (from the 1s core level in this case), and a photoelectron is emitted into the vacuum. For simplicity, the spin-orbit splitting of the 2p level is not shown.

Due to the spin-orbit interaction, (i.e., the interaction of the spin with the angular momentum), for all levels with non-zero angular momentum number L, the energy levels will be split into a

doublet; the energy difference between them is known as the spin-orbit splitting. For simplicity, the 2p level in shown without the spin-orbit splitting in Figure 2.1.

Although in equation 2.1, the work function is of the sample, $\phi = \phi_s$, the instrument has its own work function ϕ_i. Because the sample and instrument are in electrical contact, there must be a contact potential $\phi_s - \phi_i$ for equalization of the Fermi level, E_F. Thus, the final kinetic energy recorded is $E_{kin} = h\nu - E_{bin} - \phi_s + (\phi_s - \phi_i) = h\nu - E_{bin} - \phi_i$. This means that the XPS measurements do not depend on the work function of the sample. The work function of the instrument is a fixed constant that is taken into account during the calibration procedure.

In XPS, the spectral intensity is measured as a function of the kinetic energy of the photoelectrons, $I(E_{kin})$. Using equation 2.1, the measured kinetic energies are converted to binding energies, which are given with respect to the Fermi level, E_F (the zero binding energy is set at the Fermi level). Then the intensity is given as a function of the binding energy, $I(E_{bin})$. The binding energies of the electrons are unique to each chemical element, so XPS allows to identify which elements are present in the investigated material.

Typically, XPS is used for measuring solids in various forms such as single crystals, powders, and thin-films. These solids can be metals, semiconductors, or insulators. However, there are some problems associated with measuring insulators, such as a buildup of surface charge. An electron flood gun can be used for charge neutralization, but it may not solve the problem completely, since the charge buildup may not necessarily be uniform. In principle, it is also possible to measure liquids using a liquid beam/jet, as originally proposed by Siegbahn[66], and presented in the literature such as Ref.[68]. However, then the system is not in an equilibrium state, which significantly complicates the analysis and goes beyond the scope of this dissertation. Only semiconductors are studied in this dissertation.

Figure 2.2 illustrates the XPS process schematically.
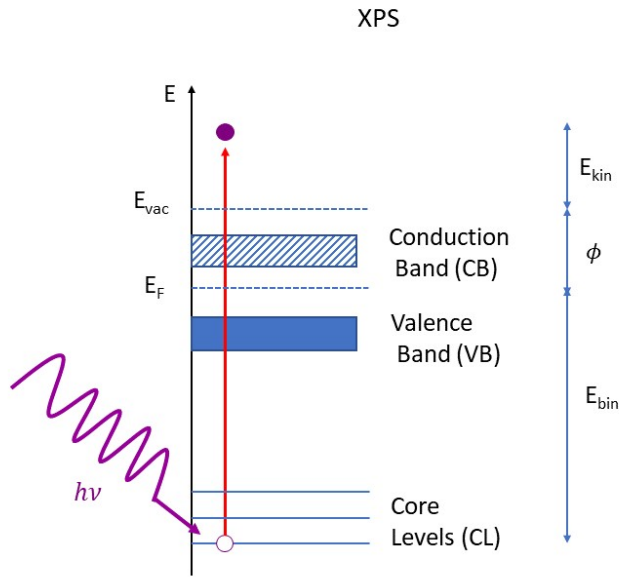
Figure 2.2. A schematic representation of the XPS process.

All of the electron states in semiconductors can be characterized into three types: core levels (CL), valence band (VB), and conduction band (CB). At absolute zero (T = 0 K), the VB is completely filled, while the CB is free of electrons. Electrons in CLs are in the inner orbitals and do not participate in chemical bonding; they can therefore be thought of as behaving like atomic orbitals, with no band dispersion. The only difference with atomic orbitals is the chemical shift: the binding energy of the CL electrons can shift slightly (on the order of 1 to several eV) depending on the chemical bonds the atom from which the electron is ejected is forming. For example, in metal oxides, the oxygen atom is more electronegative and pulls the electrons towards it, resulting in a higher binding energy of the corresponding CL of the metal compared to if it were in a pure metal state.

In XPS, both the CLs and the VB states are probed. The CLs allow to obtain information on the chemical structure, and the VB states mainly on the electronic structure of the material.

The key components in an XPS experimental setup are the x-ray source, the analysis chamber under ultra-high vacuum (UHV), and the hemispherical analyzer and detector. In the x-ray source, a tungsten filament acts as the cathode, which is heated by an electric current, generating electrons. A high potential difference (15 kV) is applied between the cathode and anode made

from the target material. The thermoelectrons are accelerated towards the anode, and as a result of the interaction between the electrons and anode material, x-rays are emitted. The x-ray tube that Röntgen used when he discovered x-rays in 1895 was essentially not so different; the modern configuration is under vacuum, while in the early setup there was a partial vacuum and the electrons were produced by ionization of the residual air molecules.

The resulting x-ray spectra consists of two components. First, there is the continuous spectrum due to bremsstrahlung ("braking radiation"): the electrons emitted from the cathode are decelerated in the target material and emit radiation as a result. On top of the bremsstrahlung lie the characteristic x-ray peaks. When an electron emitted from the cathode strikes the target material, an electron from an inner shell is ejected, forming a core hole; an electron from an outer shell relaxes and fills this hole, and an x-ray photon is emitted as a result. The transitions must obey the selection rule for angular momentum: $\Delta L = \pm 1$. Thus, s-s transitions are forbidden. Siegbahn notation is used for the characteristic X-rays: transitions from the $L_{2,3}$ (2p) to the K (1s) level are the K_α emission lines, $M_{2,3}$ (3p) to K (1s) are the K_β lines, and so on.

The two x-ray sources used for measurements presented in this dissertation are Mg K_α, with energy 1253.6 eV and line width 0.7 eV, and Al K_α , with energy 1486.7 eV and line width 0.85 eV. In our laboratory, for Al K_α radiation, a monochromator (a quartz crystal) is used to remove the K_β line, bremsstrahlung, and make the narrower line width. This reduces the intensity of the photoelectron beam, but the resolution is greatly improved.

It is important to note that the chamber where the measurements are performed must be under ultra-high vacuum (UHV), which is defined as the vacuum characterized by pressures less than 10^{-8} mbar; in practice measurements are performed with pressure on the order of 10^{-10} mbar. UHV is crucial for XPS measurements, to ensure a sufficiently low probability of the photoelectrons interacting with residual gas molecules. In addition, XPS is a surface-sensitive technique (see more below) so it is important to ensure an atomically-clean sample surface. The time t (in seconds) it takes to form a new monolayer of surface adsorbates (such as oxygen, carbon, and their compounds) on a freshly cleaned surface is (roughly) given by[69]

$$t[s] = \frac{1.7 \times 10^{-6}}{0.6 \cdot p \cdot S[mbar]}, \tag{2.2}$$

where the pressure p is in mbar, and S is the Sticking coefficient, (which is 1 if all the atoms colliding with the surface stick to it). Thus, for pressures on the order of 10^{-8} mbar, a new monolayer will form after several minutes, while for pressures on the order of 10^{-10} mbar, it will already take several hours.

The photoelectrons are decelerated by electrostatic lenses and go through a hemispherical analyzer with two concentric hemispheres with a potential difference applied between them. This potential difference sets the so-called pass energy, the kinetic energy the photoelectrons must possess to travel across the analyzer. The voltages are usually kept constant to ensure a constant energy resolution. For further details of the experimental setup, please refer to Chapter 3, as well as literature such as Refs.[69,70].

The photoemission process can be described theoretically as follows. In time-dependent first order perturbation theory, the transition probability per unit time, W_{fi}, from the initial state (ground state) to the final state (1 electron ejected from the material and the $(N-1)$ electron system is given by Fermi's golden rule:[71]

$$W_{fi} \propto \frac{2\pi}{\hbar}\left|\langle\psi_f|\widehat{H}'|\psi_i\rangle\right|^2 \delta(E_i - E_f - h\nu) = \frac{2\pi}{\hbar}\left|M_{fi}\right|^2 \delta(E_i - E_f - h\nu). \quad (2.3)$$

Here, ψ_i and ψ_f are the initial and final eigenstates, and E_i and E_f are the initial and final eigenvalues of the unperturbed Hamiltonian $\widehat{H}_0$. $\widehat{H}'$ is the interaction Hamiltonian describing the perturbation, M_{fi} are the transition matrix elements, and the delta function ensures energy conservation. The interaction Hamiltonian is given by:

$$\widehat{H}' = -\frac{e}{mc}\vec{A}\cdot\vec{p}, \quad (2.4)$$

where $\vec{A}$ is the vector potential of the electromagnetic field, $\vec{p}$ is the momentum of the electron, m and e are the mass and charge of the electron, and c is the speed of light. Several approximations are made when writing down Equation 2.4: the scalar potential is set to zero, the linear optical regime is assumed, which allows to drop the quadratic term in $\vec{A}$, and the dipole approximation is made (neglecting spatial variations of $\vec{A}$ over atomic distances), i.e., $\nabla\vec{A} = 0$. In addition, the commutation relation $[\vec{p}, \vec{A}] = i\hbar\nabla\vec{A}$ is used to obtain Equation 2.4.[69]

Assuming the investigated surface is homogenous and infinitely thick, the photoelectrons are detected perpendicularly to the sample, and the angle between the x-ray source and the analyzer is the magic angle (54.7°), the intensity of an XPS spectrum can be expressed/approximated by the following formula:

$$I \sim \sigma N \lambda(E) T(E). \tag{2.5}$$

The magic angle ensures that the angular asymmetry factors can be set to unity.[72]

In equation 2.5, σ is the photoionization cross-section, which describes the probability for the photoemission to occur, and is proportional to the square of the matrix elements:

$$\sigma \propto \sum_f |M_{fi}|^2. \tag{2.6}$$

N is the concentration of the element in the investigated sample. λ is the inelastic mean free path (IMPF); it describes the distance an electron can travel through a material before the intensity of the electron beam decreases to $1/e$ of its initial value. It is a function of the kinetic energy, and is roughly described by the universal curve shown in Figure 2.3[73] below:
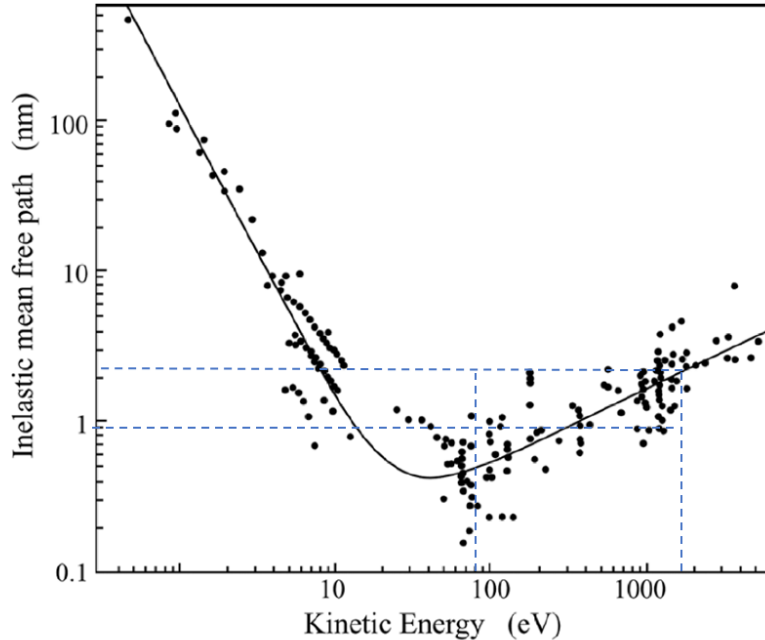
Figure 2.3. Inelastic mean free path as a function of the kinetic energy. The experimental data points for different materials are averaged to obtain the universal curve. The kinetic energy range roughly explored

by XPS, and the corresponding IMFP values are indicated by the blue dashed lines. Figure reproduced from Ref.[73].

From Figure 2.3, one can see that for Mg K_α and Al K_α- excited XPS, the photoelectron kinetic energies roughly vary from 100 to 1500 eV, and the IMFP roughly ranges from 1 to 3 nm. Thus, XPS measurements are surface sensitive. As will be explained in more detail in 2.1.1.3, hard x-ray photoelectron spectroscopy (HAXPES), allows to obtain more bulk-sensitive results.

T is the analyzer transmission function, and it depends on the kinetic energy. It depends on the pass energy of the analyzer as well, so it is important to choose appropriate values for the pass energy to maximize the intensity, as well as to obtain high resolution spectra.

In this dissertation, the ratio of concentrations of two elements are determined from XPS peaks with very similar kinetic energies. In this case, λ and T can be considered to be nearly identical. Then the ratio of the concentration of two elements A and B in the sample can be written as:

$$\frac{N_A}{N_B} = \frac{I_A/\sigma_A}{I_B/\sigma_B} \tag{2.7}$$

Specifically, the Ga/In ratio (and thus the [Ga]/ ([Ga]+[In]) or GGI ratio which is important for the solar-cell samples presented in Chapter 4) can be computed in this way from the In 4d (binding energy ~17-18 eV) and Ga 3d (binding energy ~ 18-20 eV) peaks.

In addition to the electrons forming the main photoelectron peaks, there are electrons that are inelastically scattered before they are able to escape into the vacuum; these electrons constitute the background observed in the XPS spectrum. Different functions can be used to describe the background such as the Shirley or Tougaard background; however, in this dissertation a simple linear function was found to be sufficient to describe the background.

The core hole formed has a finite lifetime τ on the order of 10^{-15} s; by Heisenberg's uncertainty principle this corresponds to a lifetime broadening $\Gamma = \frac{\hbar}{\tau}$, which is on the order of 0.1 eV. This intrinsic lifetime broadening contributes to the broadening of the XPS peaks and is described by a Lorentzian function. In addition, there are various factors contributing to the experimental broadening, the main factors being the resolution of the electron analyzer, and the line widths of the x-ray source. In addition, there are factors such as thermal, pressure, and vibrational broadening, which can also contribute to the experimental broadening. In general, the

experimental broadening can typically be approximated by a Gaussian function. To take into account the various effects, together with a linear fit of the background, the XPS peak is fitted by a Voigt function, which is a convolution of the Gaussian and Lorentzian functions. The fits are performed in the Fityk software,[74] where the ratio between the Gaussian and Lorentzian functions can be varied to obtain an optimal fit.

The core hole will be filled by an electron lying at a higher energy level. The resulting energy can be used in one of two processes: an x-ray photon can be emitted, or another electron can be emitted into the vacuum. The latter process will be described in the following section.

2.1.1.2 X-ray excited Auger electron spectroscopy

Figure 2.4 shows the X-ray-excited Auger electron spectroscopy (XAES) process:
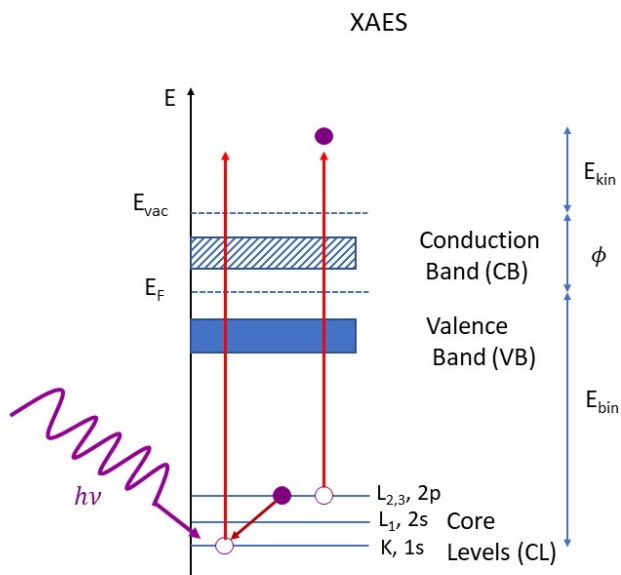
Figure 2.4. Schematic representation of the XAES process, after the core hole is created in XPS. The spin-orbit splitting of the 2p level is not shown for simplicity.

For the Auger process to occur, a core hole must be created, either by an electron or x-ray photon. When the x-ray source creates the core hole (i.e., the XPS process), the consequent Auger process is known as x-ray excited Auger spectroscopy (XAES). Then, the core hole is filled by a higher lying electron (either from a core level or the valence band), and the energy left

is used for the emission of a second (Auger) electron (also from a core level or the valence band). In Figure 2.4, the kinetic energy of the Auger electron, E_{Auger} is given by

$$E_{Auger} = E_K - E_{L1} - E_{L2,3} - \phi, \tag{2.8}$$

where E_K, E_{L1}, and $E_{L2,3}$ are the binding energies of the 1s, 2s, and 2p electrons, respectively, and ϕ is the work function. Other transitions (e.g., with a core-hole in the L or M level, or the higher-lying electrons in the valence band) are also Auger transitions occurring in various materials. From Equation 2.8, it is clear that the Auger kinetic energy is independent of the initial photon energy. Therefore, the XAES spectral intensities are plotted as a function of the kinetic energy rather than the binding energy as in XPS. It should be mentioned that x-ray notation is used to specify the Auger process (as compared to spectroscopic notation used in XPS).

As mentioned in 2.1.1.1, x-ray emission (XES) is a competing process to the Auger process. However, as shown in Figure 2.5 below, for light elements (Z< 30), Auger emission is more likely to occur:
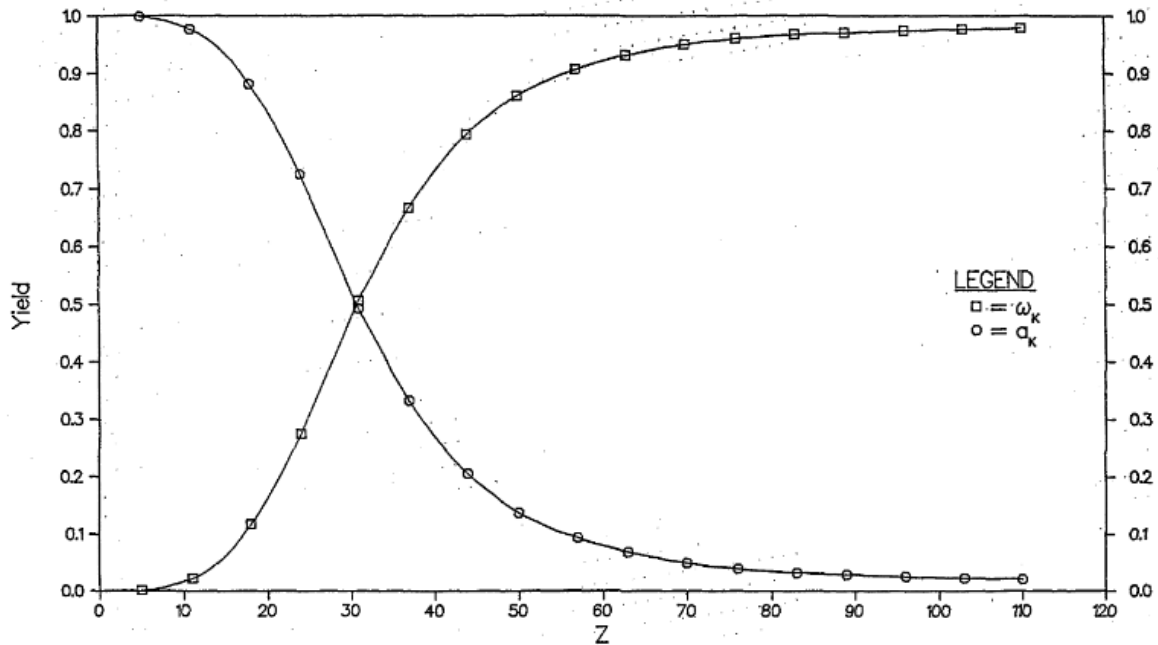
Figure 2.5. Auger and fluorescence x-ray yields as a function of the atomic number when a core hole is created in the K shell (i.e., the 1s orbital). The fluorescence yields are denoted as ω_K with square data points, while the Auger yields are denoted as a_K with circle data points. Figure reproduced from Ref.[75].

14

The Auger kinetic energy is element specific, and Auger spectra have very distinct shapes depending on the specific transitions. As such they offer complimentary information to XPS on the chemical structure of the investigated material. Due to the complex shapes of Auger spectra, the fitting procedure differs to that of XPS spectra. Rather than using an analytical function, the Auger spectra of a reference material/sample are taken, and a multi-component fit is performed.

The chemical shifts of the Auger spectra are often larger than of the corresponding photoelectron peaks. Combining this information can be very useful when analyzing the chemical structure, which is done by calculating the modified Auger parameter for an element, α', which is defined as follows:

$$\alpha' = E_{bin}(photoemission) + E_{kin}(Auger). \tag{2.9}$$

In other words, the binding energy of the most prominent photoemission peak, and the kinetic energy of the most prominent Auger peak are added together. It is robust to charging effects since charging has the opposite effect on kinetic and binding energies. This makes it easier to identify the chemical compounds in a material. Values of the modified Auger parameter are presented in literature such as the NIST XPS Database,[76] and are often shown in the form of a Wagner plot: the photoelectron binding energies are plotted on the x-axis, and the corresponding Auger kinetic energies are plotted on the y-axis; diagonal lines indicate the calculated modified Auger parameter.[77]

2.1.1.3 Synchrotron based (hard) x-ray photoelectron spectroscopy

In 2.1.1.1, it was mentioned how bremsstrahlung contributes to the background of the x-ray radiation, upon which are situated the characteristic x-ray lines. The bremsstrahlung is mostly seen as an impediment and can be removed by monochromatizing the x-ray light. The generation of synchrotron radiation can be understood by drawing a parallel to how bremsstrahlung is created.

The synchrotron was invented by Vladimir Veksler in 1944,[78] and is a type of cyclic particle accelerator where an electric field is used to accelerate the particles, and a magnetic field is used

to bend their trajectory (bending magnets). The particles travel with a constant speed, and in a (nearly) circular trajectory; thus, they have a centripetal acceleration. According to the classical theory of electromagnetism, they emit radiation as a result of this acceleration. This radiation can be used as the light source for various experiments. The storage ring is a special type of synchrotron where the electrons are "stored" by circulating with a (mostly) constant energy. At the KIT light source, the electrons circulate around the storage ring at 2.5 GeV.[79] The radiation is produced at bending magnets and specialized insertion devices called wigglers and undulators that are inserted into the straight sections of the storage ring, creating highly brilliant synchrotron radiation. Beamlines are built tangentially to the bending magnets or insertion devices and capture the radiation exiting at a tangent from the storage ring. Figure 2.6 shows the layout of the KIT light source:
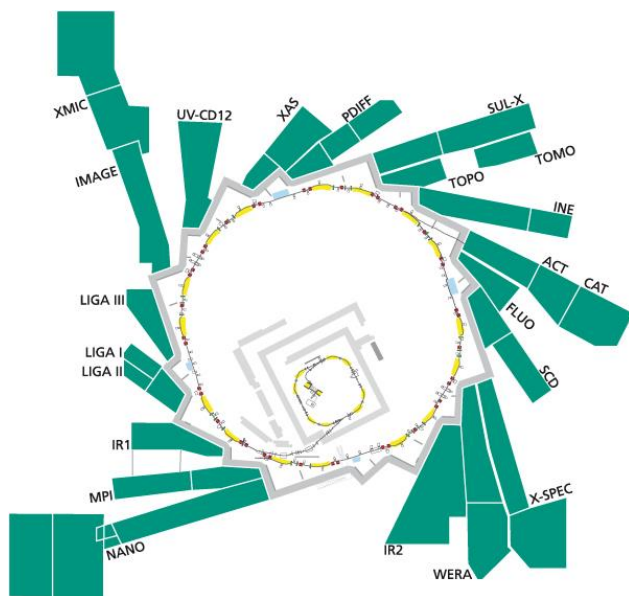
Figure 2.6. Schematic layout of the KIT light source: microtron, storage ring, and beamlines (X-SPEC beamline on the lower right side). Figure reproduced from Ref.[80].

In this dissertation, photoelectron spectroscopy (PES) studies were done at the (double) undulator X-SPEC beamline at the KIT synchrotron.[62] Experimental details and the beamline layout are presented in Chapter 3. The x-ray beam has a high photon flux and is much more

intense and collimated than the laboratory-based sources. In addition, one of the main advantages is the available variation of photon energy as compared to the discrete photon energy in laboratory-based XPS. In particular, X-SPEC offers a wide photon energy range of 70 eV up to 15 keV. Experiments presented in this dissertation were performed in the photon energy range from 70 eV to 6.3 keV, corresponding to a maximum IMFP (when the kinetic energy is maximal and the binding energy is close to zero) from 0.5 to 7.9 nm (see Table 5.1 in Chapter 5). Experiments performed with photon energies of 2.1 keV and higher are referred to as hard x-ray PES (HAXPES). By performing (HAX)PES measurements on a sample at these wide range of photon energies, information on the chemical and electronic structure of both its bulk and surface can be obtained. In Chapter 5, valence band measurements at this wide range of photon energies are presented.

2.1.2 X-ray Spectroscopies

2.1.2.1 X-ray absorption and emission spectroscopies

In all of the techniques discussed in 2.1.1, the emitted electrons were detected, i.e., "photon in, electron out" techniques were presented. In this section, "photon in, photon out" techniques are discussed. Figure 2.7 illustrates the x-ray absorption (XAS) and x-ray emission (XES) processes:
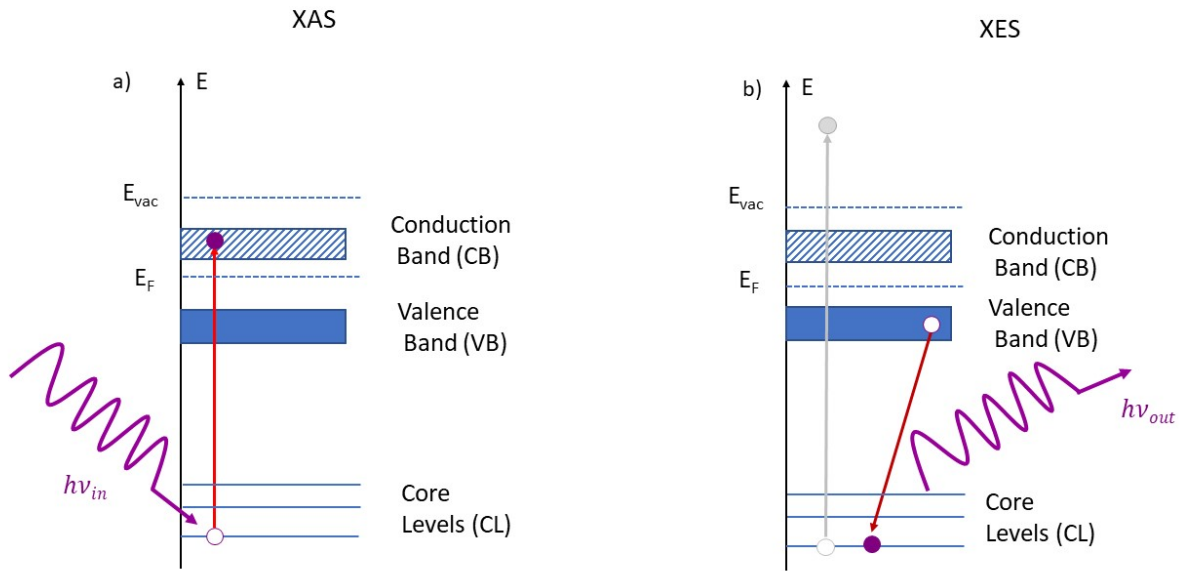
Figure 2.7. Schematic representation of the XAS and XES, and RIXS processes. a) describes XAS, b) describes XES (the initial excitation is shown in gray and is non-resonant, with the photoelectron leaving the system), and a) followed by b) describes RIXS (without the excitation shown in gray).

In XAS (Figure 2.7 a)), an incident x-ray photon with energy $h\nu_{in}$ is used to excite a core electron into the conduction band (not into the vacuum as in XPS). The absorption is measured and plotted as a function of $h\nu_{in}$. In XES, the excitation is typically non-resonant, i.e., $h\nu_{in}$ is significantly larger than the energy required to excite the core electron into the conduction band. This initial excitation is shown in gray in Figure 2.7 b). The created core hole is then filled by an electron lying at a higher level (the valence band or higher-lying core levels). The energy created by this relaxation process is used in the emission of another photon, which is detected in XES experiments. The intensity of the emitted x-rays is plotted as a function of $h\nu_{out}$.

As for photoelectron spectroscopy, the transitions from the initial to final states are described by Fermi's golden rule (Equation 2.4). In the dipole approximation, the interaction Hamiltonian can be written as: $\widehat{H}' = \vec{e} \cdot \vec{r}$, where $\vec{e}$ is the polarization vector of the light source and $\vec{r}$ is the position vector. This approximation works well for light atoms such as O with small core wave-functions, i.e., small r, and small photon energies, i.e., small $h\nu$.[81] Keeping in mind the definition of the density of states, $\rho(E) = \sum_f \frac{2\pi}{\hbar} \delta(E - E_f)$, XAS and XES intensities can be written as:

$$I_{XAS}(h\nu_{in}) \propto \left|\langle\psi_f|\vec{e}\cdot\vec{r}|\psi_i\rangle\right|^2 \rho_f(E_f), E_f = E_i + h\nu_{in} \qquad (2.10)$$

$$I_{XES}(h\nu_{out}) \propto \left|\langle\psi_f|\vec{e}\cdot\vec{r}|\psi_i\rangle\right|^2 \rho_i(E_i), E_i = E_f + h\nu_{out} \qquad (2.11)$$

For the XAS and XES intensities to be non-zero, the states must have an overlap with the localized core hole. In addition, the dipole selection rules must be followed, in particular, the angular momentum quantum number L must follow: $\Delta L = \pm 1$. This is why in XAS and XES the intensity is proportional to the *local partial* DOS (LPDOS). In Chapter 6, the O 1s core-level is probed by XAS and XES. This means that transitions from a state with overlap with the O 1s with p symmetry are allowed. Due to the transition matrix elements, the XAS and XES spectra depend on the orientation of the crystal with respect to the polarization of the incident x-ray beam, which will be explored in Chapter 6.

Similar to the IMFP for electrons, the x-ray attenuation length describes the distance that the x-ray travels in a material before its intensity decreases to $1/e$ of its initial value. The attenuation lengths are tabulated in the Center for X-Ray Optics x-ray database,[82] and are on the order of 0.1 μm or 100 nm for O K XAS and XES of Ga_2O_3 (photon energies $\sim$ 530 eV). So, these X-ray spectroscopic methods probe the bulk of the material, in contrast to the surface-sensitive XPS and XAES.

To combat the low fluorescence yield (for elements with $Z < 30$; see Figure 2.5), and to be able to tune the x-ray energies, a high-flux source as provided by synchrotron radiation and a spectrometer with a high-efficiency are indispensable for XAS and XES experiments. In XAS, information about the unoccupied states, i.e., the CB in semiconductors, or the lowest

unoccupied molecular orbital (LUMO) for molecules is obtained, while in XES, the occupied states, i.e., the VB in semiconductors, or the highest unoccupied molecular orbital (HOMO) for molecules is obtained. XAS and XES are bulk-sensitive techniques, which means that how the sample surface is prepared is less critical than for the surface-sensitive photoelectron spectroscopy methods. Thus, XAS and XES measurements may be advantageous compared to XPS or HAXPES for samples with poorly defined surfaces and molecular systems.

2.1.2.2 Resonant inelastic x-ray scattering

Historically, because of experimental limitations, XAS and XES spectra were obtained separately, and were thus considered as two independent, although related processes.[83] However, with the advances in synchrotron radiation sources in the 1990s, it was shown that when the incident photon energy $h\nu_{in}$ is chosen such that it is close to the x-ray absorption edge of the material, the emission spectra strongly depend on $h\nu_{in}$. The results of the C K edge resonant emission spectra of diamond were formative in further developments.[84] In a subsequent paper by one of the same authors,[83] it was shown that the absorption and emission is in fact a one-step process, where the photon is scattered, losing the energy $(h\nu_{in} - h\nu_{out})$ as a result. In solid state systems, an electron hole pair is formed. This combined process is called resonant inelastic x-ray scattering (RIXS). Whereas the transition probability for one-photon processes (XPS, XES, XAS) is given by Equation 2.4, for two photon processes (RIXS and other scattering processes), the intensity is proportional to the scattering cross-section given by the Kramers-Heisenberg formula:[85–87]

$$I_{RIXS}(h\nu_{in}, h\nu_{out}) \propto \frac{\nu_{out}}{\nu_{in}} \sum_f \sum_m \frac{|\langle f|\boldsymbol{p} \cdot \boldsymbol{E_{out}}|m\rangle\langle m|\boldsymbol{p} \cdot \boldsymbol{E_{in}}|i\rangle|^2}{(E_m - E_i - h\nu_{in})^2 + \frac{\Gamma_m^2}{4}} \delta(h\nu_{in} - h\nu_{out} - E_f + E_i) \quad (2.12)$$

Here, $|i\rangle$ is the initial ground state, $|f\rangle$ is the final state with an electron in the CB and a hole in the VB, and $|m\rangle$ is the intermediate state with the core hole with lifetime broadening Γ_m, and the summation is performed over all intermediate and final states. E_i, E_m, and E_f are the energies of the initial, intermediate, and final states, and the Dirac-delta function ensures energy conservation. When $h\nu_{in}$ is on-resonance, the scattering cross-section can be enhanced by many

orders of magnitude. If there was no Γ_m, the condition for resonance would be:

$E_m - E_i - h\nu_{in} \rightarrow 0$. Then, $E_m \rightarrow E_i + h\nu_{in}$, i.e., resonance would only occur when the incident photon energy is approaching the absorption edge. With Γ_m, the condition for resonance becomes: $(E_m - E_i - h\nu_{in})^2 \lessgtr \frac{\Gamma_m^2}{4}$. So, detuned excitation is possible, within the limits of Γ_m (following a Lorentzian distribution)[88]. Thus, the lifetime broadening of the intermediate states allows to use photon energies below the absorption edge to excite electrons into "virtual" states, with an associated Raman shift (see Chapter 6). Since there is no core hole in the final state, the lifetime broadening of the core hole is eliminated. The above Figure 2.7 a) followed by b) illustrates the one-step process of RIXS.

The RIXS spectral intensity is a function of both $h\nu_{in}$ and $h\nu_{out}$, so a two-dimensional representation of the data is desirable. However, usually only a few RIXS spectra can be measured, and it would take a very long time to obtain densely spaced RIXS spectra. The high-transmission, high-resolution spectrometer developed by our group (see Chapter 3) allows measurements of "maps", two-dimensional plots of a series of emission spectra for each excitation energy of a "normal" XAS scan, to be performed in less than an hour.[89]

2.2 Computational Methods

(This section is based on the introduction given in Ref.[90]. Readers are also referred to other introductory material such as [91]).

Computational solid-state physics/chemistry deals with calculating various properties of molecules and solids. In this dissertation, the focus is on calculating the electronic structure of solids, from which spectra (PES, XAS, XES, and RIXS spectra) are obtained. A solid is a system of $N + ZN$ interacting particles, where N is the number of nuclei, and Z is the number of electrons in an atom. This is a many-body problem for which the exact many-body Hamiltonian is:

$$
\begin{aligned}
\hat{H} = &-\frac{\hbar^2}{2}\sum_i \frac{\nabla^2_{\vec{R}_i}}{M_i} - \frac{\hbar^2}{2}\sum_i \frac{\nabla^2_{r_i}}{m_e} \\
&-\frac{1}{4\pi\epsilon_0}\sum_{i,j}\frac{e^2 Z_i}{\left|\vec{R}_i - \vec{r}_i\right|} + \frac{1}{8\pi\epsilon_0}\sum_{i,j}\frac{e^2}{\left|\vec{r}_i - \vec{r}_j\right|} \\
&+\frac{1}{8\pi\epsilon_0}\sum_{i\neq j}\frac{e^2 Z_i Z_j}{\left|\vec{R}_i - \vec{R}_j\right|}
\end{aligned}
\tag{2.13}
$$

The nuclei are located at R_i with mass M_i and the electrons are at r_i with mass m_i. The terms in the Hamiltonian are (from first to last): the kinetic energy operator of the nuclei, the kinetic energy operator of the electrons, and the Coulomb interaction between the electrons and nuclei, the electron-electron interaction, and the nuclei-nuclei interaction. Solving the Schrödinger Equation for this many-body problem exactly is not possible, and some approximations must be made.

The first approximation made is the Born-Oppenheimer approximation. Since the nuclei are much heavier and hence slower than the electrons, they can be assumed to be fixed, and the electrons are moving in the external potential of the nuclei. This removes the first term of the Hamiltonian in Equation 2.13 and reduces the last term to a constant, resulting in:

$$\hat{H} = \hat{T} + \hat{V} + \hat{V}_{ext} \tag{2.14}$$

where $\hat{T}$ is the kinetic energy operator of the electrons, $\hat{V}$ is the potential energy of the electron-electron interaction, and $\hat{V}_{ext}$ is the potential energy of the electron-nuclei interaction. This Hamiltonian is still too large and complex to be able to solve. Several methods have been developed to further simplify the problem, such as the Hartree-Fock method[92], and Density Functional Theory, the latter of which will be introduced below.

2.2.1 Density Functional Theory

As the name implies, in Density Functional Theory (DFT), the ground-state properties of a many-body system are obtained through the functional (function of another function) of the density. The theory of DFT was first established by the two theorems of Hohenberg and Kohn[93], and the Kohn-Sham equations[94] allowed the practical implementation of DFT. The Kohn-Sham equations enable the many-body problem of N interacting electrons in a static external potential (the nuclei) to be reduced to a problem of N *non*-interacting electrons in potentials due to the nuclei, as well as due to exchange and correlation effects. The Kohn-Sham Hamiltonian $\hat{H}_{KS}$ is:

$$\hat{H}_{KS} = \hat{T}_0 + \hat{V}_H + \hat{V}_{xc} + \hat{V}_{ext} \tag{2.15}$$

where $\hat{T}_0$ is the functional for the kinetic energy of a non-interacting electron gas, $\hat{V}_H$ is the Hartree potential, $\hat{V}_{xc}$ is the exchange-correlation functional, and $\hat{V}_{ext}$ is the external potential. The theorem of Kohn and Sham states that the exact ground-state density of an N-electron system is given by:

$$\rho(\vec{r}) = \sum_{i=1}^{N} \phi_i(\vec{r})^* \phi_i(\vec{r}) \tag{2.16}$$

where $\phi_i(\vec{r})$ are N single-particle wave functions that are solutions to the Schrödinger-like Kohn-Sham equations:

$$\widehat{H}_{KS}\phi_i = \epsilon_i\phi_i \qquad (2.17)$$

The eigenvalues and eigenvectors can be obtained using traditional linear algebra techniques. It is important to note that the ϕ_i and ϵ_i are wavefunctions and energies of a fictitious system, i.e., they are not the electronic wavefunctions and energies. The Kohn-Sham equations are solved iteratively: an initial density ρ_0 is guessed, from which a Hamiltonian $\widehat{H}_{KS1}$ is built. Then, the equations are solved, obtaining a set of ϕ_1, from which ρ_1 is obtained. If ρ_1 and ρ_0 are equal, then the true ground-state density has been obtained. Usually this is not the case, and then the cycle is repeated until $\rho_n = \rho_{n-1}$ with a given precision (which is set by a convergence parameter). This is known as the self-consistent field cycle (SCF).

If the exchange-correlation functional $\widehat{V}_{xc}$ was known, then DFT would allow to obtain the exact ground-state density. However, the exchange-correlation functional is in fact not known and must be approximated. One such approximation is the local density approximation (LDA), where the material is divided into a 3-dimensional grid of infinitesimally small volumes with a constant density. Then, it is assumed that the contribution from each such volume to the exchange-correlation energy is the same as that of a homogenous electron gas, with the same overall density as the material has in this volume.[90] The LDA functional is very efficient as it only depends on the local density.[95] Further elaborated approximations are where both the local density and its gradient play a role, and such approximations are known as generalized gradient approximations (GGA). The Perdew-Burke-Ernzerhof (PBE) functional [96] belongs to the class of GGA functionals, and is the one used in the calculations presented in this dissertation.

To solve the Kohn-Sham equations, the wavefunctions need to be expressed in a chosen finite basis set. Examples of two different types of basis sets are plane waves, and augmented plane waves plus local orbitals, which are used in Quantum Espresso (to obtain the ground-state wavefunctions in OCEAN) and Wien2k, respectively. One of the main differences in the two

methods employed in Quantum Espresso and Wien2k is how the core and valence electrons are treated. The two methods will be introduced in the following two sections.

2.2.1.1 Plane wave pseudopotential method

Assuming that there are periodic boundary conditions applied to the investigated material, following Bloch's theorem, its eigenfunctions $\psi_{\vec{k}}^n$ can be written in the plane wave basis set as follows:

$$\psi_{\vec{k}}^n(\vec{r}) = \sum_{\vec{K}} c_{\vec{k}}^{n,\vec{k}}\, e^{i(\vec{k}+\vec{K})\cdot\vec{r}} \tag{2.18}$$

where $\vec{k}$ is the vector in the first Brillouin zone, $\vec{K}$ is the reciprocal lattice vector (often labeled as $\vec{G}$), n is the band index, and $\vec{r}$ is the position vector. There are an infinite set of coefficients $c_{\vec{k}}^{n,\vec{k}}$ for the basis functions of the form $e^{i(\vec{k}+\vec{K})\cdot\vec{r}}$. For practical purposes a finite number of basis functions are required, so only plane waves with $\vec{K} \leq \vec{K}_{max}$ are used in the basis set. This corresponds to a plane-wave cutoff energy of:

$$E_{cut} = \frac{\hbar^2 K_{max}^2}{2m_e} \tag{2.19}$$

This cut-off energy must be specified when setting up the calculations.

The valence electrons are far away from the nuclei and can be approximated as free electrons. Plane waves are solutions of the Schrödinger equation when there is no potential in the Hamiltonian. On the other hand, the core electrons are much better described by atomic-like wavefunctions (see next section). In fact, the radial part of the wavefunction oscillates the most in the regions closest to the nuclei, so trying to describe this region by plane waves would require such a large number of basis functions that computations would be complicated To solve this

problem, since the core electrons do not directly participate in chemical bonding, they are "frozen out", and the potential in the regions close to the nuclei is replaced by a pseudopotential, which acts on corresponding pseudo wavefunctions. Then the core electrons are not part of the subsequent DFT calculation. Thus, the required basis set is small, and the number of electrons is reduced, so the computations can be carried out. It is important to use pseudopotentials that are *soft* (require few plane waves) and *transferrable* (system-independent). In OCEAN, the OPIUM code[97] is used to generate the pseudopotentials.

Since the ultimate goal is to calculate spectra where (usually) electrons are excited from core levels, the core levels must be accounted for. So, in OCEAN, after the pseudopotential-based DFT calculation is performed, a separate calculation of the core level wavefunctions is performed for an isolated atom.[98,99] A transformation from the pseudo to these all-electron wavefunctions is required; the projector augmented wave (PAW) method[100] is used in OCEAN for this transformation.

2.2.1.2 Augmented plane wave-based all-electron method

Other type of methods are the augmented plane wave (APW) - based methods. As shown in Figure 2.8, in APW-based methods, the unit cell is divided into two regions: spheres (sphere x has radius R_x), and the interstitial region between the spheres, I:
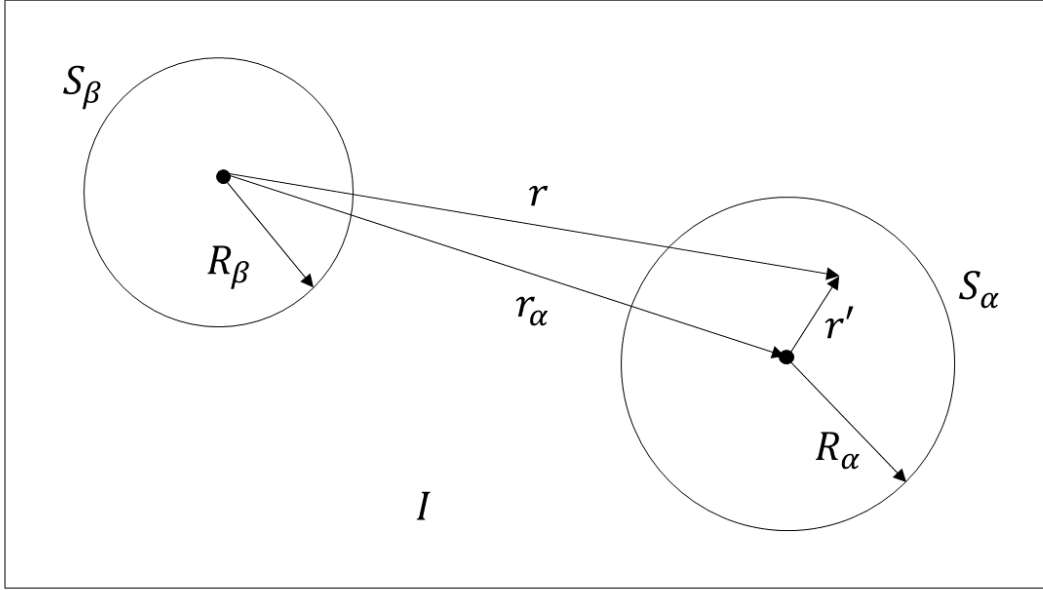
Figure 2.8. Division of the unit cell into the muffin tin regions, and the interstitial regions[90].

Electrons inside the spheres have atomic-like wavefunctions, while electrons in the interstitial region behave like plane waves. The potential is assumed to be spherically symmetric inside the spheres, and constant in the interstitial region, so it is called the muffin-tin potential, and the spheres are referred to as muffin-tin spheres. The APW basis function is defined as:

$$\phi_{\vec{K}}^{\vec{k}}(\vec{r}, E) = \begin{cases} \dfrac{1}{\sqrt{V}} e^{i(\vec{k}+\vec{K})\cdot\vec{r}}, \vec{r} \in I \\ \displaystyle\sum_{l,m} A_{lm}^{\alpha,\vec{k}+\vec{K}} u_l^{\alpha}(r', E) Y_m^l(r'), r' \in S_{\alpha} \end{cases} \tag{2.20}$$

where $\vec{k}, \vec{K}$, and $\vec{r}$ are defined as before for the plane waves, and V is the volume of the unit cell. The radial part of the atomic orbitals is u_l^{α}, and Y_m^l are the spherical harmonics (l and m are the angular and magnetic quantum numbers, respectively). The distance inside the sphere relative to its center is $\vec{r}'$ as shown in Figure 2.8.

To have a well-defined kinetic energy, the plane wave outside the sphere must match the function inside the sphere, which determines the coefficients $A_{lm}^{\alpha,\vec{k}+\vec{K}}$. However, the eigenenergy E is still undefined. In the APW method, it must be guessed first, and an iterative procedure is carried out where the APWs are determined for this trial E, from which the Hamiltonian is constructed, the matrix equation is solved, and new E are determined, until they are the same as the trial E. This results in a long computation time. To combat this problem, in the *linearized* augmented plane wave method (LAPW), a Taylor expansion of $u_l^\alpha(r', E)$ at some known energy E_0 is performed, and is approximated by the first two terms. Then, the resulting LAPW basis functions are:

$$\phi_{\vec{K}}^{\vec{k}}(\vec{r}) = \begin{cases} \dfrac{1}{\sqrt{V}} e^{i(\vec{k}+\vec{K})\cdot\vec{r}}, \vec{r} \in I \\ \displaystyle\sum_{l,m} (A_{lm}^{\alpha,\vec{k}+\vec{K}} u_l^\alpha(r', E_0) + B_{lm}^{\alpha,\vec{k}+\vec{K}} \dot{u}_l^\alpha(r', E_0)) Y_m^l(r'), r' \in S_\alpha, \end{cases} \qquad (2.21)$$

where $\dot{u}_l^\alpha$ is the derivative of u_l^α. To determine the coefficients $A_{lm}^{\alpha,lo}$ and $B_{lm}^{\alpha,lo}$, the plane waves and the functions inside the sphere, as well their derivatives, must match each other at the boundary. In the final step, rather than taking one universal E_0, a set of eigenvalues E_{tl} are taken.

In the APW+ lo method, another type of basis functions called local orbitals (lo) are added (for each atom), which are zero in the interstitial region, and in the muffin tin region of other atoms:

$$\phi_{\alpha,lo}^{lm}(\vec{r}) = \begin{cases} 0, \vec{r} \in I \\ \displaystyle\sum_{l,m} (A_{lm}^{\alpha,lo} u_l^\alpha(r', E) + B_{lm}^{\alpha,lo} \dot{u}_{lm}^{\alpha,lo}(r', E)) Y_m^l(r'), r' \in S_\alpha \end{cases} \qquad (2.22)$$

where $\dot{u}_{lm}^{\alpha,lo}$ is the derivative of u_l^α. The two coefficients $A_{lm}^{\alpha,lo}$ and $B_{lm}^{\alpha,lo}$ are determined by requiring that the local orbital has zero value at the boundary of the muffin tin, and also that it is normalized.

In the APW-based methods, the cutoff parameter for the number of basis functions used is the product of the smallest muffin tin radius (R_α^{min}) and the largest K vector (K_{max}, same as for the plane-wave basis), $R_\alpha^{min} K_{max} = l_{max}$. Typically, this cutoff parameter is set to a value between 6 and 9 [101]. The (L)APW-based methods are all-electron methods, so core and valence electrons are treated together in the same way.

2.2.2 The Bethe-Salpeter Equation approach

DFT calculations provide accurate results for the ground-state electron density, and allow to obtain good results for the band structure and density of states of various materials. It is also possible to obtain high quality spectra where, according to the final state rule[102–104], the final state is not influenced by core hole effects, such as for XES, and PES. For example, in our group, the sulfur $L_{2,3}$ XES spectra were calculated in Wien2k for various sulfates[105] and sulfides[106]. DFT calculations of the PES spectra of various polymorphs Ga_2O_3 were performed in literature,[57] with a very accurate description of the experimental spectra obtained. Chapters 5 and 6 present results of DFT-calculated PES and XES spectra for β-Ga_2O_3. However; in XAS, the final state consists of a bound core-excitonic state (the core hole and electron in the CB), and in RIXS, there is a valence-excitonic state (electron in the CB and hole in the VB) in the final state. The electron-hole interactions cannot be described by DFT, and additional approaches are required.

The Bethe-Salpeter Equation (BSE)[107] is generally used in condensed matter physics to describe neutral particle-hole excitations. The excited system with a core/valence exciton is described in the framework of linear response theory and Green's functions where the x-ray photon is treated as a perturbation. The BSE Hamiltonian is given by:

$$\hat{H}_{BSE} = \hat{H}_e + \hat{H}_h + \hat{H}_{eh} \qquad (2.23)$$

where $\hat{H}_e$ is the single-particle electron Hamiltonian, $\hat{H}_h$ is the single-particle hole Hamiltonian, and $\hat{H}_{eh}$ is the electron-hole interaction Hamiltonian. $\hat{H}_e$ is essentially the Kohn-Sham Hamiltonian $\hat{H}_{KS}$ with some corrections applied as described in Ref.[108]. $\hat{H}_h$ is given by:

$$\hat{H}_h = \epsilon_c + \chi + i\Gamma$$

<div align="right">(2.24)</div>

where ϵ_c is the binding energy of the core hole, χ is the spin-orbit splitting, and Γ is the lifetime broadening. $\hat{H}_{eh}$ is the sum of the direct ($\hat{V}_D$) and exchange ($\hat{V}_x$) interaction terms:

$$\hat{H}_{eh} = \hat{V}_D + \hat{V}_x \qquad (2.25)$$

In OCEAN, to evaluate the BSE Hamiltonian, rather than integrating over the Brillouin zone, the integrals are replaced by a finite k-point mesh of electron and hole states.[63] The size of this k-point mesh is one of the inputs that must be supplied prior to starting the calculation. The number of conduction bands included in the calculation is also finite, and is a parameter supplied as an input as well. In OCEAN, the BSE calculations are performed within the Tamm-Dancoff approximation,[109] where the coupling between excitations and de-excitations is neglected.

So, to obtain the XAS and RIXS spectra, the ground-state electron density is first calculated. Then, the BSE Hamiltonian is constructed from the DFT Kohn-Sham Hamiltonian for the electrons, the Hamiltonian for the holes, and the Hamiltonian describing their interactions. Upon solving it, final spectra can be obtained. More details of the BSE approach and linear-response formalism as implemented in OCEAN can be found in literature such as Refs [63,108,110]. In Chapter 6, the XAS, XES, and RIXS spectra calculated using OCEAN are presented.

2.3 Application of Ga₂O₃ as a buffer layer in Cu(In,Ga)Se₂ – based thin film solar cells

In solar cells, light is converted into electricity by the photovoltaic effect: if the incident photon has an energy greater than the bandgap of the material, $hv > E_g$, an electron will be ejected from the VB into the CB, creating an electron-hole pair. A potential difference is applied, and after attaching a load, a closed electrical circuit is created such that the electron-hole pair doesn't recombine, and so that there is one direction in which the electrons flow (the holes flow in the opposite direction) and not simply an accumulation of charge on the surface. This voltage is created by a p-n junction, made of either two different layers of the same material but with different doping (homojunction), or made of two different materials (heterojunction). Typically, electrons flow through the n-type layer towards the front contact, and holes flow through the p-type layer towards the back contact, although the role of front and back contact can be reversed in some materials. The front and back contacts are the metal contacts which are attached to a load to complete the electric circuit. Figure 2.9 shows a schematic diagram of the p-n junction:
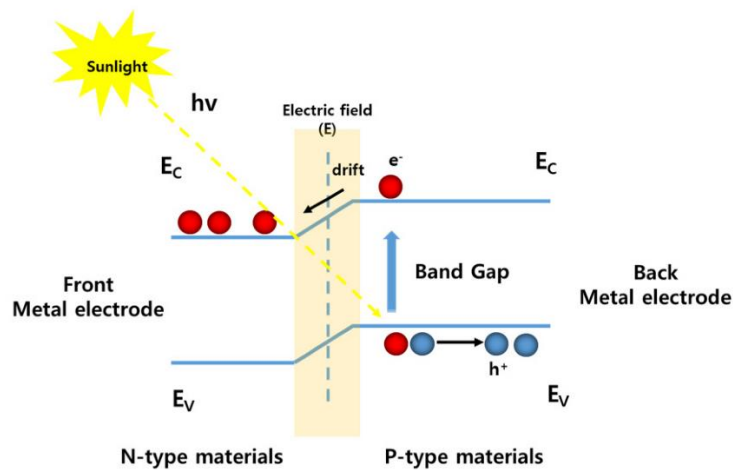
Figure 2.9. Schematic of the p-n junction in solar cells. Figure reproduced from Ref. [111].

The most commonly used solar cells are crystalline Si solar cells, where the p-n junction is made by different doping (n-type Si is most often doped with P and p-type Si with B). It is currently

the most dominant type of cell used because of the high efficiencies (27.6% is the current world record for single crystal cells[112]) as well as the relatively low cost. However, for many decades, thin-film solar cells, such as amorphous silicon (a-Si)[113], cadmium telluride (CdTe)[114] and copper indium gallium diselenide (Cu(In,Ga)Se$_2$, CIGSe)[115] have been studied in parallel. Among the thin-film materials relevant for industry, CIGSe-based cells have the highest efficiency and are comparable to Si (the current world record for CIGSe is 23.6%).[112] CIGSe has a high absorption coefficient. This means that much smaller amounts of CIGSe are used (1-2 μm) compared to Si (160-190 μm). Another advantage of CIGSe is that its bandgap can be modified by varying the Ga/(Ga+In) (GGI) ratio making better use of the solar spectrum: the bandgap is 1.04 eV for CuInSe$_2$[116] and goes up to 2.49 eV for CuGaSe$_2$[117]. In addition, thin-film solar cells are lighter and more flexible than Si-based solar cells.

In a simplified picture, in CIGSe-based solar cells, there is a p-n junction where the CIGSe absorber is of the p-type, while the buffer material is of the n-type. However, this description is only considering the bulk of the materials, and cannot accurately describe the absorber and buffer surfaces, as well as their interface. Below the absorber is the back contact made out of Mo, which is typically 0.5-1 μm thick. The Mo is placed on a substrate, which is most often made out of soda-lime glass. The buffer layer is typically made out of CdS. Above the buffer is the front contact, which is also called the window layer, and is made of a bilayer of transparent conductive oxides (TCOs), typically ZnO and ITO (indium tin oxide). Figure 2.10 shows a schematic of the cross section of a CIGSe solar cell:
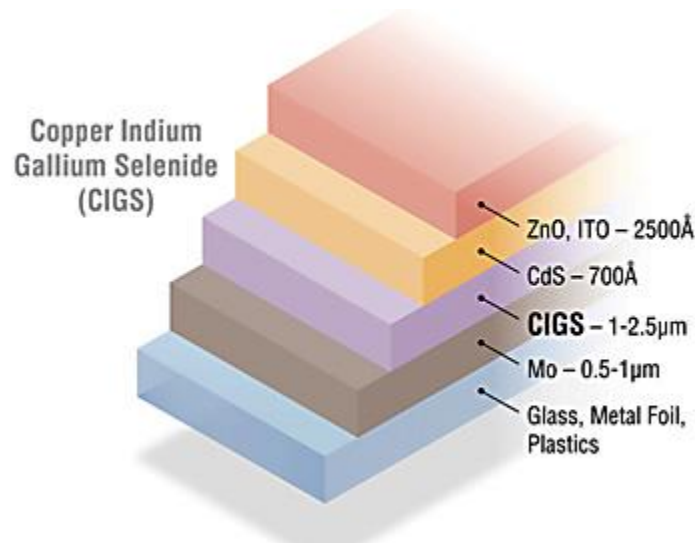
Figure 2.10. Schematic of the CIGSe solar cell, reproduced from Ref.[118].

In 1993, beneficial effects of Na residue from the soda-lime glass substrate on the solar-cell efficiency were observed[119]. Since then, it has been an active area of research to understand and optimize the incorporation of alkali metals in CIGSe. The highest efficiency CIGSe solar cells have been achieved by application of alkali post-deposition treatments (PDT) to the CIGSe after its growth: 20.4% has been achieved with KF-PDT[120], 22.6% with RbF-PDT,[121] and 23.35% with CsF-PDT.[43]

Although the buffer layer is most often made of CdS, there are several disadvantages of using it. Cd is a toxic material, with its use banned in several countries (for example Japan), and the chemical bath deposition (CBD) process which is used to deposit CdS onto CIGSe produces waste water which needs to be properly handled[122,123]. Moreover, the CBD cannot be performed in vacuum, which interrupts the (otherwise) vacuum-based process chain[16,123]. There is also parasitic absorption, i.e., when the photon is absorbed but an electron-hole pair is not generated, at shorter wavelengths of the solar spectrum. Thus, alternative buffer layers are being developed, and in fact the current world records for mini modules and lab-based cells use sputtered $Zn(O,S)$[124] or $CBD-Zn(O,S,OH)$[43] buffers, respectively.

In this dissertation, samples with radio-frequency (rf) sputter-deposited Ga_2O_3 as the buffer layer were investigated. Ga_2O_3 was chosen due to its large band-gap of 4.4-4.9 eV (which reduces the parasitic absorption), and to have a "dry" production process without interrupting the vacuum-based process chain. RbF PDT was applied to the CIGSe, and for half of the samples, an additional rinsing step was applied (see Chapter 4 for more details). The complete solar cell was made similarly to that shown in Figure 2.10, and showed efficiencies of ~13% for the rinsed samples. In Chapter 4, the chemical structure of the rinsed and non-rinsed CIGSe absorbers, the Ga_2O_3 buffer, and their interface is investigated, while in Chapter 5, measurements of the valence band of the Ga_2O_3 buffer are presented.

2.4 Crystal structure, Brillouin zone, and band structure of β-Ga$_2$O$_3$

In this thesis, Ga$_2$O$_3$ samples with two different morphologies are studied: nanocrystalline thin-films (Chapters 4 and 5), and single crystals (Chapters 5 and 6). Crystalline Ga$_2$O$_3$ was first discovered to exist as five different polymorphs in 1952: α, β, γ, δ, and ε.[125]. Various studies have conclusively shown that β-Ga$_2$O$_3$ is the most stable polymorph under standard temperature and pressure. Thus, most research has focused only on β-Ga$_2$O$_3$. Although our collaboration partners have shown that the nanocrystalline thin-film samples are a mixture of α-Ga$_2$O$_3$ and β-Ga$_2$O$_3$, here, the sole focus is on the geometry and electronic structure of β-Ga$_2$O$_3$.

The crystal structure of β-Ga$_2$O$_3$ is monoclinic, with lattice parameters $a = 12.23$ Å, $b = 3.04$ Å, and $c = 5.80$ Å. The angle between the **a** and **c** axes, β, is 103.8°, while the angles between the other axes are 90°.[126–128] Figure 2.11 shows the (conventional) unit cell of β-Ga$_2$O$_3$.
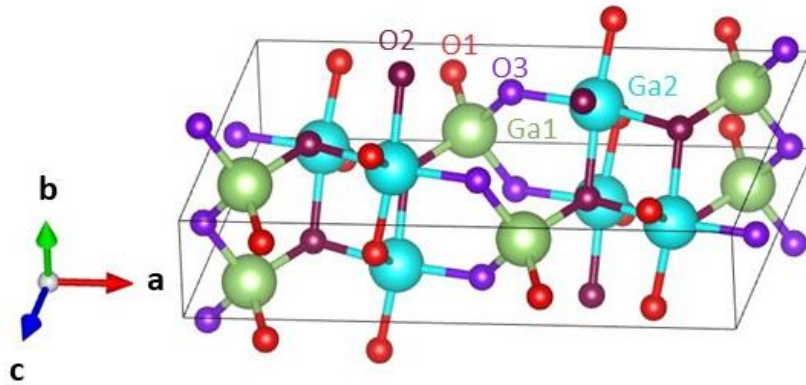
Figure 2.11. The conventional unit cell of β-Ga$_2$O$_3$ (see Refs.[128] and [129]). Tetdrahedrally-coordinated Ga atoms (Ga1) and octahedrally-coordinated Ga atoms (Ga2) are shown in green and blue, respectively. Inequivalent O atoms are shown in red (O1), maroon (O2) and purple (O3). The crystal structure was produced using the VESTA software.[130]

Following Ref. [128], the unit cell vectors of the conventional unit cell are introduced as follows:

$$\boldsymbol{a} = a\hat{x}$$

$$\boldsymbol{b} = b\hat{y}$$

$$\boldsymbol{c} = c\,cos\beta\hat{x} + c\,sin\beta\hat{z}$$

Here, $\hat{x}$, $\hat{y}$, and $\hat{z}$ are unit vectors parallel to the Cartesian x, y, and z axes.

Figure 2.11 shows that there are 2 inequivalent Ga atoms: those that are tetrahedrally-coordinated are labeled as Ga1 while those that are octahedrally-coordinated are labelled as Ga2. There are also 3 inequivalent O atoms, depending on how they are bonding with the Ga atoms: O1 has 2 bonds with Ga2 and 1 bond with Ga1, O2 has 3 bonds with Ga2 and 1 bond with Ga1 (making it octahedrally-coordinated), and O3 has 1 bond with Ga2 and 2 bonds with Ga1 (making it tetrahedrally-coordinated).

The conventional unit cell is constructed from the primitive unit cell shown in Figure 2.12 below:
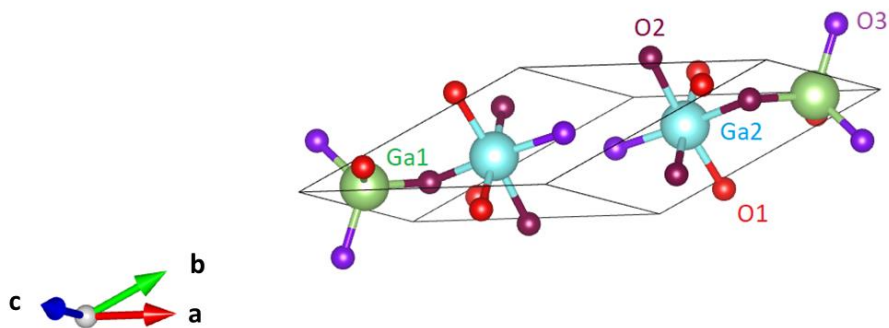
Figure 2.12. The primitive unit cell of β-Ga_2O_3 (see Ref.[128]). Tetdrahedrally-coordinated Ga atoms (Ga1) and octahedrally-coordinated Ga atoms (Ga2) are shown in green and blue, respectively. Inequivalent O atoms are shown in red (O1), maroon (O2) and purple (O3). The crystal structure was produced using the VESTA software[130].

The Brillouin zone can be constructed from the primitive unit cell, and is reproduced from Ref.[17] below:
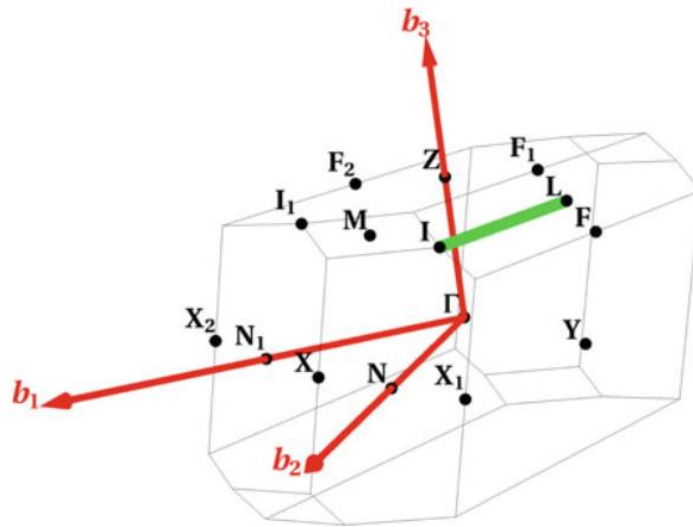
Figure 2.13. The Brillouin zone of monoclinic β-Ga$_2$O$_3$, reproduced from Ref.[17]. The high-symmetry points are labeled. The reciprocal lattice vectors are shown in red, and the I-L line is marked in green.

The reciprocal lattice vectors are shown in red, and the high-symmetry points, the coordinates of which are given in Ref.[17], are marked. The same points are used for the k-path of the k-resolved bandstructure of β-Ga$_2$O$_3$ shown in Figure 2.14 below.
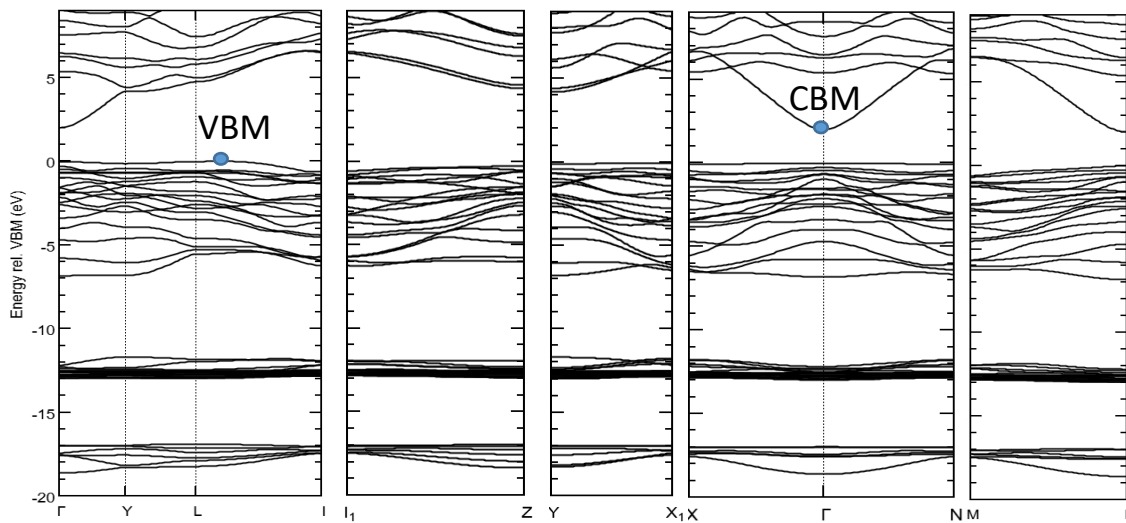
Figure 2.14. The k-resolved bandstructure of β-Ga_2O_3, calculated in Wien2k. The zero of the energy scale corresponds to the valence band maximum. The valence band maximum (VBM) and conduction band minimum (CBM) positions are marked by blue circles.

In Figure 2.14, the positions of the high-symmetry points in reciprocal (k) space are shown on the x-axis, and the energy relative to the VBM is shown the y-axis. There are three main regions: the upper valence band region at 0 to 7 eV below the VBM, and the Ga 3d and O 2s regions at ~ 12 eV to 13 eV and ~ 17 eV to 20 eV below the VBM, respectively. The Ga 3d and O 2s display some dispersion with k, so they cannot simply be treated as core-levels. They are often referred to as semi-core states and are known to influence the (upper) VB structure[57,131]. A portion of the conduction band near the conduction band minimum (CBM) is also shown, and one can see that the CBM is at the Γ point. Meanwhile, the VBM is located on the I-L line, so β-Ga_2O_3 has an indirect band-gap. The I-L line is marked in green in Figure 2.14, to shown that the VBM lies on this line.

This band structure corresponds to what was reported earlier in literature for DFT calculations[21,128,132]. Bandgaps are usually underestimated by DFT in the LDA or GGA approximation[133], as well as the position of the semi-core states with respect to the VBM.[57] Both effects are evident in Figure 2.14, while the other features of the bandstructure are well reproduced. Thus, in this thesis, the bandgaps are not reported from the above bandstructure.

3. Experimental setup

3.1 Laboratory-based setup

All of the XPS and XAES measurements were performed at the Materials for Energy (MFE) Laboratory, which is located at the KIT light source. Figure 3.1 shows a picture of the MFE Lab, with the key components labeled:
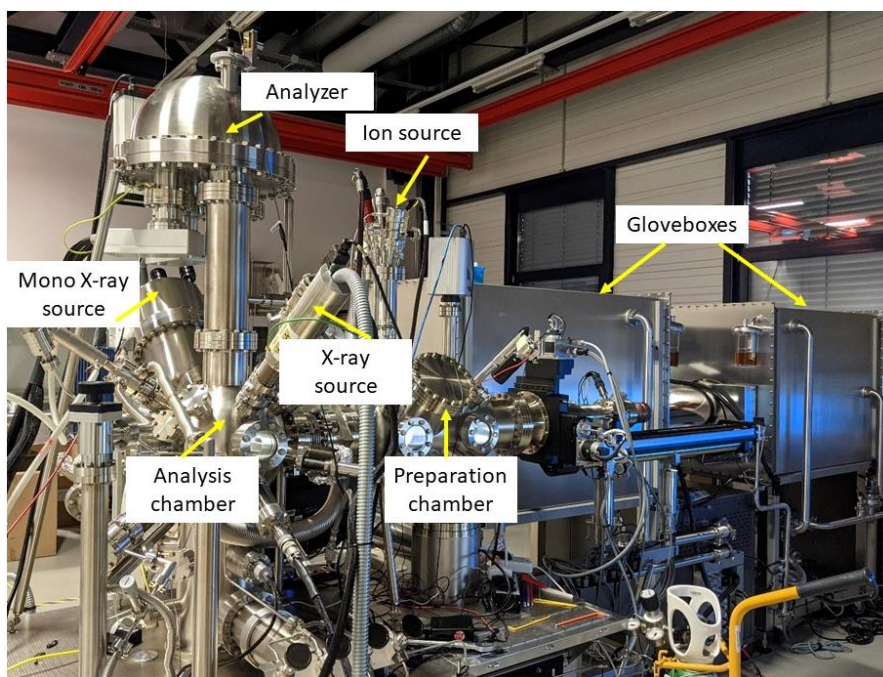
Figure 3.1. MFE lab, showing the key components used for the measurements presented in this dissertation.

Samples and chemicals are stored in the Ar- filled gloveboxes to avoid air exposure. Most of the sample preparation was done in the glovebox as well, except for when preparing the cleaving sample holder for the experiments presented in Chapter 5. The samples are directly introduced to the UHV system through the load lock (the gloveboxes are connected to the load lock, which is not visible in Figure 3.1), transferred to the preparation chamber, and finally to the analysis chamber where XPS and XAES measurements are performed. There are two x-ray sources: the Scienta Omicron DAR 450 twin anode non-monochromatized x-ray source (of which only Mg

K_α is used), and the SIGMA Surface Science MECS monochromatized x-ray source (Al K_α). Photoelectrons and Auger electrons are detected by the Scienta Omicron Argus CU electron analyzer.

When real-world samples such as solar-cell samples are investigated, they are usually studied in their as-received form. Such is the case for the measurement results presented in Chapter 4. However, a low energy Ar^+-ion treatment may also be performed to reduce the surface adsorbates (C and O) on the sample surfaces. Using the FOCUS FDG 150 ion source, a 1 hour long 50 eV ion treatment was performed on the β-Ga_2O_3 single crystal to study surface defect states (see Chapter 5).

3.2   Synchrotron-based setup

3.1.1   X-SPEC beamline at the KIT Light Source

HAX(PES) measurements were performed at the X-SPEC beamline[62] at the KIT light source. As mentioned in Chapter 2, the X-SPEC beamline allows to perform measurements in the photon energy range 70 eV – 15 keV, thus allowing to obtain both bulk and surface-sensitive information about the samples. For HAXPES measurements ($h\nu = 2.1$ keV or higher), the photoionization cross section rapidly decreases with increasing photon energy[134]. So, it is important to have a high photon-flux synchrotron-based x-ray source. Figure 3.2 illustrates the beamline layout of X-SPEC:
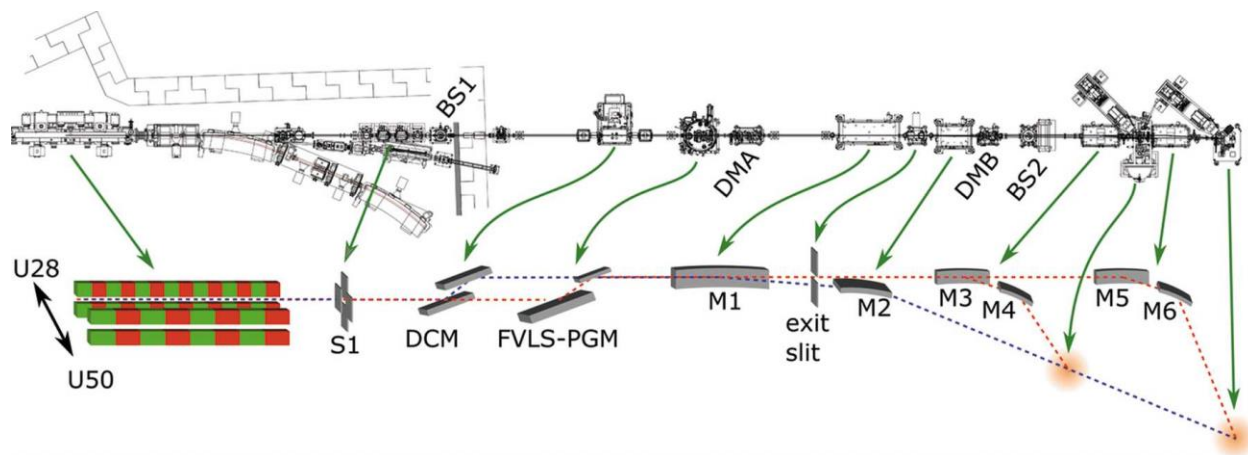
Figure 3.2. Schematic layout of the X-SPEC beamline, with a bird's eye view of the design drawing (top), and the schematic of the most important components in the beamline (bottom). Some key components are: the undulator source with two magnetic structures (U28 and U50), the hard x-ray monochromator (DCM), the soft x-ray monochromator (FVLS-PGM), the two hard X-ray mirrors (M1 and M2), and the two pairs of soft x-ray mirrors, used to focus the beam into the UHV endstation (M3 and M4), and the in-situ endstation (M5 and M6), respectively. The path of hard x-rays is shown in blue, and the path of soft x-rays is shown in red. Figure reproduced from Ref.[62].

In addition to the wide photon energy range, one of the main assets of the X-SPEC beamline is the ability to perform measurements with both hard and soft x-rays at the same sample spot position. X-rays are generated by the double undulator structure shown on the left of Figure 3.2, which is placed in one of the straight sections of the storage ring, as shown in Figure 2.6. It consists of two magnetic structures of period length 28 mm (U28) and 50 mm (U50), which are used for hard and soft x-rays (above and below 580 eV), respectively[62]. For hard x-rays, all of the soft x-ray components are moved out of the beam, and vice versa. Hard x-rays are monochromatized by a double-crystal monochromator (DCM) with pairs of Si (111) and Si (311) crystals. The higher harmonics of the Si (111) crystal are also used for higher resolution measurements at high energies (for example, the Si (333) reflection is used for measurements at 6.3 keV presented in Chapter 5), but the photon flux is significantly decreased as a result. Then, the collimated hard x-ray beam is focused by two mirrors (M1 and M2) onto the endstations.

The soft x-rays are monochromatized by a focusing variable-line-space plane-grating monochromator (FVLS-PGM). In the PGM, one grating can be chosen to cover the whole energy range. Two pairs of mirrors focus the soft x-ray beam onto the endstations: M3 and M4 for the UHV endstation, and M5 and M6 for the in-situ endstation. X-SPEC has two endstations: in the first one, samples are studied under UHV. All measurement results presented in this dissertation were performed at the UHV endstation. There is also another endstation, where samples can be studied at or above atmospheric pressures, by separating their environment from the UHV environment of the analysis chamber. In Figure 3.2, the path of the hard x-rays is shown in blue, and the path of the soft x-rays is shown in red.

In the (HAX)PES measurements, photoelectrons are detected by the Phoibos 225 electron analyzer (SPECS), and are collected at 90° with respect to the incoming x-ray beam.[62] The x-ray source is linearly polarized, in contrast to laboratory-based XPS where the source is unpolarized. Thus, the electrons are collected parallel to the photon polarization vector.

XAS, XES, and RIXS are also all possible measurement techniques at X-SPEC. However, the O K RIXS data of Ga_2O_3 (Chapter 6) for this thesis were collected with the SALSA endstation at Beamline 8.0.1 of the Advanced Light. The next section will briefly introduce Beamline 8.0.1 and SALSA.

3.1.2 SALSA endstation at Beamline 8.0.1 at the Advanced Light Source, Berkeley

All the XAS, XES, and RIXS measurements in this thesis were performed at the SALSA endstation of Beamline 8.0.1 at the Advanced Light Source (ALS), Lawrence Berkeley National Laboratory. Figure 3.3 shows a schematic layout of Beamline 8.0.1:
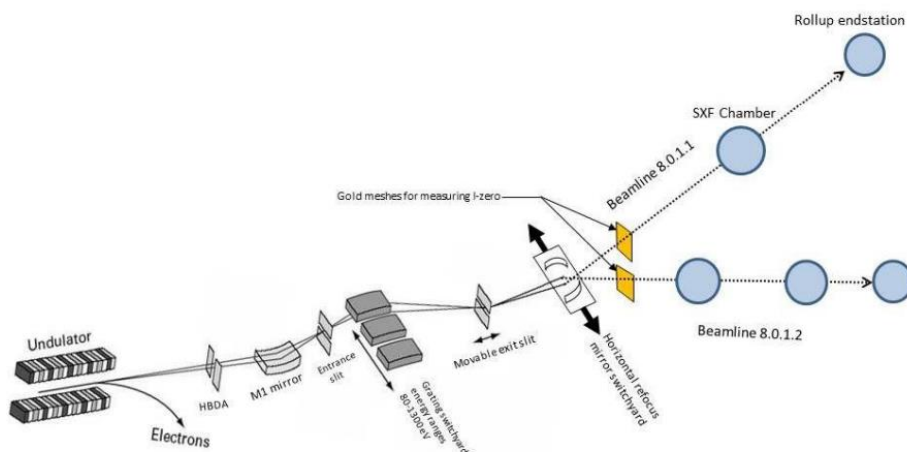
Figure 3.3 Schematic layout of Beamline 8.0.1. Some of the key components are: the undulator, mirrors, entrance slit, spherical grating monochromator (SGM), and exit slit. There are two endstations at Beamline 8.0.1.1: the stationary SXF endstation, and a rollup spot that can be used by "rollable" endstations, i.e., SALSA. Figure reproduced from Ref.[135].

Beamline 8.0.1 is a soft x-ray beamline. Similar to X-SPEC at KIT, the x-rays are generated by an undulator structure placed in one of the straight sections of the storage ring. The undulator has a period of 50 mm, and offers the energy range of 80-1250 eV. The x-rays are monochromatized and collimated by the spherical grating monochromator (SGM). Mirrors and apertures direct the beam through the entrance slit, SGM, and exit slit, to either Beamline 8.0.1.1 or 8.0.1.2. Our group is only using Beamline 8.0.1.1, which has two endstations: the SXF endstation is stationary, while SALSA is a rollup endstation (it is "rolled in" for each beamtime). In addition to measuring solid state samples, SALSA also allows to study liquids, gases, and their interfaces by means of its flow-through liquid cell which is separated from UHV by a thin window membrane.[136]

The SALSA endstation has a high-resolution, high-transmission x-ray spectrometer,[137] with an entrance slit-less design, a spherical collecting mirror, a variable line spacing grating, and a soft x-ray CCD. It has a resolving power of 1200 or better, over the photon energy range of 130-650 eV. The spectrometer is optimized for the S $L_{2,3}$, C K, N K, and O K edges, since these compounds are typically present in organic materials, and allows to detect them simultaneously in the appropriate diffraction orders (O K is detected in the 3rd or 4th order).

4 Chemical structure of the Ga₂O₃/Cu(In,Ga)Se₂ interface

The majority of the following chapter is published in ACS Applied Materials and Interfaces. Reprinted with permission from [Pyatenko *et al.*, ACS Appl. Mater. Interfaces 2023, 15, 45, 53113- 53121]. Copyright [2023] American Chemical Society.

4.1 Introduction

As mentioned in Chapter 2, ever since Na residue (from the soda-lime glass substrate) was observed on CIGSe surfaces[119,138–141], optimizing the incorporation of alkali metals in CIGSe has been an active area of research. The alkali-fluoride postdeposition treatments (PDTs) are most often followed by a rinsing step (e.g., with H₂O or an NH₃ solution) which removes excess alkali fluoride.[142–144] Rinsing steps of CIGSe absorber surfaces have been observed to lead to a reduction or even complete removal of alkali metals[145] and, in some cases, even oxides[146,147] from the absorber surface.

Although chemical-bath deposited (CBD) CdS is generally used as the buffer layer in high-efficiency CIGSe-based thin-film solar cells,[121,148–150] , as explained in Chapter 2, there are many problems associated with it, namely the toxicity of Cd, the parasitic light absorption of CdS, and the CBD process interrupting the vacuum-based process chain. With its wide bandgap and optical transparency, Ga₂O₃ is a promising buffer layer material. Previously, a thin Ga₂O₃ layer has also been applied as a passivation layer at the CdS/CIGSe interface, which improved the various solar cell parameters such as the open-circuit voltage (V_{oc}), the short-circuit current density (J_{sc}), and the fill factor (FF), resulting in an efficiency increase of 2.6% (absolute) as compared to the reference cells without Ga₂O₃ passivation layer.[15] Furthermore, amorphous (In₁₋ₓGaₓ)₂O₃ buffer layers (with x ranging from 0.6 to 1) were investigated, achieving efficiencies (~15.8%) close to those of reference cells with CdS buffers (~17.2%) for x = 1 (i.e., pure Ga₂O₃).[53]

In a first trial, our collaboration partners at ZSW used sputter-deposited gallium oxide as a buffer layer for CIGSe absorbers, reaching efficiencies up to ~13.7% (compared to ~17.6% with a CdS reference buffer).[16] Furthermore, replacing i-ZnO in a ZnO:Al/i-ZnO/CdS/CIGSe

structure by sputtered Ga_2O_3 resulted in cell efficiencies of 20.2 % (compared to 20.4% for the reference cell).[23] The absorbers were exposed to a RbF-PDT, as in the CdS-based ZSW process that has led to efficiencies above 22%.[121] Additionally, a rinse in a 1.5 M NH_3 solution to remove surplus RbF, as well as a temperature optimization series for the buffer deposition were performed. Due to the wider band-gap of Ga_2O_3, an increase in J_{sc} compared to reference cells with CdS was observed.[16,23]

This Chapter presents a detailed investigation of the chemical structure of the RbF-PDT CIGSe absorber surface, the sputter-deposited Ga_2O_3 buffer layer, and the Ga_2O_3/CIGSe interface. Particular focus is placed on the investigation of the ammonia-based rinsing step and its impact on the chemical structure of the absorber surface and the buffer/absorber interface, which is substantially more complex than a simple removal of RbF. For this purpose, samples were studied by XPS, XAES, and HAXPES. Findings in this work can be correlated to electrical device parameters as reported in Refs [16,23].

4.2 Experimental details

The investigated samples were prepared at ZSW; the CIGSe absorbers were grown in a high-vacuum chamber by co-evaporating Cu, In, Ga, and Se in an in-line multi-stage process onto a molybdenum/soda-lime glass substrate (for more details see Ref.[151]). The bulk [Ga]/([Ga] + [In]) (GGI) ratio was determined by x-ray fluorescence measurements (XRF) as 0.27, and the integral Cu content was found to be 21.3 at%.

The RbF-PDT was applied in the same high-vacuum chamber without breaking the vacuum after the CIGSe process. Figure 4.1 illustrates how two different sample sets were prepared.
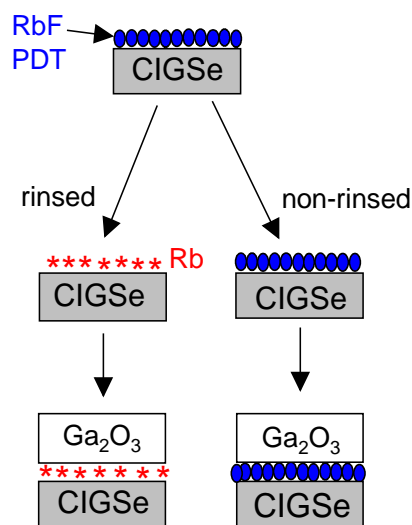
Figure 4.1. Schematic diagram of the preparation of the rinsed and non-rinsed sample sets. The RbF-PDT is depicted by blue circles. The rinse removes excess material of the RbF-PDT, while some Rb remains at the CIGSe surface, and is depicted by red asterisk symbols. Subsequently, Ga_2O_3 is RF-sputter deposited onto both the rinsed and non-rinsed CIGSe absorbers, generating buffer layers of various thicknesses (1, 3, 10, and 100 nm). Although the CIGSe is deposited on a Mo/soda lime glass substrate, it is omitted from the diagram for clarity. Graph reprinted with permission from [ACS Appl. Mater. Interfaces 2023, 15, 45, 53113- 53121]. Copyright [2023] American Chemical Society.

The first set of absorbers was rinsed in 1.5 M NH_3 solution for 30 seconds (referred to as "rinsed" in the following), while the second set was not ("non-rinsed"). Subsequently, Ga_2O_3 was deposited by radio-frequency (RF) magnetron sputtering from a ceramic target at a substrate temperature of 150 °C (details on the Ga_2O_3 sputter deposition process can be found in Refs.[16,23]), generating films with thicknesses d of 1, 3, 10, and 100 nm. Sister samples, processed to full solar cells (i.e., with an approximately 100 nm thick Ga_2O_3 buffer layer and a sputtered i-ZnO/ZnO:Al transparent front contact), showed maximum efficiencies of ~5% for the non-rinsed and above 13% for the rinsed CIGSe absorbers, in comparison to above 16% for CdS-buffered reference devices.[44]

After preparation at ZSW, the samples were briefly exposed to air, sealed in a dry nitrogen atmosphere, and transported to KIT. There, the sealed samples were unpacked and mounted in an Ar-filled glovebox at the MFE laboratory. Without any air-exposure, the mounted samples were

transferred directly from the glovebox into the UHV system for XPS and XAES measurements. XPS measurements were performed with both the Mg K_α and monochromatized Al K_α x-ray sources. The base pressure in the XPS chamber was less than 2×10^{-10} mbar. After the initial XPS and XAES measurements, the samples were transferred to X-SPEC. After a brief exposure to air (less than 30 seconds), HAXPES spectra were measured at a photon excitation energy of 2.1 keV using the Si(111) reflection of the DCM. The base pressure in the HAXPES analysis chamber was less than 5×10^{-10} mbar.

To calibrate the XPS/XAES measurements, the most prominent photoemission and Auger peaks of sputter-cleaned Au, Ag, and Cu foils were used.[152,153] The HAXPES binding energies were calibrated using the Au $4f_{7/2}$ peak[62,152] of a reference Au foil.

4.3 Results and discussion

Figure 4.2 shows the a) HAXPES ($h\nu_{exc} = 2.1$ keV) and b) XPS survey spectra of the (red) rinsed and (black) non-rinsed samples, as well as the 1, 3, and 100 nm Ga_2O_3/CIGSe samples.
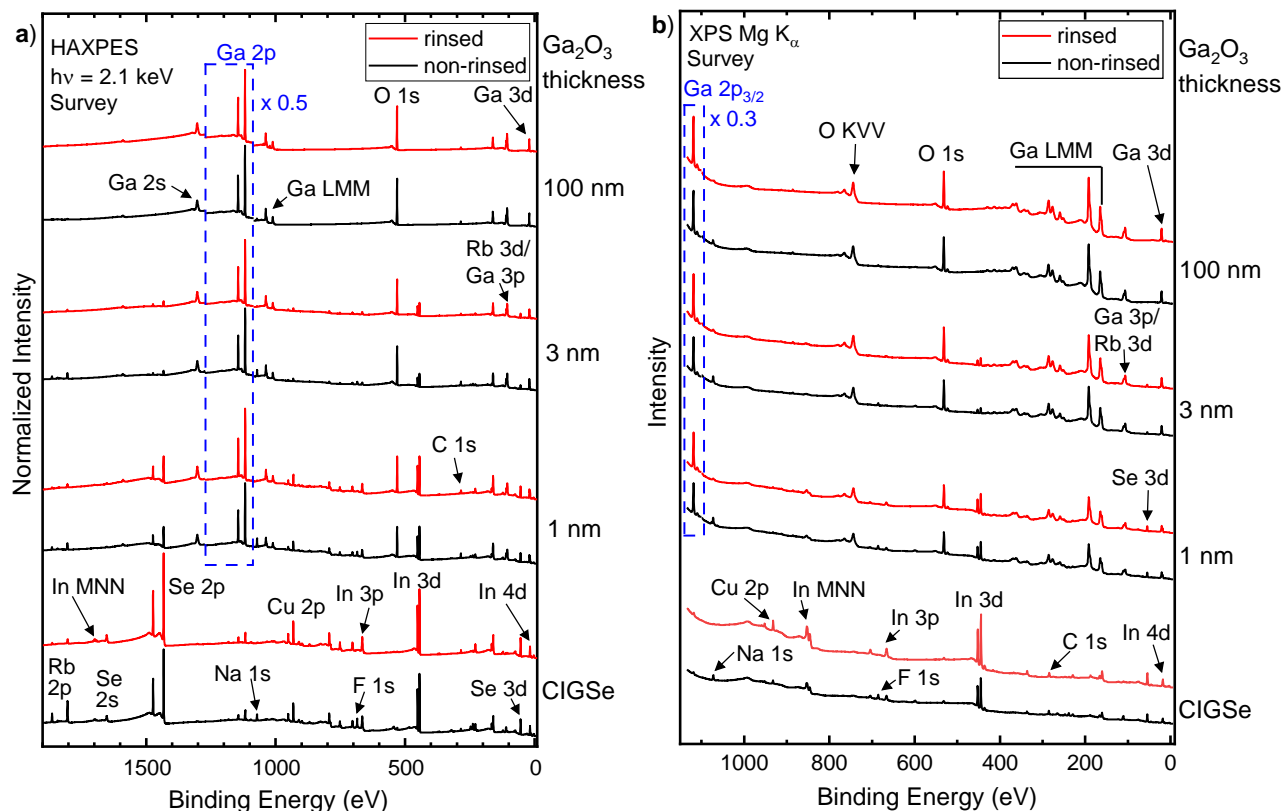
Figure 4.2. a) HAXPES survey spectra, measured at an excitation energy of 2.1 keV, and b) Mg K_α XPS survey spectra, of the CIGSe absorbers with RbF-PDT and the 1, 3, and 100 nm Ga_2O_3/CIGSe interface samples. The red and black spectra correspond to the rinsed and non-rinsed sample series, respectively. The spectra in a) were normalized to their overall integral intensity, while the spectra in b) were normalized to the measurement time. The Ga $2p_{3/2}$ signals of the sputtered Ga_2O_3 buffer layers are multiplied by a factor of 0.5 in a) and 0.3 in b) for better visibility (blue dashed box). Prominent photoemission and Auger peaks are labeled. Graphs reprinted with permission from [ACS Appl. Mater. Interfaces 2023, 15, 45, 53113- 53121]. Copyright [2023] American Chemical Society.

For the CIGSe absorbers, the expected core levels and XAES lines of the absorber elements (Cu, In, Ga, and Se) are detected. Also, the Rb 2p lines are clearly visible in a) (E_{bin} ~ 1800 eV), demonstrating one strength of HAXPES to also detect such deeply-bound core levels; in the case of Rb on CIGSe, uniquely identifying Rb with any other line is extremely challenging (see Figure 4.6 below for an example of the complicated fit for the Rb 3d/Ga 3p detail region). With

increasing buffer layer thickness, the Cu, Se, and In signals are increasingly attenuated by the Ga_2O_3 overlayer, while the Ga and O signals show a strong enhancement.

Due to the higher excitation energy used for HAXPES as compared to laboratory XPS, the kinetic energy of corresponding core-level peaks increases, and thus the HAXPES measurements are less surface-sensitive than the XPS measurements (see Figure 2.3 for the inelastic mean free path as a function of the kinetic energy). For instance, the inelastic mean free path λ as calculated using the Tanuma Powell and Penn (TPP2M) Algorithm[154,155] for the In 3d feature is 3.0 nm for HAXPES and 1.7 nm for XPS, respectively.

In the XPS data in Figure 4.2 b), all absorber-related lines are fully attenuated for the thickest buffer layer (100 nm) samples, while the HAXPES data (Figure 4.2 a)) shows very small Cu 2p, In 3d, and Se 3d signals for the rinsed and non-rinsed sample sets (enabled by the excellent signal-to-noise ratio obtainable at the X-SPEC beamline). This could be due to regions with lower buffer layer thickness (or even a not fully closed buffer layer), a diffusion of the absorber elements into (or onto) the buffer layer, or a combination thereof. Note that a cross-section image of the Ga_2O_3/CIGSe interface[44] suggests that regions with lower buffer layer thickness are unlikely, but cannot be entirely excluded for this sample series. In both absorber spectra, small C and O 1s signals are visible. For the non-rinsed absorber, strong Rb-, F-, and Na-related signals, the latter likely due to diffusion from the soda-lime glass,[139] are also detected.

A comparison of the non-rinsed and rinsed CIGSe absorbers shows that the CIGSe-related lines (e.g., Cu 2p, In 3d, Se 3d) increase after the ammonia rinse by a factor of ~1.3. In parallel, there is a strong decrease of the intensities of the Rb 2p, F 1s, Na 1s, and O 1s lines, while the C 1s intensity increases by a factor of 1.2. Figure 4.3 shows the O and C 1s detail spectra for the non-rinsed and rinsed sample series.
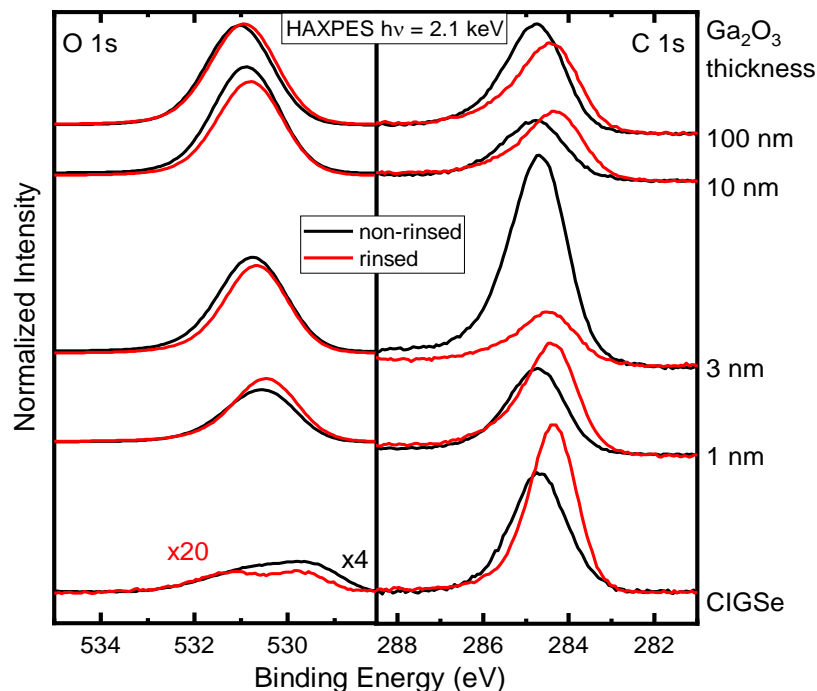
Figure 4.3. O 1s (left) and C 1s (right) core levels for the non-rinsed and rinsed CIGSe and Ga_2O_3/CIGSe samples with increasing Ga_2O_3 thickness, measured with HAXPES at an excitation energy of 2.1 keV. The red and black spectra correspond to the rinsed and non-rinsed sample series, respectively. The O 1s spectra were magnified by a factor of 20 for the rinsed and by a factor of 4 for the non-rinsed CIGSe absorber samples, respectively. Graph reprinted with permission from [ACS Appl. Mater. Interfaces 2023, 15, 45, 53113- 53121]. Copyright [2023] American Chemical Society.

In the O 1s spectra, the signals of both, rinsed and non-rinsed, CIGSe absorbers consist of two components (the peak shapes are asymmetrical), which indicates that oxygen is present in (at least) two different chemical environments. The presence of more than one oxygen species on CIGSe absorbers after RbF-PDT has been reported before as well.[156] The rinse removes a large part of the oxygen, with the signal decreasing by a factor of ~5 for the rinsed sample. Overall, the intensity of the oxygen signals on the absorber surfaces is very low (note the magnification factors of ×4 and ×20, and also see the survey spectra in Figure 4.2). The samples with Ga_2O_3 buffer layer all have the same O 1s peak shape, which increases in intensity and shifts towards higher binding energies for thicker buffer layers. The rinse reverses this effect slightly – all peaks are shifted to lower binding energy for the rinsed samples.

The C 1s signal in the HAXPES spectra varies strongly between rinsed and non-rinsed samples, suggesting that the amount of surface adsorbates present on a particular sample likely depends on the specific conditions under which it was prepared and handled. Again, the intensity of the carbon signals on the absorber surfaces is very low (see Figure 4.2). A slight shift towards lower binding energies of the C 1s peak for the rinsed samples, compared to the non-rinsed samples is also observed.

Figure 4.4 shows the Na 1s signals for the non-rinsed and rinsed sample series.
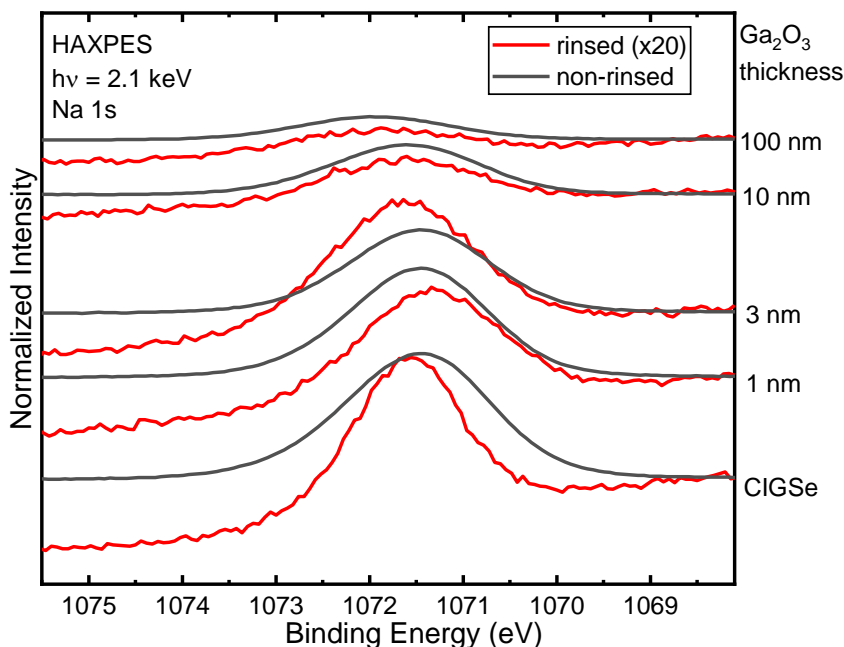
Figure 4.4. Na 1s peaks for the non-rinsed (black) and rinsed (red) CIGSe and Ga_2O_3/CIGSe samples with increasing Ga_2O_3 thickness, measured with HAXPES at an excitation energy of 2.1 keV. The rinsed spectra were magnified by a factor of 20. Graph reprinted with permission from [ACS Appl. Mater. Interfaces 2023, 15, 45, 53113- 53121]. Copyright [2023] American Chemical Society.

The Na 1s signal decreases by a factor of ~20 after the rinse. The peaks decrease with increasing buffer layer thickness and appear to exhibit a similar behavior for the non-rinsed and rinsed samples, although there are some differences depending on the specific sample and how it was prepared (such as the higher Na 1s peak in the 3 nm Ga_2O_3/CIGSe rinsed sample).

The spectral changes in Figures 4.2-4.4 can be interpreted as follows: The rinse removes excess material of the RbF-PDT (i.e., Rb and F), Na, and surface oxides (as will be discussed below)

from the absorber surface. The absorber-related signals (as well as tightly bound CIGSe surface species, e.g., carbon) then increase in intensity due to the reduced attenuation by this surface layer. The larger increase of the C 1s signal for the rinsed absorber may also be due to a more "reactive" surface after the rinse, being more susceptible to the adsorption of carbon-containing species during the subsequent sample handling.

To study the differences in the chemical environment at the surfaces of the non-rinsed and rinsed absorbers, the Ga $2p_{3/2}$, In $3d_{5/2}$, Rb $2p_{3/2}$, and Se 3d spectral regions are presented in Figure 4.5.
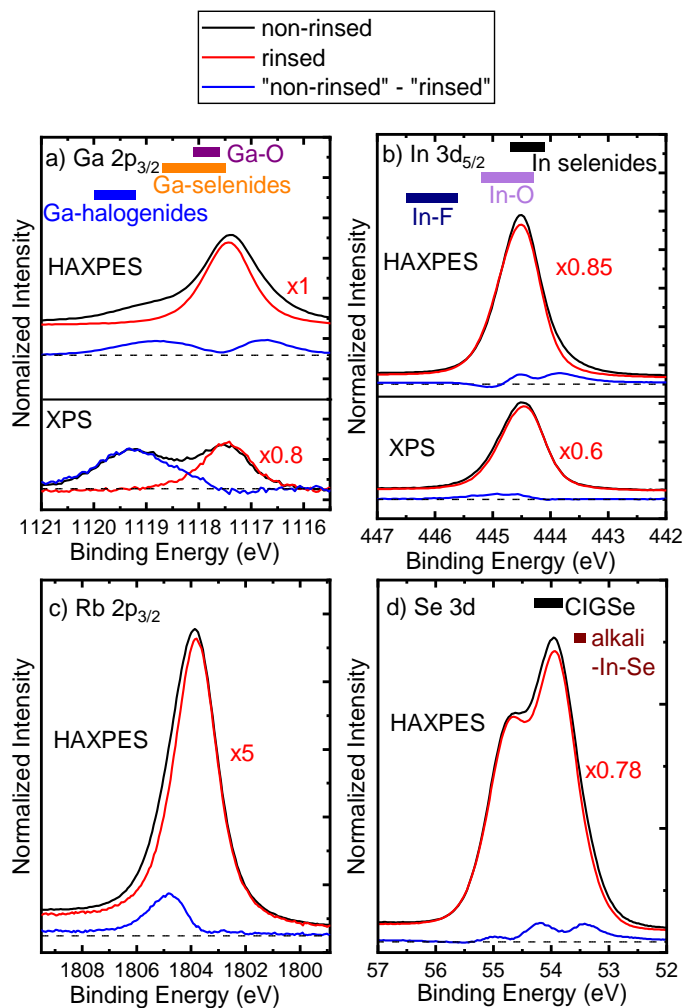
Figure 4.5. HAXPES (hν = 2.1 keV) and monochromatized Al K_α XPS spectra of the a) Ga $2p_{3/2}$, b) In $3d_{5/2}$, c) Rb $2p_{3/2}$, and d) Se 3d regions. The black and red lines correspond to the non-rinsed and rinsed CIGSe absorbers, respectively. All spectra were normalized by the same factors as the survey spectra in Figure 4.2. In addition, the given multiplication factors were applied to the red spectra (rinsed) in Figure 4.5 in order to maximize the contribution of the respective component. The blue lines then show the

difference spectra between "non-rinsed" and "rinsed" surfaces. Colored bars show ranges of literature values of the binding energies for different compounds.[76,142,157] Graph reprinted with permission from [ACS Appl. Mater. Interfaces 2023, 15, 45, 53113- 53121]. Copyright [2023] American Chemical Society.

In Figure 4.5 a), prior to the rinse, a spectral component indicating Ga-F bonds is found (the blue box shows literature values for Ga in GaCl, $GaBr_3$, and GaI_3).[157] After the rinse, this component disappears, as indicated by the difference spectrum (blue). This is in accordance with the F signal, which vanishes after the rinse (to be discussed later below). The Ga-F environment is much stronger in the more surface-sensitive XPS measurement, and the overall Ga $2p_{3/2}$ signal is reduced after the rinse, which can be explained as follows: the RbF-PDT forms Ga-F bonds with Ga at the surface, and the rinse washes away F and (some of) the Ga, reducing the GGI ratio at the surface. This finding is supported by inductively-coupled plasma-mass spectrometry (ICP-MS), where Ga was found in the rinsing residue.[39] This change in Ga content at the surface might impact (reduce) the surface band gap and the performance of the cells.[158]

In Figure 4.5 b), there is no indication of In-F bonds. However, the XPS spectrum shows a weak shoulder at ∼ 445.5 eV that is removed after the rinse, likely due to reduction in In-O bonds. This observation will be discussed in conjunction with Figure 4.7.

There are additional shoulders at low binding energies for the HAXPES Ga $2p_{3/2}$ and In $3d_{5/2}$ spectra of the non-rinsed samples in Figure 4.5 a) and b), respectively. In the case of the Ga $2p_{3/2}$, this additional component can be assigned to the Na $KL_{2,3}L_{2,3}$ Auger transition at ∼1112 eV[76], which is removed after the rinse. The low-binding energy shoulder of the In $3d_{5/2}$ at ∼443.8 eV might be attributed to In in a Rb-In-Se environment present at the surface before the rinse, as will be discussed below.

Figure 4.5 c) shows that the Rb signal decreases by more than a factor of 5 after the rinse. In addition, the difference spectrum clearly highlights that there is an additional spectral component in the non-rinsed absorber at higher binding energies. It is assigned to an Rb-F environment, which, similarly to Ga-F, is removed by the rinse as well. The main spectral component can be attributed to Rb at the CIGSe surface[159,160].

The Se 3d spectra in Figure 4.5 d) indicate only a small contribution from a Rb-In-Se environment before the rinse, indicated by a weak additional spectral component at low binding energies. The binding energy corresponds to that of an alkali-In-Se environment, as reported in Ref.[142]. A narrowing of the line after the rinse is observed, which may indicate that there are several slightly different chemical environments present on the non-rinsed sample. In Ref.[142], a shift of ~0.5 eV was observed for the In $3d_{5/2}$ peak between In in a CIGSe and In in an alkali-In-Se environment. The weak low-binding energy shoulder (443.8 eV) of the In $3d_{5/2}$ in Figure 4.5 b) might be attributed to this chemical environment. In summary, a comparison between non-rinsed and rinsed absorber surface suggests the presence of a Rb-In-Se environment, [142,159] which is subsequently reduced (if not even fully removed) by the here-applied rinse.

To further analyze the effect of the rinse on Rb, Figure 4.6 shows data and fits of the Rb 3d/Ga 3p spectral region measured by monochromatized Al K_α XPS.
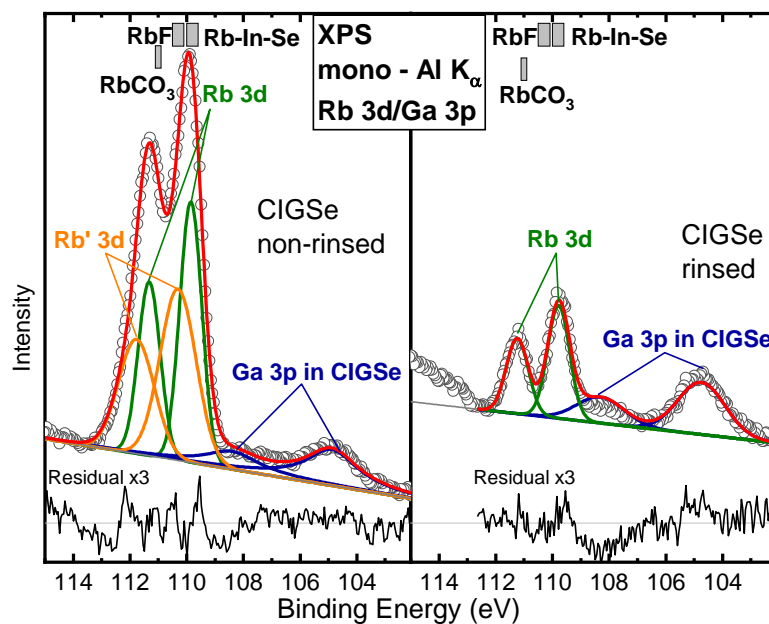
Figure 4.6. Rb 3d/Ga 3p monochromatized Al K_α XPS spectra of the non-rinsed (left) and rinsed (right) CIGSe absorber. Colored components show the fit results: green (Rb 3d), orange (Rb' 3d), blue (Ga 3p in CIGSe), and the sum of the fit (red). The non-rinsed absorber shows two Rb components, while only one Rb component (green) is present for the rinsed absorber. Residuals are shown in light gray below each spectrum, and are multiplied by a factor of 3 for both samples. The grey bars show ranges of literature values of the binding energies for different compounds.[159–161]

53

One can see that due to the overlap of the Ga 3p and Rb 3d spectra, the analysis is more complicated than for the Rb 2p$_{3/2}$ region. It is necessary to perform a multi-component fit, where (as briefly described in Chapter 2), simultaneously with fitting the background by a linear function, the photoelectron peaks are fitted by Voigt functions. The intensity ratio between each spin-orbit doublet is fixed according to the multiplicity 2j + 1 (i.e., 2:1 for the Ga 3p and 3:2 for the Rb 3d peaks), and the spin-orbit splitting, Δ, was used as a fit parameter (resulting in $\Delta_{Rb} \approx$ 1.47 eV for Rb 3d, and $\Delta_{Ga} \approx$ 3.52 eV for Ga 3p). The Gaussian and Lorentzian widths of each spin-orbit doublet (for each chemical environment) were coupled.

Figure 4.6 shows that on the non-rinsed absorber, Rb is present in two different chemical environments: Rb 3d$_{5/2}$ at ∼ 109.9 eV (Rb 3d), and Rb' 3d$_{5/2}$ at ∼ 110.3 eV (Rb' 3d), respectively. The rinsed absorber exhibits only one Rb 3d component, with Rb 3d$_{5/2}$ at ∼ 109.8 eV. Based on results in literature[159–161], the Rb 3d component can be attributed to Rb at the CIGSe surface, while the Rb 3d' component can be attributed to Rb in an Rb-F environment. These results corroborate the HAXPES Rb 2p$_{3/2}$ analysis in Figure 4.5 c).

Figure 4.7 shows the In 4d/Ga 3d spectral region.
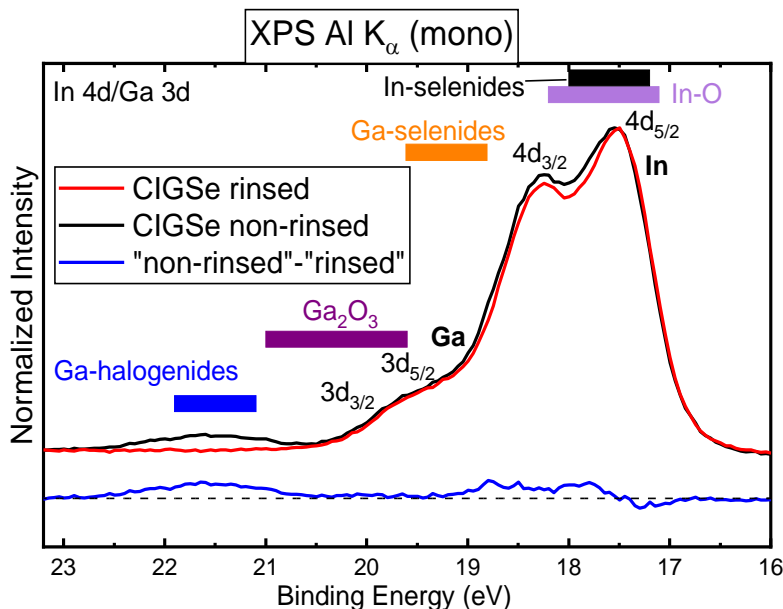
Figure 4.7. Monochromatized Al K_α XPS spectra of the In 4d/Ga 3d region. The black and red lines correspond to the non-rinsed and rinsed CIGSe absorbers, respectively. The spectra were normalized to their overall maximum. The blue line shows the difference spectrum between "non-rinsed" and "rinsed".

Consistent with the findings above, a second Ga 3d component at ~21.5 eV is found for the non-rinsed CIGSe. Again, based on literature values for other Ga-halogenides (GaCl$_3$, GaBr$_3$, and GaI$_3$),[157] this peak is assigned to Ga-F bonds at the surface. This component is not present for the rinsed sample, in agreement with the above-discussed F removal from the surface. The In 4d spectrum in Figure 4.7 exhibits a clear intensity reduction at ~18 eV for the rinsed as compared to the non-rinsed absorber. The blue difference spectrum ("non-rinsed" – "rinsed") highlights this reduction, in agreement with the intensity reduction on the high-binding energy side of the In 3d$_{5/2}$ XPS spectrum in Figure 4.5 b). These additional spectral components are attributed to In-O bonds. Figure 4.5 b) shows that the overall In 3d$_{5/2}$ intensity increases significantly after the rinse. In contrast, the overall Ga 2p$_{3/2}$ intensity decreases, leading to a reduction of the surface GGI ratio as a result of the rinse.

To gain insights into the chemical composition of the Ga$_2$O$_3$ buffer layer and the formation of the Ga$_2$O$_3$/CIGSe interface, the XAES spectra of indium (M$_{4,5}$N$_{4,5}$N$_{4,5}$, Figure 4.8) and gallium (L$_3$M$_{4,5}$M$_{4,5}$, Figure 4.9) were investigated.
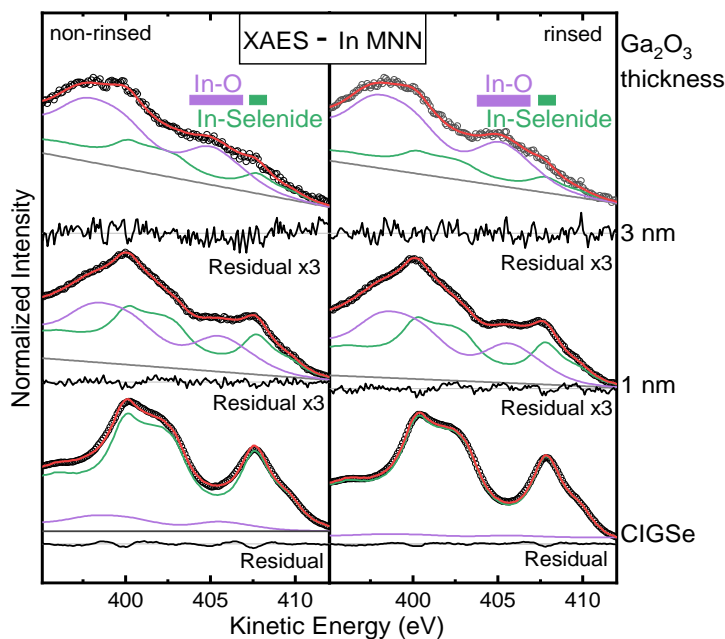
Figure 4.8. Mg K_{α}-excited In $M_{4,5}N_{4,5}N_{4,5}$ for the non-rinsed (left) and rinsed CIGSe (right) and Ga$_2$O$_3$/CIGSe samples with Ga$_2$O$_3$ thicknesses of 1 and 3 nm. Data points are represented as open black circles, individual species (fit components) are represented in green (In-Se bonds) and purple (In-O bonds), and the sum is presented in red. A linear background is shown in gray. Below each spectrum, the residual is given. Literature values for the prominent $M_4N_5N_5$ feature of different compounds[76] are marked as colored bars. Graph reprinted with permission from [ACS Appl. Mater. Interfaces 2023, 15, 45, 53113- 53121]. Copyright [2023] American Chemical Society.

While the two In MNN CIGSe absorber spectra look similar to published spectra,[147,152,156,162] the 1 and 3 nm Ga$_2$O$_3$ thickness spectra show additional intensity in the "valley" at 405 eV, and the overall spectral shape is broader. To analyze these spectral changes, all In MNN spectra were fitted using two single-species In MNN spectra as fit functions (derived from an untreated ZSW absorber sample from another batch). All In MNN fits are thus composed of two components: one with the In $M_4N_{4,5}N_{4,5}$ at $\sim$ 407.7 eV, attributed to In in a CIGSe environment, and the other at 405 – 405.5 eV, attributed to In in an oxide environment. For the 1 and 3 nm Ga$_2$O$_3$/CIGSe samples, an additional Gaussian broadening was applied to the oxide component to describe the presence of several, slightly varying chemical environments. The oxide component is weak in the non-rinsed absorber, and further decreases by about four times in the rinsed absorber. For both the rinsed and non-rinsed 1 and 3 nm Ga$_2$O$_3$/CIGSe samples, a relative increase in the oxide component is observed, which dominates the 3 nm spectra. This finding indicates a significant influence of the sputter deposition of the Ga$_2$O$_3$ layer on the absorber surface, in particular intermixing of absorber elements and the formation of In-O bonds.
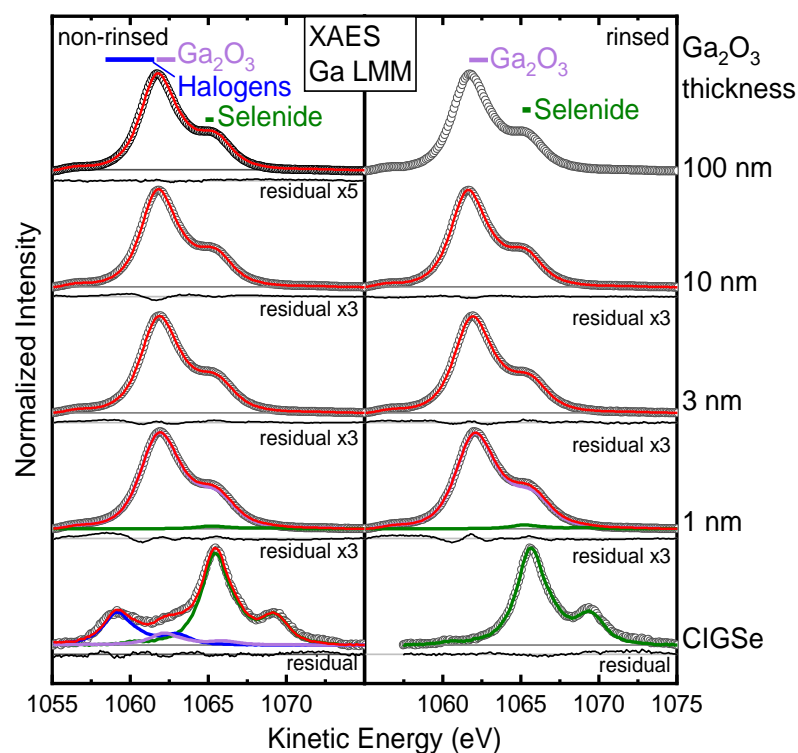
Figure 4.9. Mg K_α-excited $L_3M_{4,5}M_{4,5}$ XAES spectra of gallium for the non-rinsed and rinsed CIGSe and Ga_2O_3/CIGSe samples with increasing Ga_2O_3 thicknesses. Data is represented as open black circles, individual species (fit components) are represented in green (selenide), purple (gallium oxide), and blue (gallium fluoride), and the sum is represented in red. Below each spectrum, the residual is shown. Literature values for the prominent $L_3M_{4,5}M_{4,5}$ feature of different compounds[76,157] are marked as colored bars. Graph reprinted with permission from [ACS Appl. Mater. Interfaces 2023, 15, 45, 53113- 53121]. Copyright [2023] American Chemical Society.

In a similar fashion, the Ga $L_3M_{4,5}M_{4,5}$ region is analyzed in Figure 4.9. A single species Ga $L_3M_{4,5}M_{4,5}$ spectrum (derived from the same untreated ZSW absorber sample mentioned above) was used as the fit function to describe the Ga $L_3M_{4,5}M_{4,5}$ absorber spectra, while for the samples with buffer layer, the measured Ga $L_3M_{4,5}M_{4,5}$ spectrum of the 100 nm rinsed Ga_2O_3/CIGSe sample was used. This approach is necessary due to a significant broadening *and* change in the spectral shape of the Ga $L_3M_{4,5}M_{4,5}$ spectra for various compounds.[157] While the rinsed absorber is composed of one gallium component (main peak at 1065.5 eV), attributed to Ga in a CIGSe environment, the non-rinsed absorber exhibits two additional components. The second component at 1062 eV can be attributed to Ga in an oxide environment, and the third component

at 1059 eV to Ga in a fluoride environment. This interpretation is in agreement with the results shown in Figure 4.5 a) for the Ga $2p_{3/2}$ region.

The Ga LMM spectra of all Ga_2O_3/CIGSe samples are very similar. Only a very small absorber component is present for the 1 nm Ga_2O_3/CIGSe samples, in addition to the main component attributed to Ga in Ga_2O_3. The Ga in the CIGSe environment is not visible for thicker buffer layers. To determine the chemical environment of Ga, the modified Auger parameters (α') for gallium and oxygen were calculated by adding the binding energies of the most prominent photoemission peaks (Ga $2p_{3/2}$ and O 1s) to the kinetic energies of the most prominent Auger peaks (Ga LMM and O KVV, respectively), $\alpha' = E_{bin}(photoemission) + E_{kin}(Auger)$. They are 2180.6 ± 0.2 eV for gallium and 1040.4 ± 0.2 eV for oxygen, respectively, independent of the buffer layer thickness. These values are close to the ones reported in literature for gallium (2180.1-2180.4 eV) and oxygen (1040.7 eV) in Ga_2O_3,[76] suggesting that the dominant species in the buffer layer is indeed Ga_2O_3, independent of the rinse, and that the chemical environment does not change with increasing thicknesses. Notably, there is no indication for the formation of gallium hydroxides, which would be indicated by an additional component in the O 1s spectra (see Figure 4.3).

As a next step, the RbF-PDT-related elements and their evolution as a function of Ga_2O_3 buffer layer thickness is investigated. As already mentioned, the Rb $2p_{3/2}$ peak has a binding energy of ~1804 eV, and hence can only be studied using HAXPES. A clear advantage of measuring this region is that there are no overlapping peaks, in contrast to the Rb 3d/Ga 3p region (as measured with XPS and shown in Figure 4.6 for the absorbers).

Figure 4.10 a) shows the fit analysis of the Rb $2p_{3/2}$ peaks for the non-rinsed and rinsed samples with Ga_2O_3 buffer layer, while 4.10 b) shows the Rb $2p_{3/2}$ peak area as a function of the nominal buffer layer thickness.
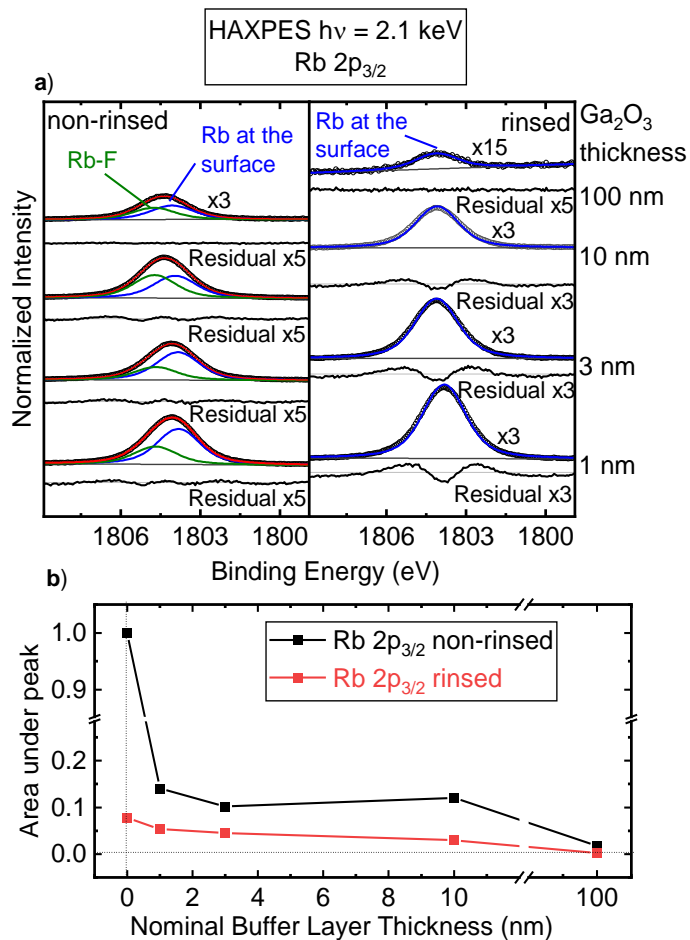
Figure 4.10. a) Data and fits of the Rb $2p_{3/2}$ spectra of the non-rinsed (left) and rinsed (right) CIGSe samples with Ga_2O_3 buffer layer, measured with HAXPES at an excitation energy of 2.1 keV. Data is represented as open black circles, individual species (fit components) are represented in green (Rb-F) and blue (Rb at the surface), and the sum is represented in red. Below each spectrum, the magnified ($\times3$ or $\times5$) residual is shown in light gray. b) Rb $2p_{3/2}$ peak area as a function of the nominal buffer layer thickness, normalized to the intensity of the non-rinsed absorber surface. Data for the non-rinsed and rinsed samples are shown in black and red, respectively. Graph reprinted with permission from [ACS Appl. Mater. Interfaces 2023, 15, 45, 53113- 53121]. Copyright [2023] American Chemical Society.

Figure 4.10 a) demonstrates that a Rb $2p_{3/2}$ signal is visible on all sample surfaces. Note that these measurements are very surface-sensitive: at this excitation energy, the inelastic mean free path of the Rb $2p_{3/2}$ electrons is ~0.8 nm; in contrast, it is ~2.3 nm for the Rb 3d region. Combined with the complications arising from the spectral overlap with the Ga 3p lines, it is

much harder to unequivocally discern the presence of Rb on the Ga_2O_3 buffer layer surfaces from the Rb 3d spectra. In the non-rinsed samples, Rb is mainly present in two different environments, as discussed in Figures 4.5 c) and 4.6: Rb adsorbed on CIGSe and Rb-F, while in the rinsed samples only adsorbed Rb is present.

Figure 4.10 b) shows an overall decrease in the area under the (total) Rb $2p_{3/2}$ peak with increasing buffer layer thickness. This decrease is much weaker than would be expected for an (exponential) attenuation by the Ga_2O_3 overlayer. This discrepancy indicates a diffusion/segregation of Rb in both the rinsed and non-rinsed cases. In the rinsed case, the Rb intensity slowly but steadily decreases with buffer layer thickness. In contrast, the Rb 2p intensity in the non-rinsed series decreases sharply from the absorber to the 1 nm Ga_2O_3 sample, then stays approximately constant up to 10 nm Ga_2O_3, and then further strongly decreases from 10 to 100 nm. In addition, Figure 4.10 a) shows that the relative fraction of the Rb-F component increases with increasing buffer layer thickness in the non-rinsed sample series.

To further investigate the Rb-F diffusion/segregation, the fluorine signals are also studied in detail. Figure 4.11 shows the In 3p and F 1s detail regions, measured with HAXPES. Although it is possible to observe the F 1s peak with XPS, the high signal-to-noise ratio achievable with HAXPES at the X-SPEC beamline helps to clearly detect the small F 1s peak between the (strong) In 3p peaks in the rinsed sample series.
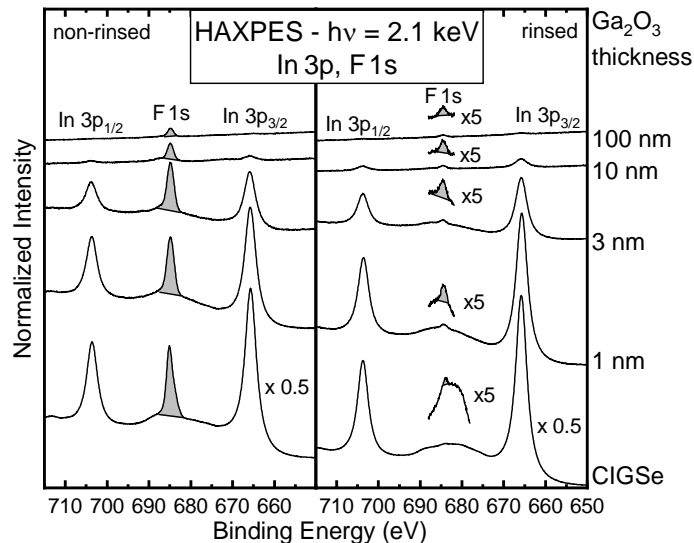
Figure 4.11. In 3p and F 1s region for the non-rinsed (left) and rinsed (right) CIGSe and Ga_2O_3/CIGSe samples with increasing Ga_2O_3 thickness, measured with HAXPES at an excitation energy of 2.1 keV. To highlight the F 1s signal in the rinsed sample series, it is magnified by a factor of 5 and shown in blue above each spectrum. Graph reprinted with permission from [ACS Appl. Mater. Interfaces 2023, 15, 45, 53113- 53121]. Copyright [2023] American Chemical Society.

In the non-rinsed samples, the F 1s peak decreases with increasing buffer layer thicknesses. There is still a clear F 1s peak for the 100 nm non-rinsed sample but no In 3p peaks, indicating a clear diffusion/segregation of F to the Ga_2O_3 buffer layer surface. After the rinse, no (or only a very small) F 1s peak is found, indicating that the rinse removes F from the absorber surface. In contrast, the rinsed Ga_2O_3/CIGSe samples all show a small F 1s peak, which slightly decreases in intensity as a function of buffer thickness. As a possible explanation for the presence of F on the rinsed Ga_2O_3/CIGSe samples, some F might diffuse into the CIGSe absorber (e.g., along grain boundaries) during the RbF-PDT and then diffuse to the Ga_2O_3/CIGSe interface during the sputter deposition process (assisted by the elevated process temperature).

To gain a better understanding of the diffusion/segregation of all the PDT-related elements, as well as to investigate the potentially weak diffusion of the absorber-related elements, an "effective buffer layer thickness" is calculated from the attenuation of the most prominent XPS and XAES peaks. Assuming a homogenous buffer layer with thickness d, the intensity of an XPS/XAES signal would be given by $I = I_0\,e^{-d/\lambda}$, where I_0 is the intensity for the absorber sample, and λ is the inelastic mean free path, calculated using the Tanuma Powell and Penn (TPP2M) Algorithm.[154,155] The "effective buffer layer thickness" is then defined as $d_{eff} = \lambda \ln\left(\frac{I_0}{I}\right)$, and is plotted against the nominal buffer layer thickness in a logarithmic plot. To take into account the energy distribution of the peak intensities, i.e., the broadening of the peaks, rather than taking the peak maxima for I and I_0, an area under the peaks is calculated and taken instead. Figure 4.12 shows a plot of the effective vs nominal buffer layer thickness for the non-rinsed samples (the rinsed samples show very similar results).
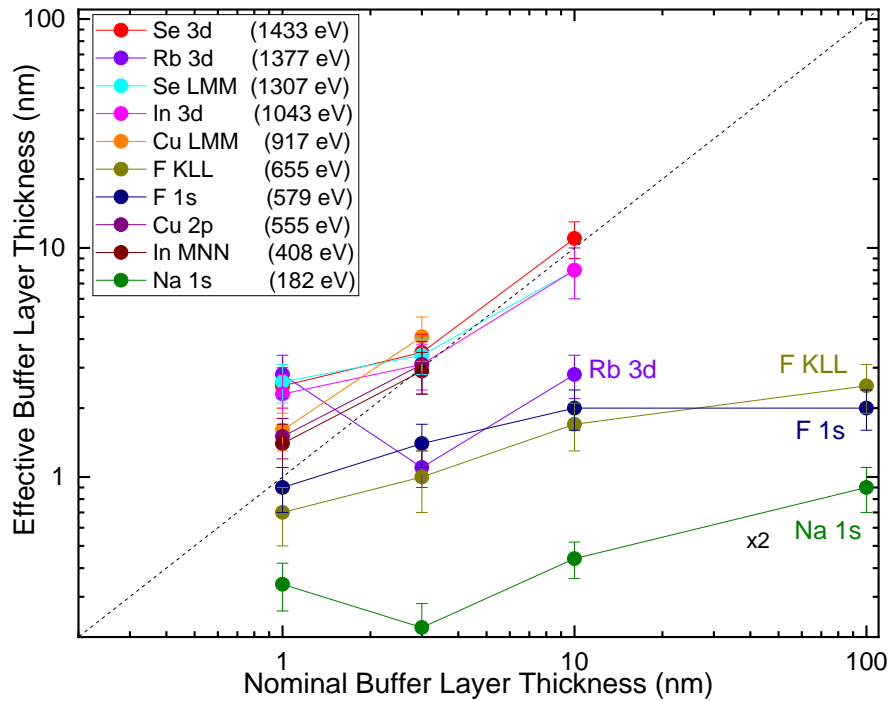
Figure 4.12. Effective buffer layer thickness, d_{eff}, calculated from the attenuation of the different absorber and PDT-related peaks, as a function of the nominal buffer layer thickness, for the non-rinsed samples. The legend shows the different XPS/XAES peaks and their corresponding kinetic energies. While the absorber-related peaks indicate no (or very weak) diffusion, the effective buffer layer thicknesses of the PDT-related peaks are significantly below the dashed line, indicating their diffusion into the buffer layer.

If there was no diffusion, the effective buffer layer thickness would be equal to the nominal buffer layer thickness, and the data points would lie on the straight dashed line shown in Figure 4.12. On the other hand, if there was diffusion, the effective buffer layer thickness would be less than the nominal buffer layer thickness and the data points would lie below the dashed line. One can see that the data points for the absorber-related peaks lie close to this line, suggesting no, or very weak diffusion of these elements. For the 1 nm Ga_2O_3/CIGSe samples, many of the data points of the absorber-related peaks lie above the dashed line, i.e., the effective buffer layer thickness is less than the nominal one. This may suggest that the buffer layer is not completely closed/formed at 1 nm, and there may be some holes.

For the PDT-related elements, i.e., Rb, F, and Na, the data points are clearly below the dashed line, indicating a strong diffusion of these elements into the buffer layer, and corroborating the results discussed above in Figures 4.4, 4.10 and 4.11.

It can be speculated that the large amounts of Rb-F on the non-rinsed absorber and its diffusion into the Ga_2O_3 buffer layer could lead to the observed significantly lower solar-cell efficiencies. Rinsing the CIGSe absorber removes F, some Rb, and associated oxides, and could hence result in optimized interface properties and higher efficiencies.

4.4 Conclusion

In this Chapter, a detailed investigation of the chemical structure of the RbF-treated CIGSe absorber surface, with and without an ammonia-based rinse, as well as their interfaces with a sputter-deposited Ga_2O_3 buffer layer was presented. The rinse removes almost all F and most of the Rb in an Rb-F environment, while some remains at the CIGSe surface. The rinse removes In-O, Ga-O, and Ga-F bonds from the CIGSe surface, decreases the Ga/(Ga+In) ratio at the surface, and removes evidence of a Rb-In-Se bonding environment.

Rb and F are also found on all samples with sputter-deposited Ga_2O_3 buffer layer, with and without rinse (in some cases, only trace amounts of F are observed). During sputter-deposition, a significant amount of In-O bonds is formed. The dominating chemical environment of the buffer layer is Ga_2O_3, independent of the buffer layer thickness and the absorber rinsing.

These findings thus indicate a rather complex chemical interface structure and diffusion/segregation behavior from the absorber to the buffer surface for Rb, F, and Na. This interface structure is substantially modified by applying the rinse, which then also leads to higher solar cell efficiencies. These significant changes in chemical structure are expected to lead to changes in the electronic structure, in particular the conduction band alignment, which would be the subject of future investigations.

5 Determining the valence band maximum of Ga_2O_3

5.1 Introduction

In Chapter 4, the chemical structure of the Ga_2O_3/CIGSe interface in thin-film solar cells was investigated. Understanding the electronic structure, i.e., determining the positions of the CBM and VBM of CIGSe and Ga_2O_3 with respect to E_F, the band bending due to the interface formation, as well as the work function, is likewise (if not even more) important for further improving the efficiencies of the solar cell devices. In this Chapter, the VBM of Ga_2O_3 is studied in detail.

Although Ga_2O_3 is considered to be a TCO, intrinsic (i.e., undoped) Ga_2O_3 has been reported to be poorly conducting or even insulating.[163] Defect-induced states that are responsible for the electrical conductivity of TCOs are expected to appear as a "foot" present at the valence band spectral onset.[22] Results in literature suggest that while intrinsic O vacancies are responsible for the conductivity of undoped Ga_2O_3,[164] doping with Sn[165] or Si[164] can introduce additional defects that significantly enhance its conductivity. Nonetheless, there are still many unanswered questions about the precise role of dopants in the conductivity of Ga_2O_3.

Various factors such as the morphology, crystal structure, and the preparation of the sample surface can all affect the electronic structure and hence the VBM and E_g values. The foot/tail can show up differently in spectra measured at different photon excitation energies, i.e., depending on whether the measurements are more bulk or surface-sensitive. Thus, the photon excitation energy can play a role in the determination of the VB and VBM as well.

In this Chapter, the effects of the various factors on the VBM of Ga_2O_3 were investigated using (HAX)PES for three different types of samples. As a first step, the valence band of the 100 nm Ga_2O_3/CIGSe samples were investigated. Since there is very weak (or even no) diffusion of absorber elements into the buffer layer (see Chapter 4), a cross-section image of the Ga_2O_3/CIGSe interface[23] suggests that the buffer layer is homogenous and of uniform height, with pinholes unlikely, and the inelastic mean free path for the range of excitation energies employed is considerably less than the 100 nm buffer layer thickness (0.5-8 nm, see Table 5.1), these samples were chosen as a model system for nanocrystalline Ga_2O_3.. As will be shown

below, the VB in general, and the VBM in particular, appears to show a dependence on the photon excitation energy for these samples. In addition, a tail is observed in all, especially in the most surface-sensitive measurements. To understand these effects better, the valence band of a UHV-cleaved β-Ga$_2$O$_3$ single crystal was measured. In parallel, DFT calculations for the β-Ga$_2$O$_3$ single crystal were carried out for comparison.

For real-world samples where one wants to remove surface adsorbates such as O and C, without changing or damaging the investigated surface, a low energy Ar$^+$-ion treatment is often used to clean the surfaces. However, depending on the energy of the ions and the duration of the treatment, defects, such as O vacancies, may also be introduced to the surface.[166] Thus, another sample of the β-Ga$_2$O$_3$ single crystal underwent a second surface preparation: it was exposed to a long (~ 1 hour) 50 eV Ar$^+$-ion treatment to study the impact on the valence band as a whole, and on the VBM in particular.

There are several challenges associated with determining the VBM accurately, namely that of inelastic scattering (e.g., phonon scattering), band dispersion, and final state screening effects. While different methods of determining the VBM have been presented in literature, we argue that the effects listed above are best treated by linear extrapolation.[167] Thus, for all results discussed below, the VBM was determined using linear extrapolation of the leading edge. As will be shown and discussed below, all three samples exhibit significant differences in their valence band spectra and different values of the VBM are obtained.

5.2 Experimental details

All (HAX)PES measurements were carried out at X-SPEC. Measurements with soft x-rays (70 - 1000 eV) were performed with the PGM, while the HAXPES measurements were performed using the DCM. The Si(111) reflection of the DCM was used at 2.1 keV and 4.0 keV, and the higher order, Si(333) was used at 6.3 keV.

Table 5.1 shows the inelastic mean free paths (IMFP) for electrons travelling through a Ga$_2$O$_3$ layer as a function of their kinetic energy. The IMFPs were calculated using the Tanuma Powell and Penn (TPP2M) Algorithm[154,155] for the excitation energies at which the VBM measurements

were performed. Since the binding energies are very small for valence band measurements, they can be neglected, and hence the excitation energy can be equated with the kinetic energy.

Excitation Energy (keV)	IMFP (nm)
0.07	0.5
0.1	0.5
0.2	0.6
0.5	1.1
0.8	1.5
1.0	1.8
2.1	3.2
4.0	5.4
6.3	7.9

Table 5.1. IMFP of electrons travelling through Ga_2O_3 for the excitation energies used in the (HAX)PES measurements of the valence band, calculated using the TPP2M algorithm.

Thus, one can see that valence band measurements at 0.1-0.2 keV are very surface sensitive, probing on the order of a few atomic layers. If one or at most several atomic layers are considered as the surface (around 0.3 nm), measurements at 4.0 and 6.3 keV probe 5-8 nm, i.e., more than 10 atomic layers, and can already be considered as giving information on the bulk of the material.

Measurements were first performed on the 100 nm Ga_2O_3/CIGSe samples; these samples were described in more detail in Chapter 4. β-Ga_2O_3 single crystal substrates (of size 10 x 15 mm^2) in the (010) orientation were obtained from Novel Crystal Technology, Inc., Tamura Corporation, where they were grown by the edge-defined film-fed growth method.[168] The samples were doped with Sn to improve their conductivity, resulting in carrier concentrations of 6.3x10^{18} cm^{-3}. The Ga^{3+} ions are replaced by Sn^{4+} ions, which thus act as electron donors and hence increase the conductivity.[165,169] Figure 5.1 shows a schematic diagram of the (010) surface of the β-Ga_2O_3 single crystal.
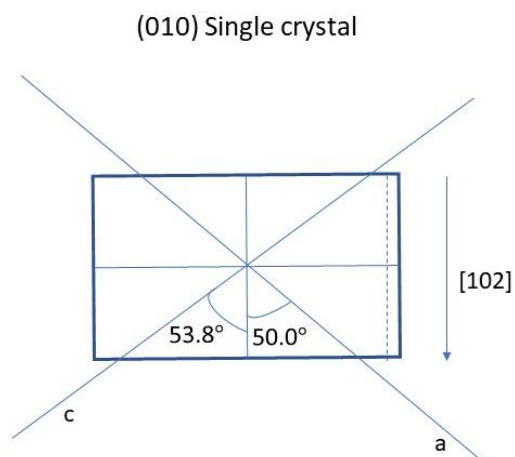
(010) Single crystal

Figure 5.1. Schematic diagram of the (010) surface of the β-Ga$_2$O$_3$ single crystal. The scratch and subsequent cleaving was performed parallel to the shorter side of the sample, which is parallel to the [102] direction, and perpendicular to the (010) surface.

 As the crystals had been exposed to air for a prolonged time period, one of the samples was cleaved in UHV (in the analysis chamber at X-SPEC; see below) prior to measurement. This ensured a clean surface with no surface adsorbates (a small C peak was observed immediately after cleaving, indicating the presence of some C in the bulk of the crystal). Figure 5.2 a) shows the cleaving sample holder and sample and b) shows a diagram of the cleaving process.
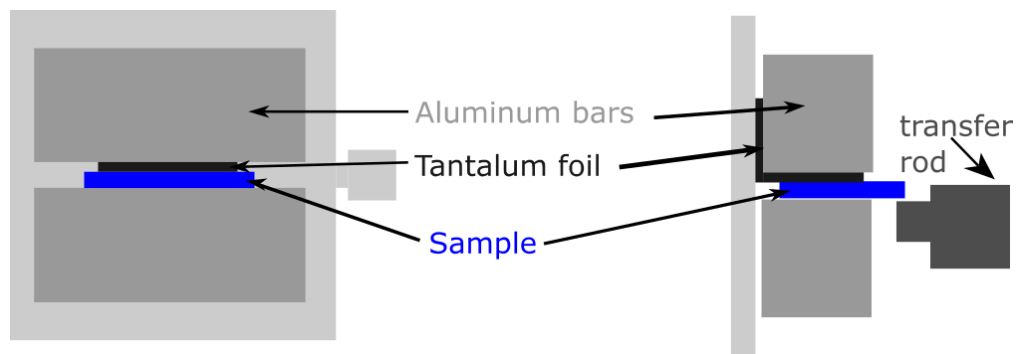
Figure 5.2. a) top view of sample holder and sample b) side view of sample holder, sample, and transfer rod used to cleave the sample.

The sample was mounted onto the sample holder (in air) by securing it with screws attached to the aluminum bars. Then, a scratch was made by a cutter parallel to the shorter side of the sample, which is parallel to the [102] direction, and perpendicular to the (010) surface, as shown in Figure 5.1. The sample and sample holder were then transferred to X-SPEC in an Ar-filled sample container, without any additional air exposure. The sample was cleaved in the analysis chamber of X-SPEC by moving the transfer rod parallel to the direction of the sctrach, as shown in Figure 5.2 b). It is important to keep in mind that the surface after cleaving is different to the (010) surface, which could result in variations in the shape of the valence band and the VBM. However, the WIEN2k calculations (see 5.3) do not taken into account the orientation of the surface, so the effects of the surface orientation were not explored here.

The second crystal was mounted onto a regular sample holder, with the (010) surface facing upwards. It was then exposed to a 1 hour 50 eV Ar^+-ion treatment, which was performed using the ion source in the MFE laboratory. The samples were transferred to X-SPEC in an Ar-filled sample container, without any air exposure. The binding energy of the Au $4f_{7/2}$ peak[62,152] of a reference Au foil was used for energy calibration. The experimental resolution was determined from measurements of the Au Fermi edge at different photon excitation energies, and varies as 0.1-0.7 eV, with the smallest value at photon excitation energy 70 eV, and the largest value at photon excitation energy 6.3 keV.

5.3 Calculations details

The PES spectra of β-Ga_2O_3 were calculated using Wien2k. As was explained in more detail in Chapter 2, Wien2k is a program package that solves the Kohn-Sham Hamiltonian based on the full-potential (linearized) augmented plane-wave ((L)APW) + local orbital (lo) methods.[170] The generalized gradient approximation (GGA), as parametrized by Perdew, Burke, and Ernzerhof (PBE)[96] was used to approximate the exchange-correlation functional. The accuracy of the basis set size is determined by the product of the smallest muffin tin radius (see chapter 2) R_{MT} times the largest k-vector K_{max}, which was set equal to 8. The self-consistent field (SCF) cycle was run with 1000 k points, while the projected density of state (PDOS) calculations were run with 10000 k points.

The PES spectra are calculated according to Ref.[171], where the PDOS are multiplied by the photoionization cross sections at the given excitation energy and polarization as presented in Refs.[172,173] (the analyzer is set parallel to the linearly polarized x-ray source at X-SPEC so the corresponding option is chosen for the calculations). The Ga 3d orbitals are treated as valence orbitals together with Ga 4s, Ga 4p, O 2s, and O 2p.

The PES were broadened with a Gaussian broadening corresponding to the experimental resolution, and a Lorentzian broadening, to account for the lifetime broadening. The Lorentzian broadening was chosen such that the tails in the experiments are best described by the calculations, and resulted in the value 0.15 eV (at all excitation energies). In Figure 5.7 below, the PES spectrum at photon excitation energy 200 eV was broadened with a Gaussian broadening of 0.2 eV, while the one at photon excitation energy 2.1 keV was broadened with a Gaussian broadening of 0.3 eV. The crystal structure of β-Ga_2O_3 was obtained from the Materials Project Database.[174]

5.4 Results and discussion
5.4.1 VBM for the 100 nm Ga_2O_3/Cu(In,Ga)Se$_2$ samples

(HAX)PES spectra were measured in the wide energy range of 0.2-6.3 keV for the 100 nm rinsed and non-rinsed 100 nm Ga_2O_3/CIGSe samples. For clarity of presentation, Figure 5.3 shows the valence bands for a selection of excitation energies for both of the samples:
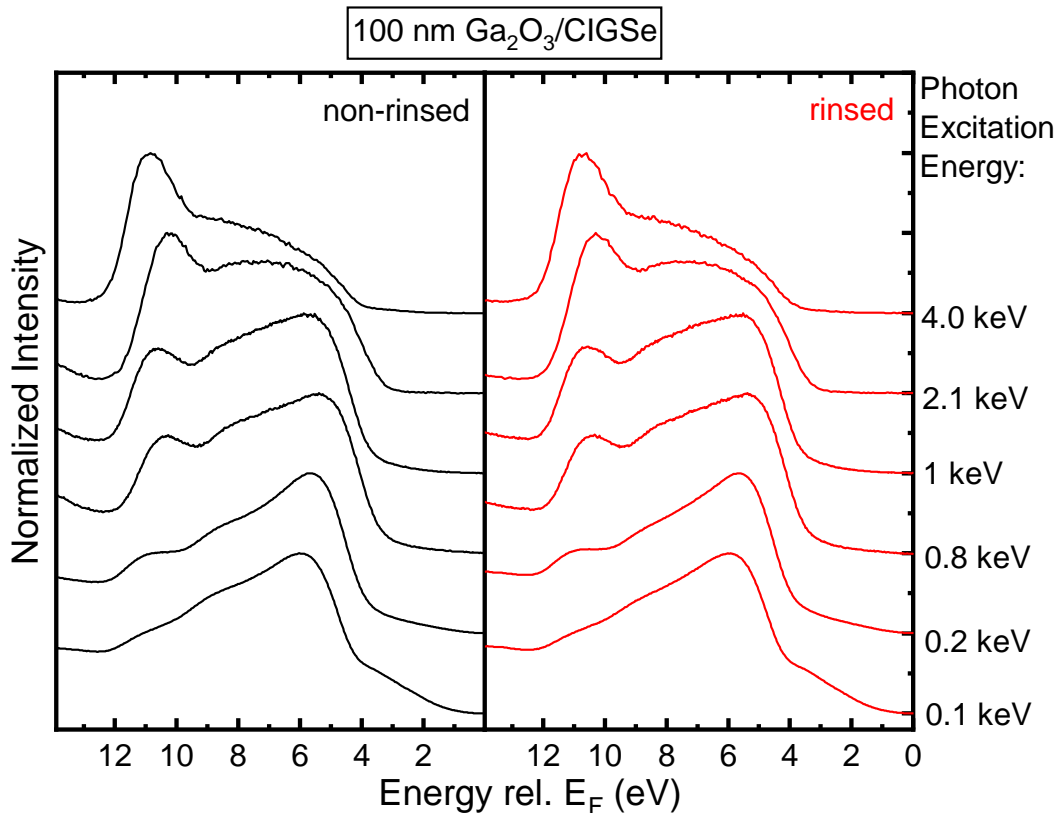
Figure 5.3. Valence bands of the 100 nm non-rinsed (left, black) and rinsed (right, red) Ga_2O_3/CIGSe samples measured with HAXPES at a wide range of photon excitation energies. The spectra were normalized to their peak maxima.

Figure 5.3 shows how the spectral shape changes with excitation energy. The tail between 2 and 4 eV is most prominent in the most surface-sensitive measurement at 0.1 keV, and least prominent in the bulk-sensitive measurement at 4.0 keV. This is not surprising since the tail is likely to be related to surface defects and/or C and O adsorbed at the surface.[59] The overall spectral shape also gradually changes, with the peak at ~ 6 eV dominating the spectra at low excitation energies, and the peak at ~ 11 eV dominating at high excitation energies. This is due to changes in the photoionization cross sections of the involved states as a function of the excitation energy and symmetry (s, p, and d states), and will be discussed in more detail in conjunction with Figure 5.9 below. In addition, no difference in the rinsed and non-rinsed spectra is observed in Figure 5.3.

Figure 5.4 shows the (HAX)PES spectra measured at low (0.2 keV) and high (2.1 keV) excitation energies for the non-rinsed and rinsed samples.
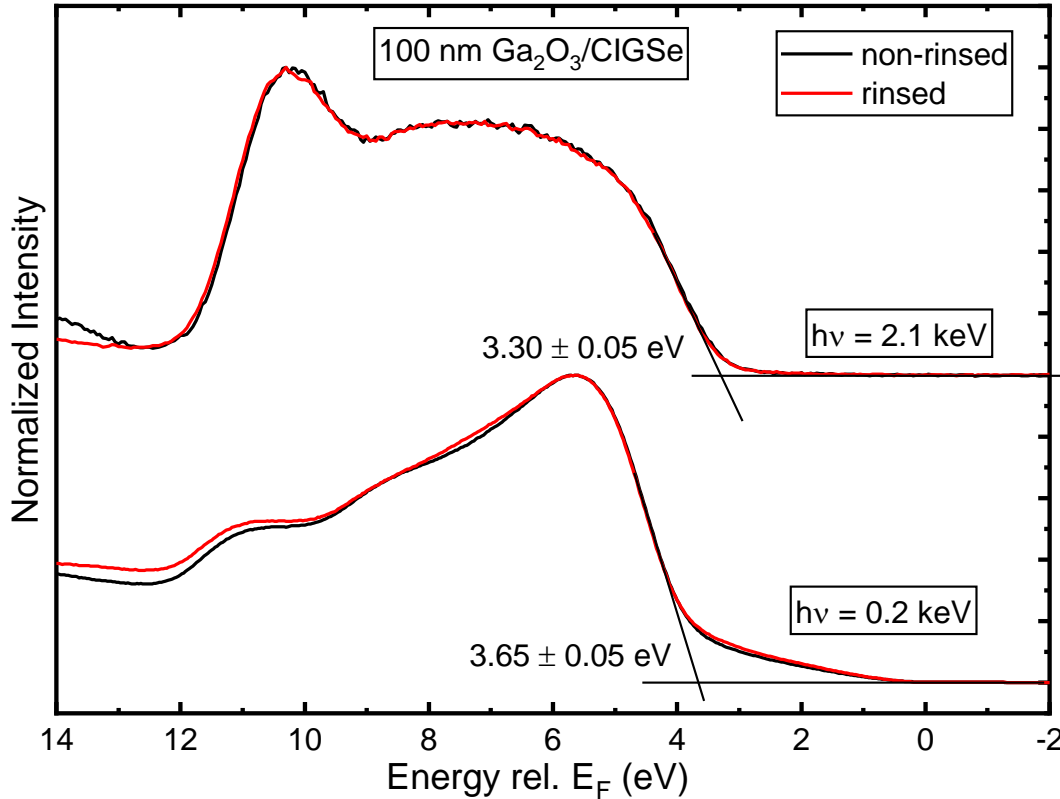
Figure 5.4. Valence bands of the 100 nm non-rinsed (black) and rinsed (red) Ga_2O_3/CIGSe samples measured with PES (photon excitation energy 0.2 keV, bottom) and HAXPES (photon excitation energy 2.1 keV, top). The spectra were normalized to their peak maxima.

One can see that the overall spectral shape is drastically different at low and high excitation energies. There is a large tail between 2 and 4 eV for both of the spectra measured at 0.2 keV, which is much less prominent in the $h\nu = 2.1$ keV spectra. The VBMs were determined by a linear extrapolation of the leading edge, giving the same values for the non-rinsed and rinsed spectra presented here, within the error bar. However, as will be shown in Figure 5.6, there were some differences between rinsed and non-rinsed spectra at some excitation energies. One can also see that the determined VBM value is significantly different for the two excitation energies.

The spectra shown in Figure 5.4 (and in general all the spectra presented in this dissertation) are the averages of a series of scans, from several, up to 100s of scans, depending on various parameters chosen to optimize the measurement). The VBM is determined (by linear extrapolation) for this average, and the error bar is the estimate/confidence interval of the precision with which it can be determined. Looking at the individual scans, one can determine the VBM for each scan (also by linear extrapolation), and the variation of the VBM will show the contribution of the experimental broadening. For the 2.1 keV data, the experimental broadening is only slightly larger than the one given in Figure 5.3 ($\pm$ 0.08 eV vs $\pm$ 0.05 eV). Figure 5.5 shows the individual scans for the 0.2 keV data (for the non-rinsed samples only for clarity of presentation).
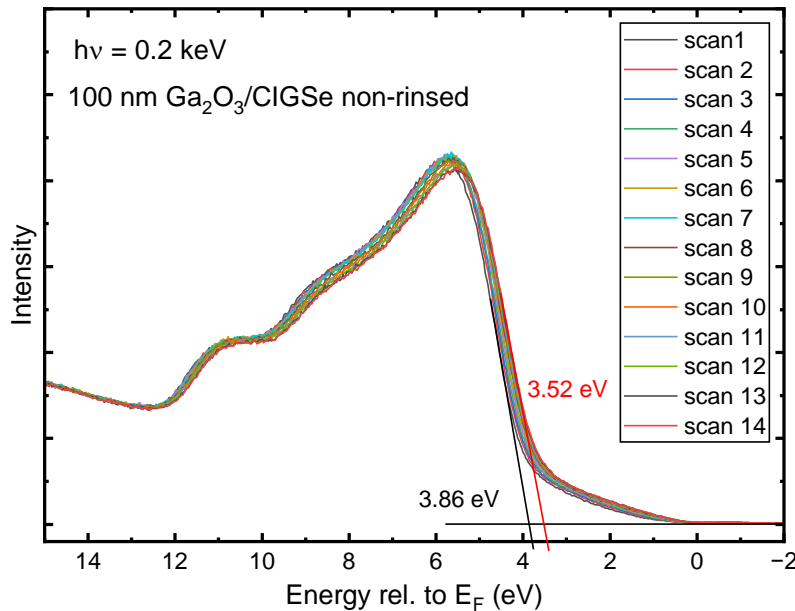
Figure 5.5. Individual scans of the valence band of the 100 nm non-rinsed Ga₂O₃/CIGSe samples, measured with PES at photon excitation energy 0.2 keV.

Figure 5.5 shows that the VBM varies from 3.86 eV for the first scan, up to 3.52 eV for the last scan. Thus, taking into account the experimental broadening, the VBM should be reported as 3.7 $\pm$ 0.2 eV, rather than 3.65 $\pm$ 0.05 eV as presented in Figure 5.4. Although this broadening does contribute to the tail, it does not explain it completely.

Figure 5.6 presents the VBM and corresponding Ga 3d peak positions determined at all the measured excitation energies for both samples.
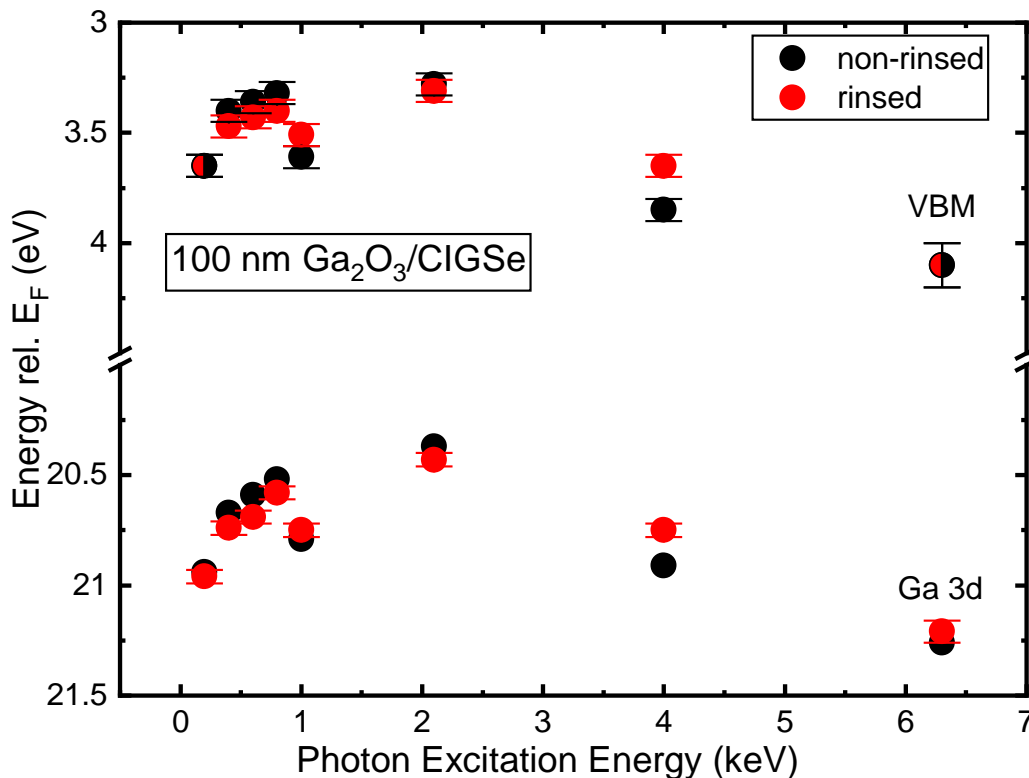
Figure 5.6. Valence band maximum (VBM) and Ga 3d peak position as a function of the excitation energy for the (black) non-rinsed and (red) rinsed 100 nm Ga_2O_3/CIGSe samples. Points where the VBM is equal for rinsed and non-rinsed is are indicated by half-circles of each color.

The VBM was determined by linear extrapolation, while the Ga 3d peak maximum was determined manually, without any additional peak fitting procedure. The error bars are estimates of the confidence with which the VBM and Ga 3d peak positions were determined. Furthermore, the measurements at 6.3 keV have the largest error bars, which is true for both the cleaved and Ar^+-ion treated β-Ga_2O_3 measurements (see 5.4.2 and 5.4.3 below). The energy resolution of the DCM decreases with excitation energy, and to combat this problem, higher harmonics of the DCM are used.[62] However, this significantly reduces the photon flux, resulting in a lower signal-to-noise ratio. In addition, the absolute values of all the photoionization cross-sections decrease with the excitation energy, which also results in a lower signal-to-noise ratio.[62] Thus, the spectra measured at 6.3 keV have a lower signal-to-noise ratio than the other presented spectra, resulting

in the larger uncertainty in the VBM and Ga 3d peak position determination. To combat this problem, a large number of scans (on the order of 100s) were taken for the spectra measured at 6.3 keV, but even the average of all these scans still has a low signal-to-noise ratio. Figure 5.7 shows how noisy the individual scans look for these spectra.
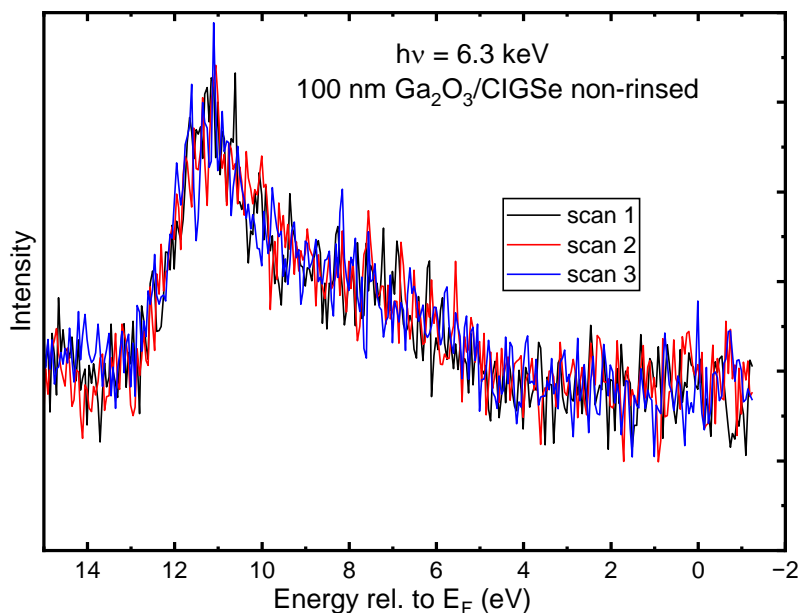
Figure 5.7. Individual scans (first three) of the valence band of the 100 nm non-rinsed Ga_2O_3/CIGSe samples, measured with HAXPES at photon excitation energy 6.3 keV.

Figure 5.6 a) shows that there is a rather wide range in the determined VBM positions: 3.3-3.6 eV for the low excitation energies (i.e., the surface-sensitive measurements), and increasing up to 4.1 eV for the highest excitation energy (i.e., the most bulk-sensitive measurement). Both the VBM position and the Ga 3d peak positions appear to first shift slightly towards, and then shift away from E_F as the measurements become more bulk-sensitive. The similarly in the behavior of the VBM and Ga 3d suggests that this is a systematic shift in the experiments.

These shifts are likely due to band bending at the Ga_2O_3 surface, which can result from surface adsorbates such as O and C. The Fermi level of Ga_2O_3 will shift to align with the Fermi level of the adsorbate molecules. The diffusion of Rb, F, and Na (see Chapter 4) from CIGSe into Ga_2O_3 could also play a role in these shifts. These elements act as dopants, which would change the

position of E_F. It is interesting to note that the VBMs of the rinsed and non-rinsed samples are nearly the same in both Figures 5.6 and 5.8 below. In fact, at several points, the values are identical (shown as half-circles of each color). Although the amounts of these elements are significantly less in the rinsed case, this difference does not appear to play a significant role, as the VBMs are practically identical for the two samples. Surface charging effects could affect the position of E_F as well.

In addition, contaminations and/or defects at the surface, which manifest themselves in the tails shown in the spectra above, could hinder the determination of the true VBM. In the bulk, these effects become minimal, so one can observe the true, slightly higher VBM.

In an attempt to minimize the effects of the changes in the Fermi level position, the Ga 3d peak position of the β-Ga_2O_3 single crystal, measured at an excitation energy for which the calibration was most accurate, corresponding to 21.53 eV was taken as a reference (see section 5.4.2 for more details). Then the difference between the Ga 3d peak positions and this value was added to all the VBMs in Figure 5.4. It is assumed that the resulting VBM positions corrected in this way will be at a more or less constant E_F. Figure 5.8 shows the resulting corrected VBM positions as a function of the excitation energy.
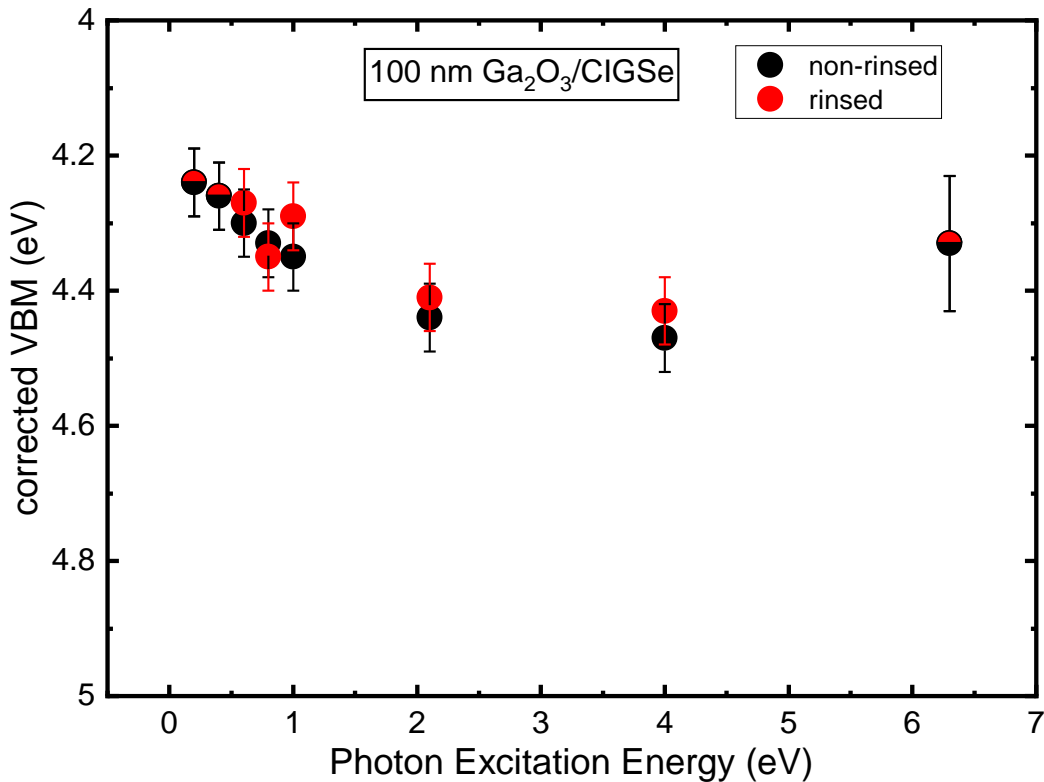
Figure 5.8. Corrected VBM (shifted such that the Ga 3d peak position is constant) as a function of the excitation energy for the (black) non-rinsed and (red) rinsed 100 nm Ga_2O_3/CIGSe samples. Points where the VBM is equal for rinsed and non-rinsed are indicated by half-circles of each color.

Figure 5.8 shows that there is much less of a difference now between the VBMs at different excitation energies. However, the VBM slightly increases from 4.2 eV at low photon excitation energies to 4.4 eV at high photon excitation energies (i.e., the relative VBM value increases from more surface-sensitive to more bulk-sensitive measurements). This suggests that there is a real difference between the surface and bulk of these samples.

To understand better the results obtained for these samples, the valence band of the β-Ga_2O_3 single crystal was investigated as a next step. For the measurements of the 100 nm Ga_2O_3/CIGSe samples, the Au 4f peaks of the Au foil were measured only once in the roughly 24 hour period in between the beam dumps, which could result in an inaccuracy in the determination of the true photon excitation energy. Therefore, for further measurements, the calibration was improved by measuring the Au 4f peaks before and after measurements of the valence band at each excitation energy.

5.4.2 VBM for the UHV-cleaved β-Ga₂O₃ single crystal

From the results in 5.4.1, it is clear that the probing depth plays an important role in the valence band measurements. To further analyze the influence of the condition of the measured surface on the determination of the VBM, a β-Ga₂O₃ single crystal model system was studied. As was explained in 5.2, the β-Ga₂O₃ single crystal was cleaved in UHV prior to the measurements to ensure a clean surface. In parallel, DFT calculations were carried out for the model β-Ga₂O₃ single crystal, obtaining the cross-section dependent PES spectra (see 5.3 for calculation details). Figure 5.9 a) shows the (HAX)PES spectra measured at low (0.2 keV) and high (2.1 keV) excitation energies, while 5.9 b) shows the DFT-calculated PES spectra (total, and projected onto the different orbitals) at the corresponding energies:
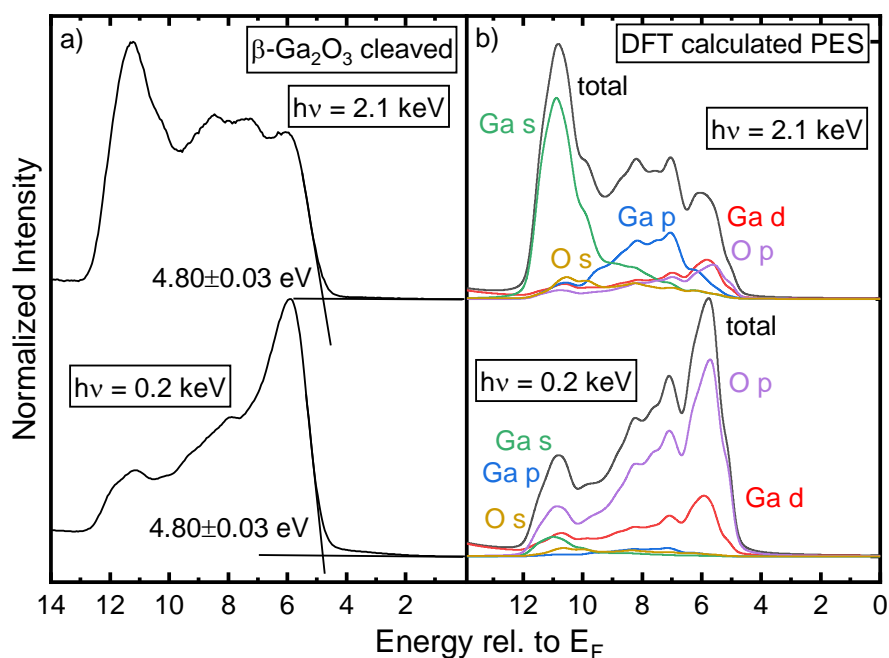
Figure 5.9. a) Valence band of the cleaved β-Ga₂O₃ single crystal measured at 0.2 keV (bottom) and 2.1 keV (top). The VBMs, determined by linear extrapolation of the leading edge, are shown. b) DFT calculated total and projected DOS weighted with the cross-sections to obtain the photoemission spectra (PES) at 0.2 keV (bottom) and 2.1 keV (top). Contributions from different orbitals are color-coded.

Compared with Figure 5.4, the spectra in Figure 5.9 a) are sharper, with more prominent features, while the tail is much smaller, supporting that the tail arises from surface defects and/or adsorbates. The VBM is determined with high accuracy by linear extrapolation of the leading edge as 4.80 ± 0.03 eV, independent of the excitation energy. Although there are some variations in the VBM for measurements at other excitation energies (as will be shown below), the VBM is still determined as 4.8 eV.

Figure 5.9 b) shows how the calculated DOS, weighted by the photoionization cross sections, varies as a function of excitation energy and the symmetry of the orbitals. At 0.2 keV, the O p states are mainly contributing to the total PES, with some contribution from the Ga d states at ~ 6 eV, a small contribution from Ga s states at ~ 11 eV, and practically negligible contributions from the Ga p and O s states (at ~7-8 eV and ~10-11 eV respectively). In contrast, the main contribution to the PES spectrum at 2.1 keV is from the Ga s states, some contribution from the Ga p states, and small contributions from Ga d, O p, and O s states. These results correspond to earlier calculation results in literature.[169] Overall, the DFT-calculations are able to capture the spectral shape of the valence band spectra very well. Figure 5.10 shows a direct comparison between the experimental and calculated valence band spectra at the same two excitation energies as above.
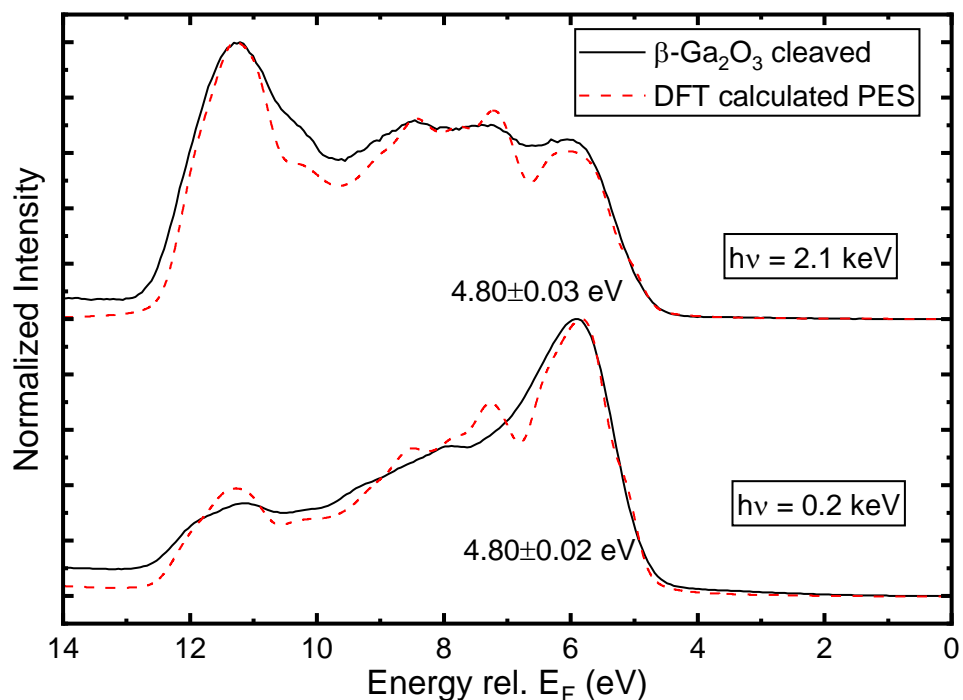
Figure 5.10. Comparison of the cleaved β-Ga$_2$O$_3$ single crystal (black) and DFT calculated PES (red, dashed) at 0.2 keV (bottom) and 2.1 keV (top). The VBMs, determined by linear extrapolation of the leading edge, are shown in black.

In DFT calculations the zero of the energy axis is set at the VBM, so shifts were applied such that the spectral features align with those of the respective experimental valence band. In addition, a stretch factor of 1.08 was applied to both of the calculated spectra for the best alignment of calculation and experiment.

All of the main features observed in the experimental spectra are reproduced in the calculations, and overall, the agreement is excellent between the two. However, many features are more pronounced in the calculations, which could be explained by some additional broadening present in the experiment that is not accounted for. One possibility is surface charging, which leads to small shifts in the peak positions over time, which results in a broadened spectrum. In the 0.2 keV data, there is a small tail that is not described by the calculations. Nonetheless, the spectra are described well, particularly around the VBM, and one can see that when a clean surface is measured, for the 2.1 keV data, the tail is described by experimental and lifetime

broadening. Figure 5.11 shows the VBM and Ga 3d peak positions determined for a wide range of excitation energies.
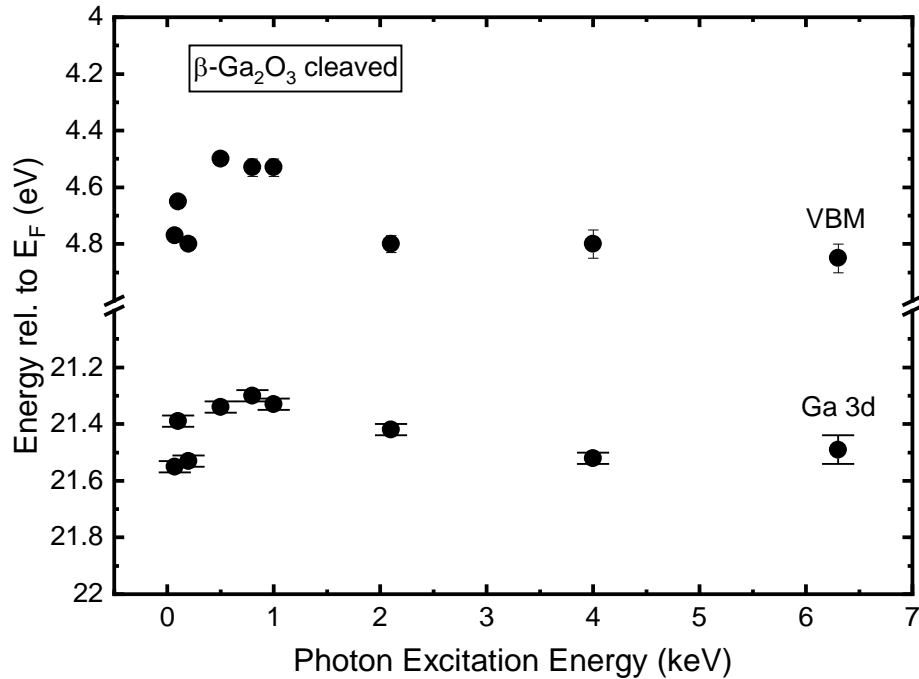
Figure 5.11. VBM and Ga 3d peak positions as a function of the photon excitation energy for the cleaved β-Ga$_2$O$_3$ single crystal.

Compared to the result of Figure 5.6 for the 100 nm Ga$_2$O$_3$/CIGSe samples, there is not much change in the VBM positions with excitation energy in Figure 5.11. However, the VBM and the Ga 3d peak positions both appear to decrease for some photon excitation energies. Here, the Au 4f was always measured before and after each valence band measurement at each excitation energy. As was done in 5.4.1, to minimize the effects of the shift of E$_F$, and obtain the corrected VBM positions, a reference Ga 3d peak position was determined. The measurement at 0.2 keV gave the most stable result, with no change in the Au 4f peak position before and after the valence band measurement. Thus, the corresponding Ga 3d peak position (21.53 eV) was chosen as the reference. The difference between the Ga 3d peak positions at each excitation energy and this value was added to the VBM, to obtain the corrected VBM values. Figure 5.12 shows the corrected VBM as a function of the excitation energy.
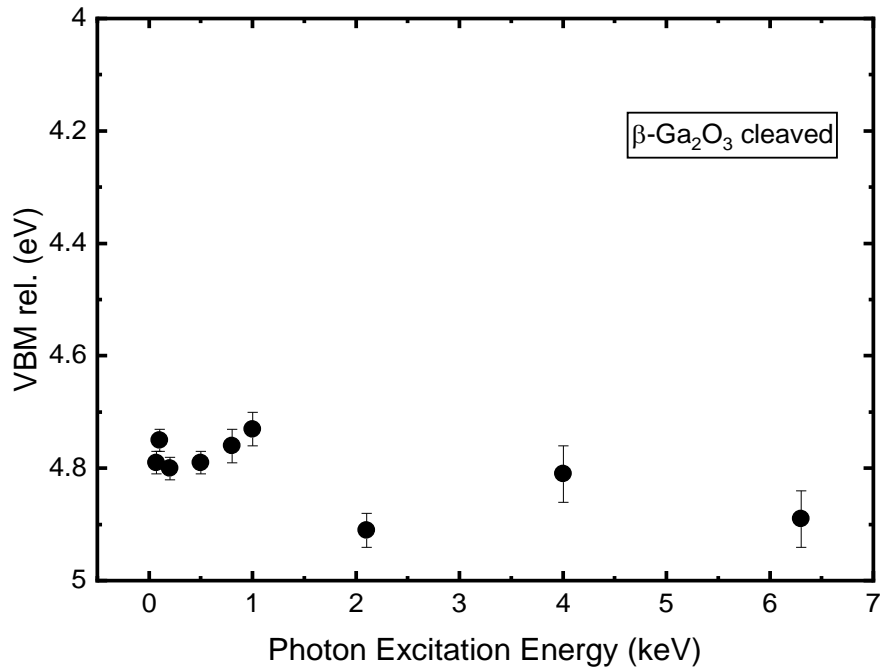
Figure 5.12. Corrected VBM (shifted such that the Ga 3d peak position is constant) as a function of the excitation energy for the cleaved β-Ga$_2$O$_3$ single crystal.

From Figure 5.12, the VBM for the cleaved β-Ga$_2$O$_3$ single crystal can be determined as 4.8 ± 0.1 eV. There is still a small downwards shift in the VBM with excitation energy, but one would need to perform more HAXPES measurements at other excitation energies to confirm this shift. The VBM is 0.5 eV higher than the one determined for the 100 nm Ga$_2$O$_3$/CIGSe samples. The surface defects that especially appear in the tails of the 100 nm Ga$_2$O$_3$/CIGSe samples, the diffusion/segregation of Rb, F, and Na from the CIGSe to the Ga$_2$O$_3$ surface, and the fact that these are different samples (a nanocrystalline thin film vs a single crystal), and underwent different sample preparation can all play a role in the observed differences in the valence band and VBM. However, (as mentioned in 5.4.1) the rinsing does not seem to affect the VBM position. In any case, the state of the surface appears to significantly affect the VBM value. To model a defect-rich Ga$_2$O$_3$ surface, the results for the Ar$^+$-ion treated β-Ga$_2$O$_3$ single crystal are investigated next.

5.4.3 VBM for the Ar⁺-ion treated β-Ga₂O₃ single crystal

Figure 5.13 shows the valence band of the Ar$^+$-ion treated β-Ga$_2$O$_3$ single crystal, together with the cleaved β-Ga$_2$O$_3$, and the 100 nm Ga$_2$O$_3$/CIGSe (rinsed) sample at selected photon excitation energies.
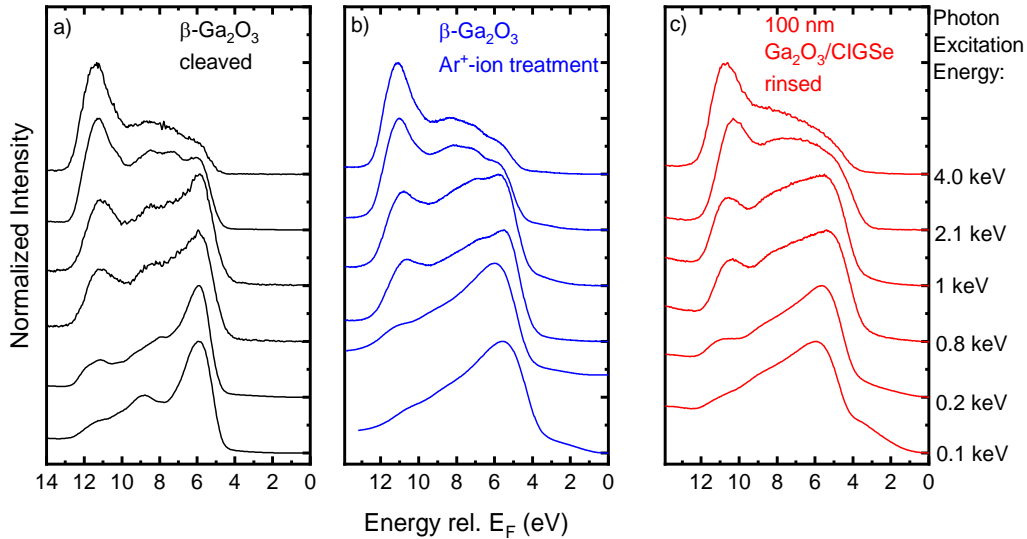
Figure 5.13. Valence bands of the a) cleaved β-Ga$_2$O$_3$ single crystal (black), b) β-Ga$_2$O$_3$ single crystal after Ar$^+$-ion treatment (blue), and c)100 nm rinsed Ga$_2$O$_3$/CIGSe samples (red) measured with HAXPES at a wide range of photon excitation energies. The spectra were normalized to their peak maxima.

The spectra of the Ar$^+$-ion treated β-Ga$_2$O$_3$ single crystal can be viewed as an intermediate "step" between the cleaved β-Ga$_2$O$_3$ single crystal and the 100 nm Ga$_2$O$_3$/CIGSe sample. The overall spectral shape is closer to that of the 100 nm Ga$_2$O$_3$/CIGSe, while some spectral features are present in the cleaved β-Ga$_2$O$_3$ single crystal but absent in the 100 nm Ga$_2$O$_3$/CIGSe are present in the Ar$^+$-ion treated β-Ga$_2$O$_3$ single crystal, but in a more broadened form. For example, the Ga p contribution at ~7-8 eV (see Figure 5.9), is broader but visible in the spectra at 2.1 keV, while it cannot be distinguished in the corresponding spectrum of the 100 nm Ga$_2$O$_3$/CIGSe sample. There is a tail at 2-4 eV, especially prominent at lower excitation energies, but it is not as large as in the spectra of the 100 nm Ga$_2$O$_3$/CIGSe sample. The presence of the tail suggests that defects such as O vacancies are indeed introduced to the surface as a result of the Ar$^+$-ion treatment.

Figure 5.14 shows the region near the VBM for all three samples at 0.1 and 4.0 keV.
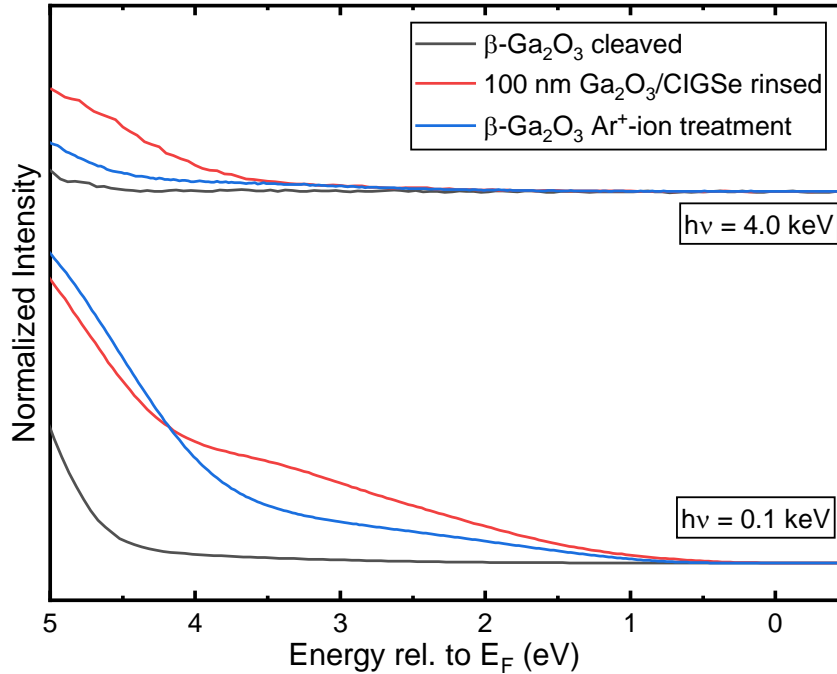
Figure 5.14. Comparison of the region near the VBM for the (black) cleaved β-Ga$_2$O$_3$ single crystal, (red) 100 nm Ga$_2$O$_3$/CIGSe rinsed sample, and the (blue) Ar$^+$-ion treated β-Ga$_2$O$_3$ single crystal, measured with 0.1 keV (bottom) and 4.0 keV (top).

One can see that at low excitation energies, the tail is the largest in the 100 nm Ga$_2$O$_3$/CIGSe spectra, followed by the Ar$^+$-ion treated β-Ga$_2$O$_3$ single crystal (there is no visible tail for the cleaved β-Ga$_2$O$_3$). At high excitation energies, there is some difference in the spectral intensities of the three samples at above 4 eV (the 100 nm Ga$_2$O$_3$/CIGSe spectra has a higher intensity between 4 and 5 eV than the other two spectra), but this does not contribute to the tail. Thus, Figure 5.14 shows that the tail plays a large role at low excitation energies (i.e., for surface-sensitive measurements), but not at high excitation energies (the bulk-sensitive measurements), as expected.

Figure 5.15 shows the VBM and Ga 3d peak positions as a function of the photon excitation energy for the Ar$^+$-ion treated β-Ga$_2$O$_3$ single crystal.
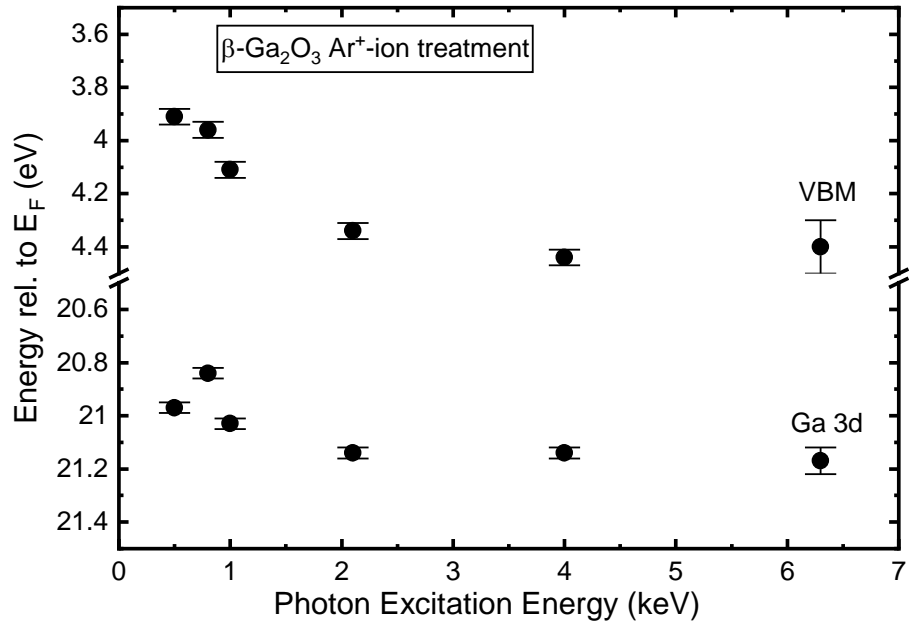
Figure 5.15. VBM Ga 3d peak positions as a function of the photon excitation energy for the Ar⁺-ion treated β-Ga$_2$O$_3$ single crystal.

Once again, a downwards shift away from E$_F$ with the photon excitation energy can be observed in both the VBM and Ga 3d positions. The same shift to the VBM positions was applied as described earlier, and the resulting corrected VBM positions are shown in Figure 5.16.
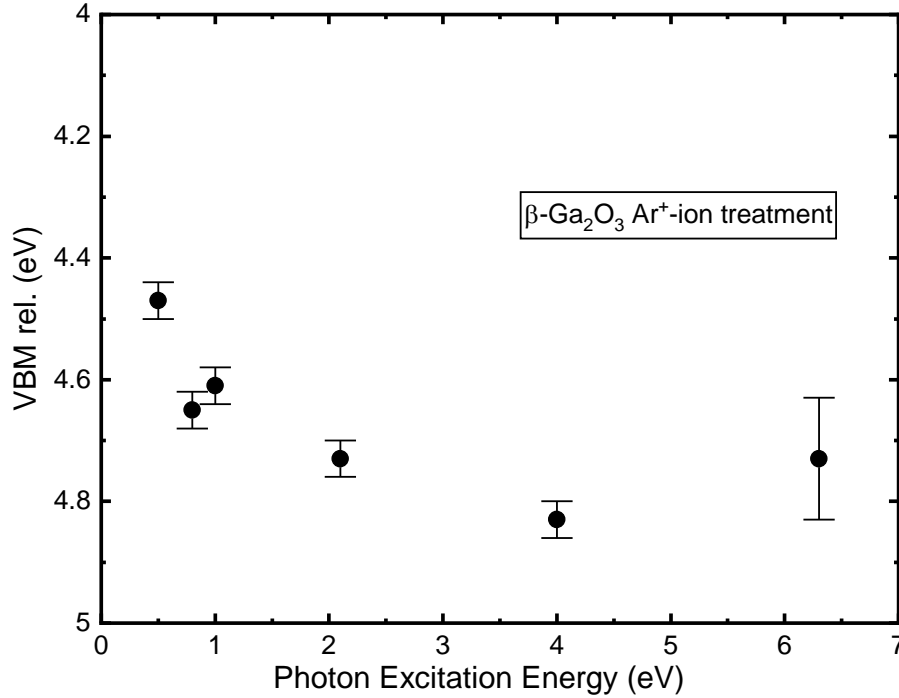
Figure 5.16. Corrected VBM (shifted such that the Ga 3d peak position is constant) as a function of the excitation energy for the Ar⁺-ion treated β-Ga$_2$O$_3$ single crystal.

The corrected VBM clearly increases with photon excitation energy until it reaches a plateau at the highest excitation energies. Similar to Figure 5.8, it can be concluded that the tail present at lower excitation energies (i.e., in more surface-sensitive measurements) affects the VBM position, and the VBM of the surface and bulk are different. This is true for the Ar⁺-ion treated crystal, as well as the 100 nm Ga$_2$O$_3$/CIGSe samples. From the results above, one can conclude that "cleaning" the β-Ga$_2$O$_3$ single crystal surface with Ar⁺-ions is on the right path towards describing the valence band of the 100 nm Ga$_2$O$_3$/CIGSe samples.

5.5　Conclusion

In this Chapter, valence band spectra were presented for the 100 nm Ga_2O_3/CIGSe samples, and the UHV-cleaved and Ar^+-ion treated β-Ga_2O_3 single crystals. Complimentary DFT calculations were performed for β-Ga_2O_3 as well.

For the 100 nm Ga_2O_3/CIGSe samples, the VBM was found to significantly change depending on the excitation energy, suggesting that the VBM of the surface differs from that of the bulk. The VBM appeared to shift away from the Fermi energy with excitation energy. This can likely be explained by band bending at the Ga_2O_3 surface, due to surface adsorbates such as O and C.

The VBM for the cleaved β-Ga_2O_3 was determined as 4.8 ± 0.1 eV, independent of the excitation energy, and corresponds to results in literature. The band-bending effects observed for the 100 nm Ga_2O_3/CIGSe samples, were absent (or very minimal) for the cleaved β-Ga_2O_3 sample. Various effects, such as the morphology (nanocrystalline vs single crystalline), surface defects, and the diffusion/segregation of small amounts of Rb, F, and Na from the CIGSe absorber, all could play a role in the significantly lower value of the VBM of the 100 nm Ga_2O_3/CIGSe samples compared to the cleaved β-Ga_2O_3. However, the rinsing did not appear to affect the VBM position. The overall spectral shape was found to be much broader in the nanocrystalline sample, which could also potentially be explained by the effects above.

The Ar^+-ion treated β-Ga_2O_3 single crystal was found to be an intermediate "step" between the nanocrystalline and cleaved β-Ga_2O_3 single crystal, in its spectral shape, as well in the behavior of the VBM, i.e., its shift away from the Fermi energy with photon excitation energy. It is likely that the Ar^+-ion treatment introduces defects such as O vacancies to the β-Ga_2O_3 surface. The Ar^+-ion treatment could potentially be used as a way to model the VBM of nanocrystalline Ga_2O_3 as well.

6 Resonant inelastic x-ray scattering of Ga$_2$O$_3$

6.1 Introduction

In Chapter 2, the crystal structure of β-Ga$_2$O$_3$ was presented. It is not surprising that the anisotropy in the crystal structure of β-Ga$_2$O$_3$ leads to an anisotropy in its electrical and optical properties. Several studies have shown an anisotropy in the optical absorption, resulting in different bandgap edges depending on the polarization of the light source[18,31–33]. Such studies allow to understand transitions from the valence to the conduction band, but cannot paint a comprehensive picture of the electronic structure, and contain no information on the core-levels. Several Angle-Resolved Photoemission Spectroscopy (ARPES) studies have been performed to determine the band structure along specific high-symmetry points and a good correspondence with DFT calculations was obtained.[175–178] However, these works did not focus on the polarization-dependent results due to the anisotropy of β-Ga$_2$O$_3$.

Cocchi et al. investigated the core-level excitations from the O K edge of β-Ga$_2$O$_3$[129]. They calculated the XAS spectra in the BSE approach for different inequivalent oxygen atoms and compared them with experimental energy-loss near-edge fine structure (ELNES) spectra along different crystal planes, finding that contributions to the spectra from certain types of atoms can be enhanced, while others can be suppressed. Swallow et al. investigated different polymorphs of Ga$_2$O$_3$[57] and found that the XAS spectra vary significantly depending on the polymorph and its crystal structure. Vorwerk studied extensively the theoretical RIXS spectra of Ga$_2$O$_3$[179,180], and one of the focuses was to understand how the absorption spectra differ between the polymorphs. Up to date, no experimental RIXS studies of Ga$_2$O$_3$ have been published.

In this chapter, the bulk electronic structure of β-Ga$_2$O$_3$ is studied by measuring experimental XAS, XES, and RIXS spectra at the O K edge, and comparing them with those calculated using the DFT/BSE methods. The XAS, XES, and RIXS spectral intensities are proportional to the dipole transition matrix elements (see equations 2.10-2.12 in Chapter 2). The dipole transition matrix elements depend on the polarization of the incoming photon beam, so by controlling the orientation of the β-Ga$_2$O$_3$ single crystal with respect to the polarization of the incoming x-ray

beam, excitations from various parts of the band structure can be enhanced or suppressed. Moreover, the dipole transition matrix elements also depend on the local geometry of the O atoms. Since there are three inequivalent O atoms in β-Ga_2O_3 (see Chapter 2), these atoms can contribute differently to the spectra depending on the polarization of the x-ray beam. As will be shown below, there are clear differences in the spectra depending on the polarization, which are observed in both the measured and calculated spectra.

6.2 Experimental details

All of the experiments discussed in this chapter were performed at the SALSA endstation[136] at Beamline 8.0.1 of the Advanced Light Source (ALS), Lawrence Berkley National Laboratory. (for more details on SALSA and the x-ray spectrometer, see Chapter 3 and Refs[136,137]). Measurements were performed on β-Ga_2O_3 single crystal samples: in addition to crystals with the (010) orientation described in Chapter 5, a crystal with the (001) orientation was ordered from the same company (Novel Crystal Technology, Inc., Tamura Corporation), and measured as well.

To perform polarization-dependent measurements, the samples were rotated such that the respective unit cell vector would align with the polarization vector of the incident photon beam. As shown in Figure 6.1 below, the incident photon beam is oriented normal to the sample surface, and the optical axis of the spectrometer is oriented at 45° relative to the incident photon beam.[181]
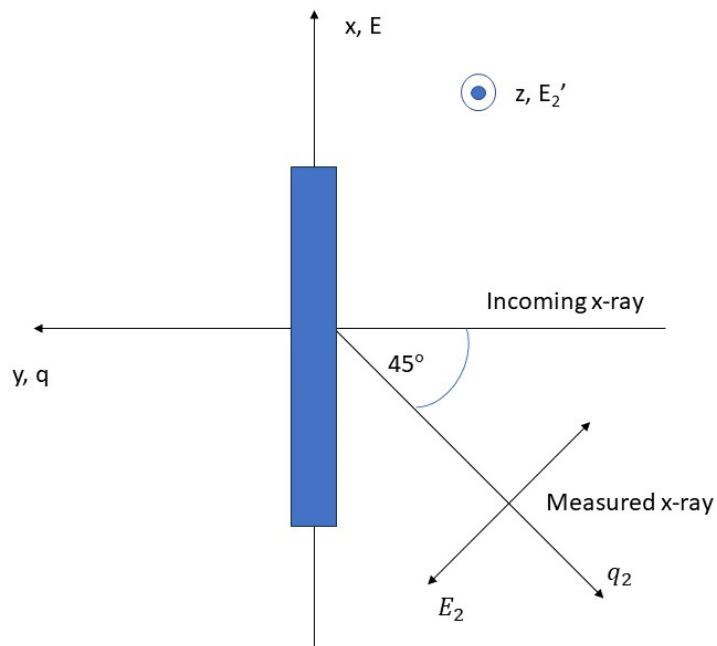
Figure 6.1. View in the x-y plane of the experimental setup of the sample relative to the incident synchrotron-based x-ray source for all three polarization directions.

Here, q and $\mathbf{E}$ are the momentum and polarization of the incoming x-ray photon. The momentum for the measured x-ray photon is q_2, while $\mathbf{E_2}$, and $\mathbf{E_2'}$ are the basis orthonormal vectors in the plane perpendicular to q_2, i.e., the plane to which all outgoing polarizations belong to. So $\mathbf{E_2}$, and $\mathbf{E_2'}$ are sufficient for calculations, since all other polarization directions are their linear combinations.

Figure 6.2 shows the experimental setup when $\mathbf{E}$ is parallel to a.

(010) Single crystal
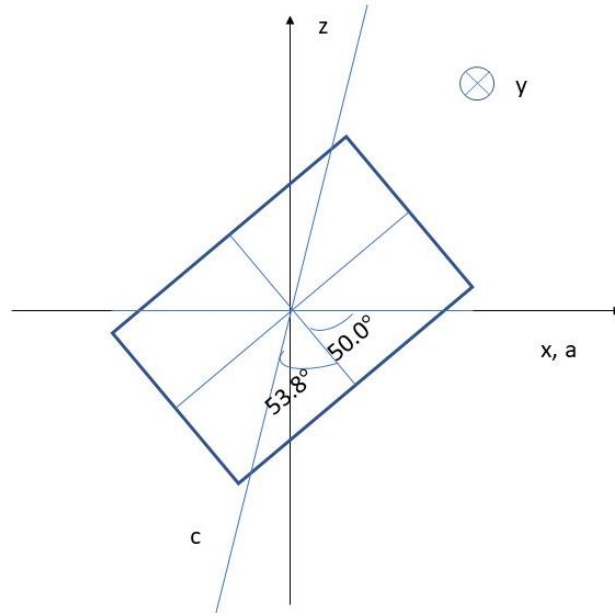
Figure 6.2. View in the x-z plane of the experimental setup when the polarization of the incoming photon beam, **E** is parallel to **a**. To perform measurements where **E** is parallel to **c**, the sample is rotated by 103.8° in the counterclockwise direction, such that the c axis aligns with the x axis.

Figure 6.2 shows that the (010) single crystal is rotated such that the **a** axis is aligned with the x axis and hence with **E**. The sample is then rotated by 103.8° in the counterclockwise direction to performed measurements where **E** is parallel to **c**.

Figure 6.3 shows the experimental setup when **E** is parallel to **b**.
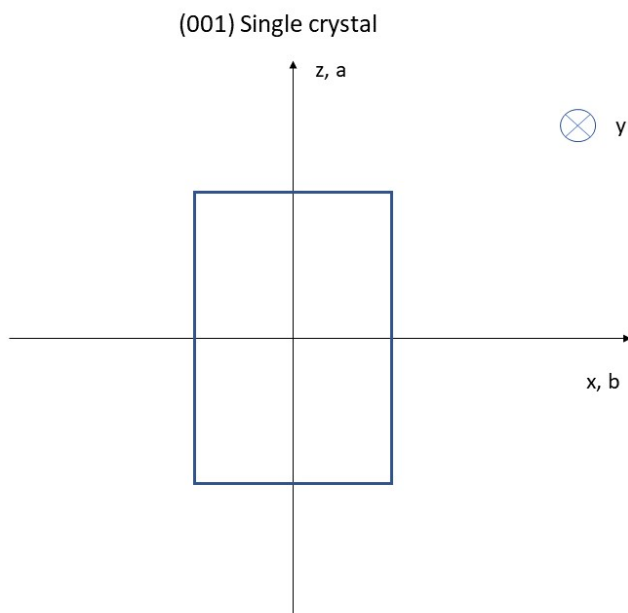
Figure 6.3 View in the x-y plane of the experimental setup when the polarization of the incoming photon beam, **E** is parallel to **b**.

The (001) single crystal, with its shorter side parallel to **b**, is necessary to be able to measure this configuration.

For each configuration, RIXS maps and non-resonant XES spectra were obtained. The emission energy scales were calibrated using the emission energies of carefully measured BN and $CaSO_4$ reference samples (measured by our group). The excitation energies were then calibrated using the elastically-scattered Rayleigh line.

6.3 Calculations details

In XES, the final state is characterized by a hole in the VB, while all core levels are filled. Thus, according to the final-state rule[102–104], effects such as core-exciton formation will not play a crucial rule (the hole in the VB is assumed to be well-screened), and ground-state calculations are often sufficient to describe XES spectra. Therefore, in the following, the experimental XES spectra are compared with spectra calculated from ground state DFT.

The electronic structure and polarization-independent XES spectrum of β-Ga$_2$O$_3$ were calculated using Wien2k. As in Chapter 5, the GGA with the PBE parametrization was used to approximate the exchange-correlation functional. The product of the smallest muffin tin radius R$_{MT}$ times the largest k-vector K$_{max}$, was set equal to 8. The self-consistent field (SCF) cycle was run with 1000 k points, while the projected density of state (PDOS) and XES calculations were run with 10000 k points. The XES spectra are calculated according to the formalism in Refs.[49, 50]. Taking into account the dipole-selection rules, the dipole matrix elements are generated, and then multiplied by the corresponding PDOS and radial transition probability to obtain the spectra.[184]

The polarization-dependent XES calculations were performed with the OCEAN code, where the ground-state wave functions are calculated with the pseudopotential-based code Quantum Espresso[185] (see chapter 2). It is necessary to specify the photon operator, as well as the momentum and polarization of the incoming (q and $\mathbf{E}$) and outgoing (q_2, $\mathbf{E_2}$, and $\mathbf{E_2}$') x-ray photons, which is done through the 'photon files' in OCEAN. The photon operator is approximated as $\mathbf{E} \cdot r$ (the dipole approximation operates well for light atoms such as O with small core wave-functions, i.e., small r, and small photon energies, i.e., small q [81]). The momentums and polarizations(q, $\mathbf{E}$, q_2, $\mathbf{E_2}$, and $\mathbf{E_2}$') were specified according to the experimental setups shown in Figures 6.1-6.3, thereby generating 9 photon files (3 for each experimental configuration). The momentum transferred to the system in units of the reciprocal lattice vectors was also specified (this is necessary for the RIXS calculations) in the main input file (as 'photon_q').

The basis set for the ground-state wavefunctions in Quantum Espresso is constructed using the norm-conserving pseudopotential, and the plane-wave cut-off was set to 122 Ryd. As in Wien2k, the GGA with the PBE parameterization was used. The energy difference between the CBM and

the highest calculated band for the final state wave functions was set to approximately 40 eV, after a series of XAS calculations with a different number of bands, and comparison of the results with the corresponding energy interval in the experimental data. A series of convergence tests were performed to determine the optimal k-point and x-point grids for calculation of the final states, which were taken as 8x8x5 and 14x14x12, respectively. A 4x4x3 k-point grid was sufficient to take for the SCF cycle.

As mentioned in Chapter 2, the ground-state DFT energies are not necessarily accurate in terms of both their absolute position, and their relative shifts (core-level shifts). This is true both for the LAPW + lo based Wien2k, since final state screening-effects are not included,[170] and for pseudopotential-based Quantum Espresso where there are no explicit core states.[81] In OCEAN, the core-level shifts are treated in the screening part of the calculation, where a single offset number is set, in accordance with the ground-state and screening calculations. The number of conduction bands was set to approximately span 150 eV above the conduction band minimum for the screening calculations.

In XAS, the final state is a core hole and an electron in the CB, so it is necessary to describe the bound excitonic state formed by the electron with the core hole. As was described in Chapter 2, RIXS is treated in the Kramers-Heisenberg formalism as a coherent process, and the resonant XES spectra are influenced both by the core-exciton formed in the intermediate state, and the valence-exciton formed in the final state. The Bethe-Salpeter Equation (BSE) is solved in a two-particle electron-hole basis using the ground state wave functions obtained using DFT, with the BSE Hamiltonian given in Chapter 2. The generalized minimal residual method (GMRES)[186,187] is used to diagonalize the BSE Hamiltonian.

A small amount of Lorentzian broadening (0.1 eV) for the core-hole lifetime is included in the spectra, to which Gaussian and Lorentzian broadening was further applied when comparing the calculations with experiment (see next section). Stretch factors of 5% to the excitation energy axis of the XAS spectra, and 10% to the emission energy axis of the XES spectra calculated using OCEAN were applied as well, in accordance with the above-mentioned underestimation of band-gaps and core-level positions in DFT. Crystallographic Information Files (CIF) containing the crystal structure were obtained from the Materials Project[174] and Crystallography Open Databases[188], and give the same results.

6.4 Results and discussion

6.4.1 Non-resonant XES spectra

Figure 6.4 shows a comparison of the experimental O K XES spectrum of β-Ga$_2$O$_3$ with the DFT-calculated electronic band structure and XES spectrum (all calculations were performed here using Wien2k).
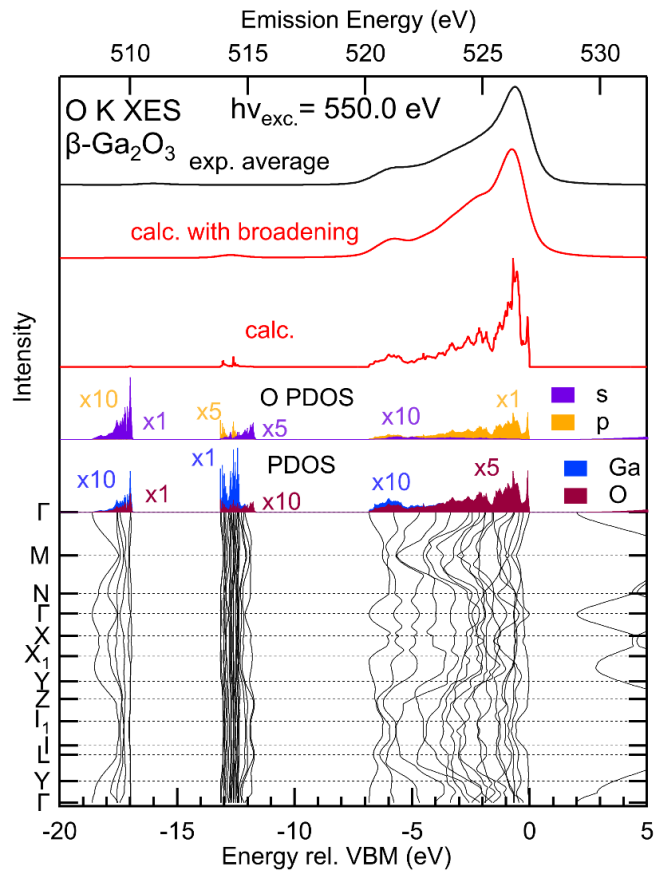
Figure 6.4. Comparison of the experimental O K XES spectrum with the DFT-calculated electronic band structure and spectrum for β-Ga$_2$O$_3$. From bottom to top: calculated k-resolved band structure, projected density of states (PDOS) for the gallium (blue) and oxygen (black) atoms, oxygen s (purple) and p (orange) PDOS, calculated O K emission spectrum (red, "calc."), calculated XES spectrum with experimental and lifetime broadening (red, "calc. with broadening"), and the experimental XES spectrum

measured at an excitation energy 550.0 eV (black, top). The zero of the energy scale of the calculations is set at the valence band maximum (VBM). Wien2k was used for the calculations.

At the bottom of the Figure, the calculated k-resolved band structure is shown, as was seen already in Chapter 2 (Figure 2.14), but here the energy and k-axes are reversed. As was discussed in Chapter 2, the band structure can be divided into three regions: the upper valence band region at 0 to 7 eV below the VBM, and the Ga 3d and O 2s semi-core regions at $\sim$ 12 eV to 13 eV and $\sim$ 17 eV to 20 eV below the VBM, respectively. The density of states projected (PDOS) onto the oxygen and gallium atoms, and then onto the oxygen s and p orbitals, is shown above the band structure. One can see that the upper valence band region is mostly composed of oxygen p orbitals. Moreover, while the Ga 3d semi-core region mostly consists of Ga, there are small contributions from O 2s and O 2p states there as well. In fact, there is Ga 3d – O 2s [57], as well as Ga 3d – O 2p hybridization (similarly to that observed for other metal oxides[189]) and there is a small contribution from Ga 3d in the O 2s semi-core region as well (note the x10 factor for the Ga PDOS in this region).

The calculated O K XES spectrum is shown on top of the PDOS. There is the main peak (maximum at $\sim$ -1.5 eV rel. to the VBM or $\sim$ 526 eV emission energy) which is the O 2p derived band due to transitions from O 2p to O 1s. There are also two very small peaks near the position of the Ga 3d semi-core region, due to transitions from the Ga 3d – O 2p hybridized-state to O 1s, referred to as the Ga 3d – O 2p hybrid band. Above this is the same spectrum convoluted with experimental and lifetime broadening (0.5 eV Gaussian and 0.1 eV Lorentzian broadening applied). Comparing it with the experimentally obtained spectrum on the top (measured at an excitation energy of 550.0 eV), there is a good correspondence, with all the main features correctly reproduced in the calculated spectrum. In both spectra, a very small contribution from the Ga 3d – O 2p hybrid band can be seen. Only one peak is seen in the experiment, the position of which differs by almost 5 eV compared to the calculated spectra. This is in line with the previously mentioned limitations of DFT in determining the absolute peak positions accurately.

Since the polarization is not a relevant parameter for the XES spectra calculated using Wien2k (as it was calculated from the PDOS), the experimental spectrum shown is an average over the 3 orientations of the incoming x-ray beam ($\mathbf{E} \parallel \boldsymbol{a}$, $\mathbf{E} \parallel \boldsymbol{b}$, and $\mathbf{E} \parallel \boldsymbol{c}$). Figure 6.5 shows a

comparison of the calculated (with experimental and lifetime broadening) and experimental emission spectra for all 3 polarization directions separately calculated with OCEAN.
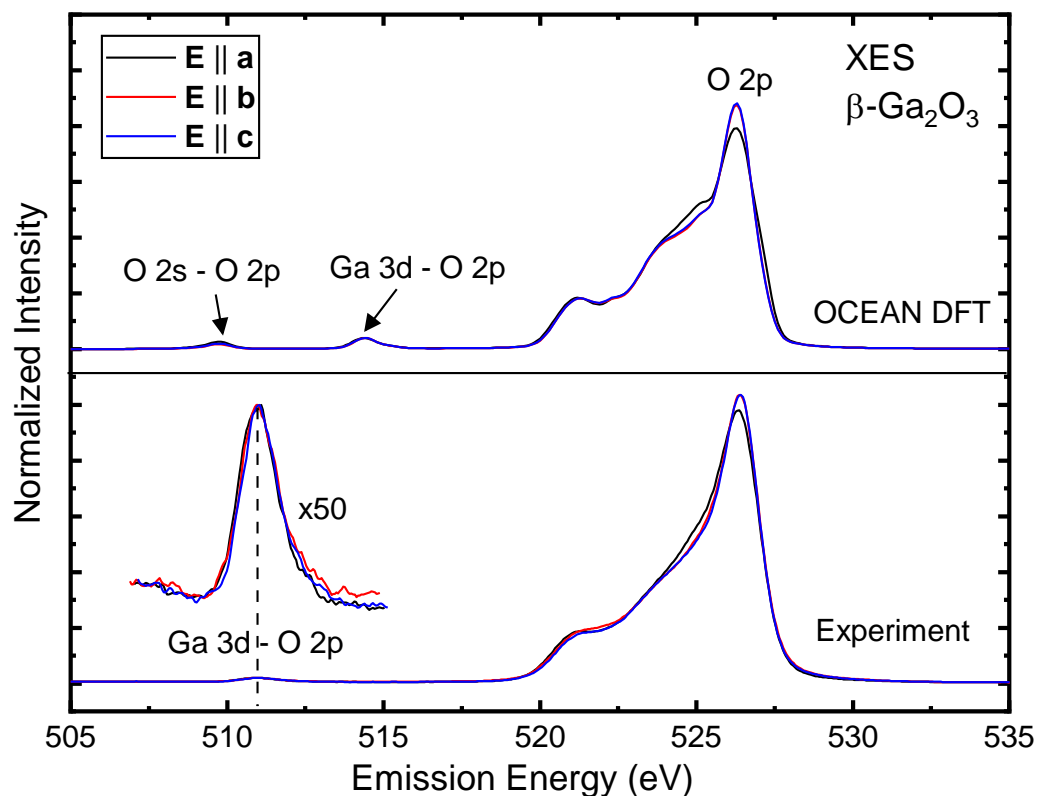
Figure 6.5. Comparison of the experimental O K emission spectra measured at excitation energy 550.0 eV (bottom) with the DFT-calculated emission spectra with experimental and lifetime broadening (top) for the 3 polarization directions: E ∥ *a* (black), E ∥ *b* (red), and **E ∥ *c*** (blue). The emission spectra were calculated on an arbitrary emission scale, and were aligned with the energy scale of the experimental spectra such that the O 2p derived band maxima (~526 eV) align with each other. The intensities were normalized to the maxima of the Ga 3d – O 2p hybrid band (~515 eV) in the experiment and calculation. A magnified (x50) Ga 3d – O 2p hybrid band region for the experimental spectra is shown. The O 2s – O 2p hybrid band (~510 eV) is visible in the calculations, but not in the experiment. OCEAN was used for the calculations.

The emission spectra were calculated on an arbitrary emission scale, and were aligned with the energy scale of the experimental spectra such that the O 2p derived band maxima (~526 eV) align with each other. To observe differences in the O 2p derived band, the spectra were then

normalized to the maxima of the Ga 3d – O 2p hybrid band (~515 eV) in both experiment and calculations, since this feature is unlikely to exhibit any changes depending on the polarization direction (being further away from the upper valence band it is more robust to changes in general). In the calculated spectra, there is the O 2s – O 2p hybrid band at ~510 eV, while it is not visible in the experimental spectra. This is because O K emission only allows to see the O 2p contribution, which is very weak at 510 eV (see Figure 6.4). So while it is predicted in theory, it is not observed in the experimental spectra.

Overall, the spectra for the 3 polarization directions are very similar both in experiment and in calculations. However, the spectrum for the **E ∥ a** direction has a slightly smaller relative intensity of the main peak at 526 eV, but exhibits a more intense shoulder at lower energies (at ~ 525 eV). Furthermore, the calculations accurately reproduce this difference in the **E∥ a** spectrum. As explained earlier, the spectral intensities are weighted by the dipole transition matrix elements, which depend on the polarization of the incident photon, as well as on the position of the electron, i.e., which inequivalent O atom it comes from. Figure 6.6 shows the XES spectra calculated for differently coordinated oxygen atoms (i.e., O1, O2 and O3 shown in Figures 2.11 and 2.12) for the 3 polarization directions.
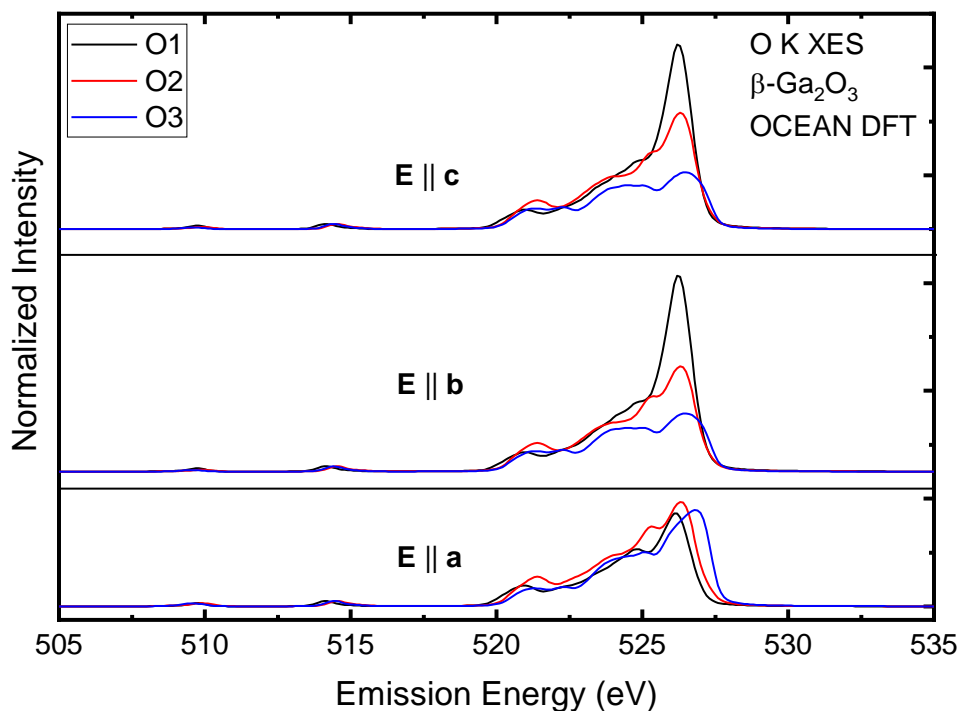
Figure 6.6. DFT-calculated contributions from differently coordinated O atoms, i.e., O1 (black), O2 (red) and O3 (blue), to the emission spectra for the 3 polarization directions: **E ∥ a** (bottom), **E ∥ b** (middle), and **E ∥ c** (top). The emission spectra were calculated on an arbitrary emission scale, and were aligned and broadened as in Figure 6.8. The intensities were normalized to the maxima of the Ga 3d-O 2p hybridized state at ~514 eV. OCEAN was used for the calculations.

One can see that when **E ∥ b** and **E ∥ c**, the results are nearly identical, and the largest contribution is from O1. When **E ∥ a**, there are equal contributions between O1, O2, and O3. The contribution from the tetrahedrally-coordinated O3 is much stronger in the emission spectrum where **E ∥ a** than for the other two directions. It is shifted towards higher emission energy relative to O1 and O2, explaining the difference in the observed experimental spectrum for the **E ∥ a** direction. Nonetheless, the difference in the emission spectra for the different polarization directions is not as significant as in the absorption spectra that will be shown below.

6.4.2 RIXS maps

To understand better the differences in the polarization directions, the RIXS experiments are analyzed as a next step. Core-excitonic effects appear in both experimental and calculated XAS and RIXS spectra, as seen below.

Figure 6.7 shows the experimental RIXS maps obtained for the 3 polarization directions:
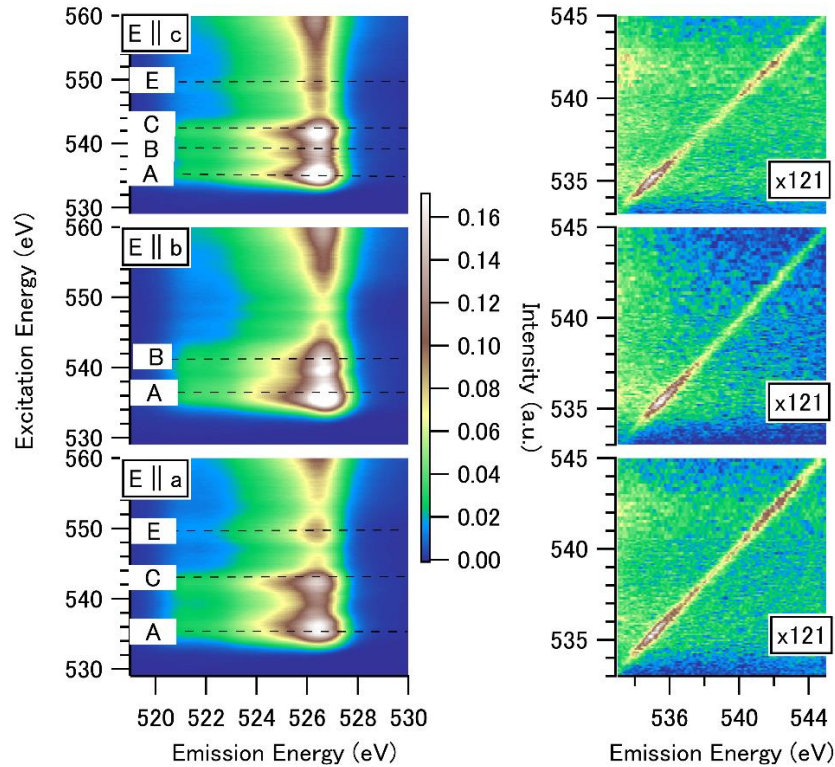
Figure 6.7. Experimental O K RIXS maps of β-Ga$_2$O$_3$ for the 3 polarization directions: **E ∥ a** (bottom), **E∥ b** (middle), and **E ∥ c** (top). The emission intensity is color-coded according to the colorscale shown and displayed as a function of the excitation and emission energies. For each polarization direction, the RIXS maps are divided into the spectator (left) and participant (right) regions. Selected absorption resonances are labeled on the left of the spectator regions and will be discussed in conjunction with Figure 6.12. The participant emission intensities are magnified by a factor of x121.

In the maps, the emission intensity is color-coded and displayed as a function of the excitation and emission energies. For each polarization direction, the RIXS maps are divided into spectator and participant regions. Figure 6.7 shows that there are distinct differences in the RIXS maps for the 3 polarization directions in the spectator region. While there are only small differences in the main emission feature from the O 2p derived band there are different absorption resonances (labeled as A, B, C, and E on the maps), that are clearly more pronounced in some maps and less in others. This will be discussed in more detail in conjunction with Figure 6.9.

For all 3 polarization directions, in the participant regions, there is the elastically scattered Rayleigh line, which is weak compared to the spectator emission (hence the magnification factor

99

of x121). Furthermore, in all 3 cases, an enhanced intensity (resonance) in the Rayleigh line at the first absorption resonance, i.e., at ~535 eV, labeled as A in the spectator region, and a resonance at ~ 542 eV, labeled C for the **E ‖ *a*** and **E ‖ *c*** directions is observed. These resonances are due to the presence of core-excitonic intermediate states.[63] Thus, there is also a high probability for relaxation, i.e., the recombination of the electron in the conduction band and the core hole, which results in a high emission probability for elastic scattering. Such resonances of the Rayleigh line have been reported by our group previously[190–192]. The fact that this experimental evidence for the formation of the core-excitonic state is seen justifies the need for BSE calculations, where core-exciton states are taken into account.

Figure 6.8 shows the calculated RIXS maps for the 3 polarization directions:
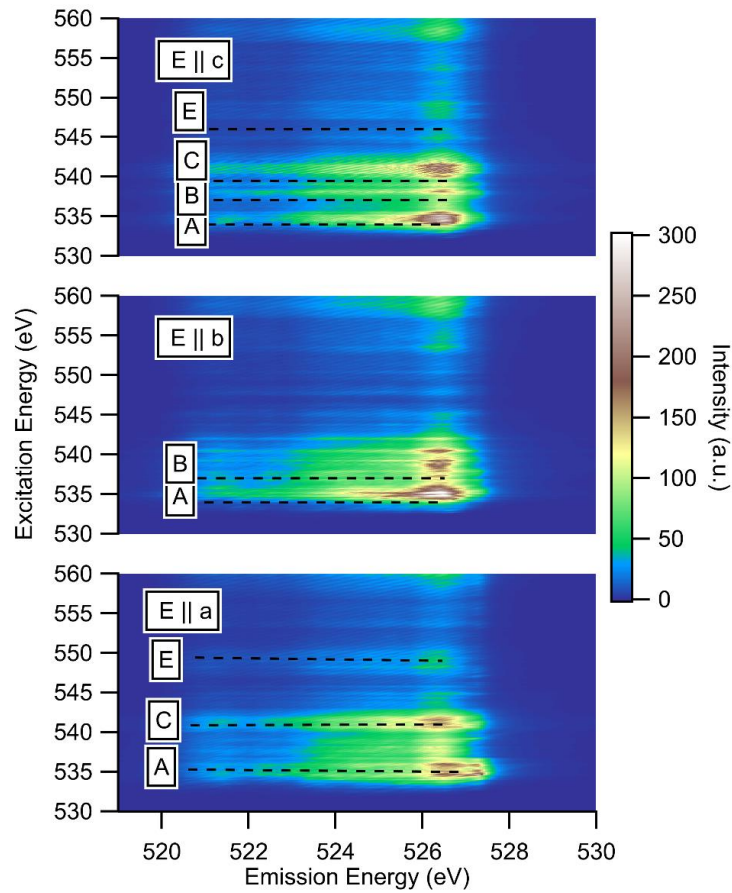
Figure 6.8. Calculated O K RIXS maps of β-Ga$_2$O$_3$ for the 3 polarization directions: **E‖ *a*** (bottom), **E‖ *b*** (middle), and **E‖ *c*** (top).

Please note that the colorscales of Figures 6.10 and 6.11 are different (the intensity is plotted in arbitrary units), and as such the intensities cannot be compared directly between the 2 Figures.

It is important to note that no additional broadening was applied to the calculated RIXS maps (only a very small broadening was applied to be able to see the spectral features, which was much less than 0.5 and 0.1 eV). Furthermore, while the experimental spectra are the sum of the coherent and incoherent (e.g., due to electron-phonon scattering) fractions, the calculated spectra consist of only the coherent fraction. Thus, at first glance the maps appear to look rather different to those in Figure 6.9. However, in fact there is a good correspondence of the calculated and experimental RIXS maps. All the main spectral features are reproduced, and the same absorption resonances (A-E) enhanced in the different polarization directions are seen as in the experimental maps in Figure 6.10. Applying additional broadening would further improve the correspondence.

6.4.3 XAS spectra

Figure 6.9 shows the experimental XAS spectra for the 3 polarization directions:
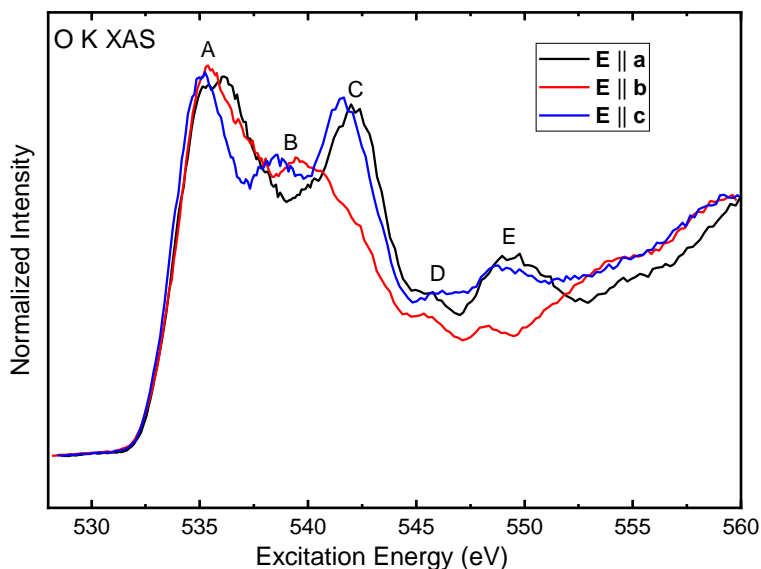
Figure 6.9. Partial fluorescence yield (PFY) O K absorption spectra of β-Ga_2O_3 for the 3 polarization directions: **E ∥ a** (black), **E ∥ b** (red) and **E ∥ c** (blue). The spectra were obtained from the RIXS maps in Figure 6.10 above, by integrating the emission intensity in the emission spectator region of the maps for

each excitation energy. The spectra were normalized to the intensity at 560 eV. Prominent absorption resonance features are labeled (A-E).

The spectra were obtained from the RIXS maps in Figure 6.7 above, by taking vertical cuts through the maps, and integrating over the same emission energy region as in the spectator region in the maps. The spectra were then normalized to the peak maximum of the feature at 560 eV.

There are several absorption features, labeled A-E, that are enhanced in some polarization directions while reduced in others. As mentioned above for the XES spectra, the dipole transition matrix elements depend on the polarization of the x-ray source, as well as on the position of the electron, i.e., what bonds the O atom it comes from is forming with the other Ga and O atoms. Figure 6.10 a) shows the XAS spectra calculated for O1, O2, and O3, and b) shows the average for the 3 polarization directions.
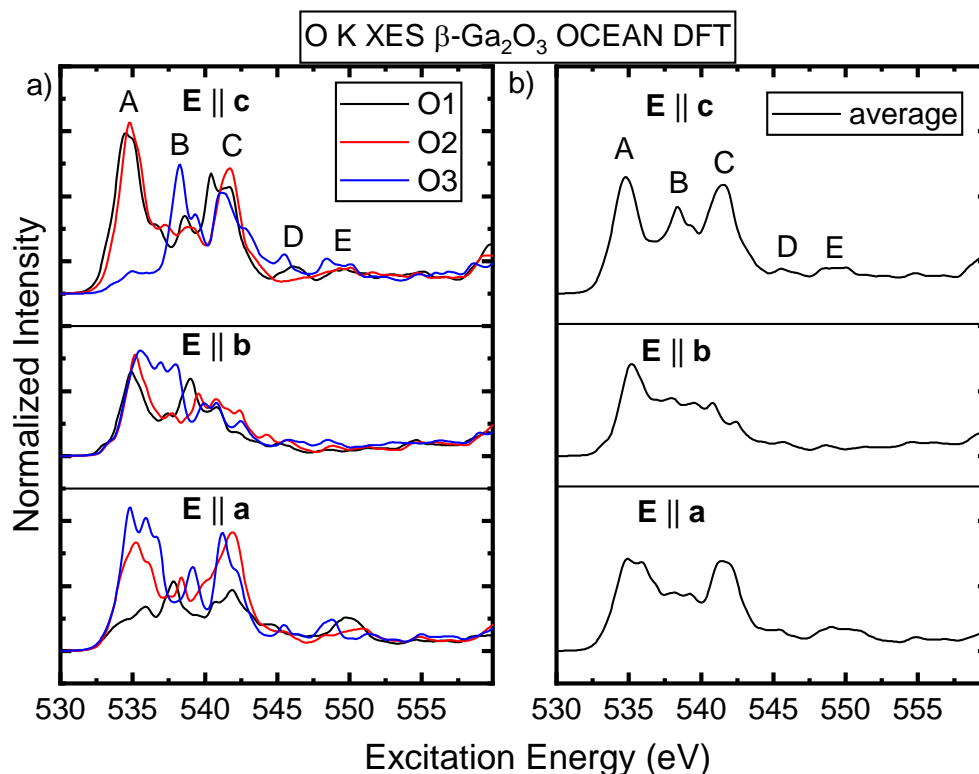
Figure 6.10. DFT-calculated a) contributions from differently coordinated O atoms, i.e., O1 (black), O2 (red) and O3 (blue) to the absorption spectra and b) their average (black) for the 3 polarization directions:

E ∥ a (bottom), **E ∥ b** (middle), and **E ∥ c** (top). The absorption spectra were calculated on an arbitrary excitation energy scale and were aligned to match the feature positions of the experimental spectra. The same shift was used for all 3 spectra. Furthermore, the excitation energy axis of the calculations was stretched by a factor 1.05 for best alignment of the spectral features in the experiment and calculation. The same broadening parameters were applied as for the XES spectra (Figure 6.5). The spectra were normalized to the intensity at 560 eV. Prominent absorption resonance features are labeled (A-E).

Feature A is present for all polarization directions. This absorption resonance is due to the core-exciton formation, and is rather similar for all polarization directions in the experiment. In Figure 6.9, feature B is present in **E ∥ b**, and **E ∥ c**, but absent in **E ∥ a**. In Figure 6.10, feature B is seen most strongly when **E ∥ c** , and comes from the tetrahedrally-coordinated O3. Conversely, features C and E are present in **E ∥ a**, and **E ∥ c**, but absent in **E ∥ b** in Figure 6.9. In the calculations, the octahedrally-coordinated O2 strongly contributes to feature C when **E ∥ a** and **E ∥ c**, while O1 contributes to feature E when

E ∥ a. According to ref.[57], feature B is missing in the absorption spectra of α-Ga_2O_3, which only has octahedrally coordinated O atoms. Meanwhile, Feature C is strong for α-Ga_2O_3 (ref.[57]). This corroborates the results above, i.e., that feature B appears to stem from tetrahedrally coordinated O atoms, while C is likely to appear from octahedrally-coordinated O atoms.

Figure 6.11 shows a comparison of the experimental and calculated (with experimental and lifetime broadening) XAS spectra:
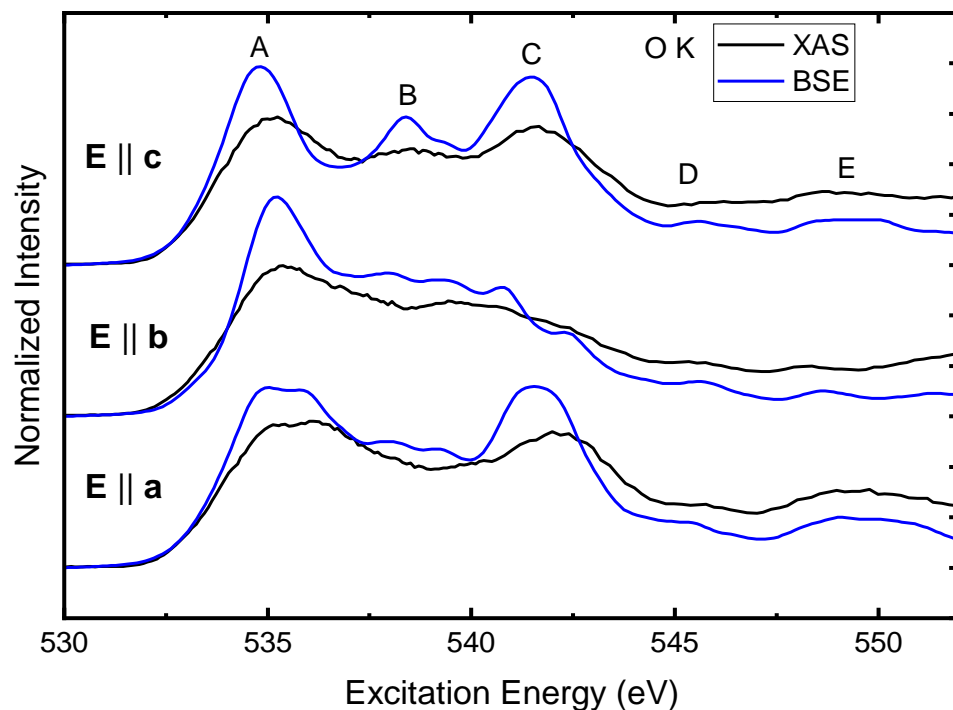
Figure 6.11. Comparison of the experimental (black) and calculated with experimental and lifetime broadening (blue) XAS spectra for the 3 polarization directions. The absorption spectra were calculated on an arbitrary excitation energy scale and were aligned to match the feature positions of the experimental spectra. The same shift was used for all 3 spectra. Furthermore, the excitation energy axis of the calculations was stretched by a factor 1.05 for best alignment of the spectral features in the experiment and calculation. The spectra are normalized to the area under the curves.

Overall, there is a good correspondence of the calculations and experiment. The same absorption features (A-E) are present/absent for the 3 polarization directions in the calculated spectra as in the experimental spectra, although the experimental spectra are significantly broadened compared to the calculated spectra.

6.4.4   RIXS spectra

Now, the experimental and calculated (with experimental and lifetime broadening) resonant XES spectra (referred to as RIXS spectra) are compared. Individual RIXS spectra were extracted from the RIXS maps in Figure 6.10 above by taking horizontal cuts through the maps. As already

mentioned, such spectra will contain both coherent and incoherent contributions, while the calculated spectra contain the coherent part only. Thus, the method presented in literature [193,194] of subtracting the incoherent fraction is employed here.

The spectra have contributions from higher harmonics, so the first step is to subtract these contributions prior to the subtraction procedure, as shown in Figure 6.12 as an example.
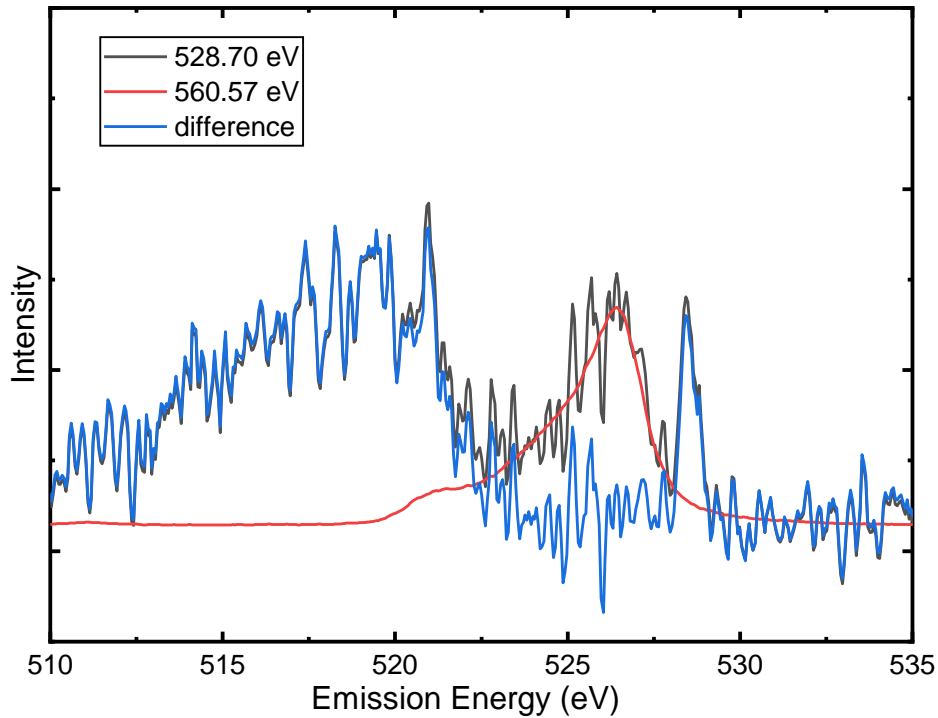
Figure 6.12. Example of subtracting the contribution from higher harmonics fraction for the RIXS spectrum at excitation energy 528.70 eV. (Black) original spectrum, (red) non-resonant emission spectrum at excitation energy 560.57 eV, and (blue) the resulting spectrum.

The black spectrum in Figure 6.12 is measured at the lowest excitation energy (528.70 eV), which is well below the absorption threshold at ~ 532 eV. In Figure 6.12, it is clear that the peak at ~ 520 eV comes from excitation into "virtual" states (see explanation below), while the peak at ~526 eV is from excitation into states at or above the CBM. Since we are below the absorption threshold, this peak must come from excitation by higher harmonics. The red spectrum is measured at the highest excitation energy (560.57 eV), which is treated as completely incoherent. One can see that its peak maximum is also at ~ 526 eV, confirming that

the peak in the black spectrum must arise from higher harmonics. So the maximum amount of the red spectrum is subtracted from the black one, such that there are no negative intensities, resulting in the blue spectrum. It is assumed that the contribution from higher harmonics is independent of the excitation energy at which the spectra are measured. So the same amount is subtracted from all the subsequent spectra.

After subtracting the higher harmonics from all spectra, another spectrum that is significantly above the absorption threshold is chosen, which is treated as completely incoherent. Here, the spectrum at excitation energy ~ 540 eV was taken, rather than the spectrum at ~ 560 eV because spectra at excitation energies above 540 eV have a satellite structure at higher emission energies (~528 eV). Figure 6.13 shows this additional satellite structure at 560.57 eV compared to the spectra at 539.95 eV.
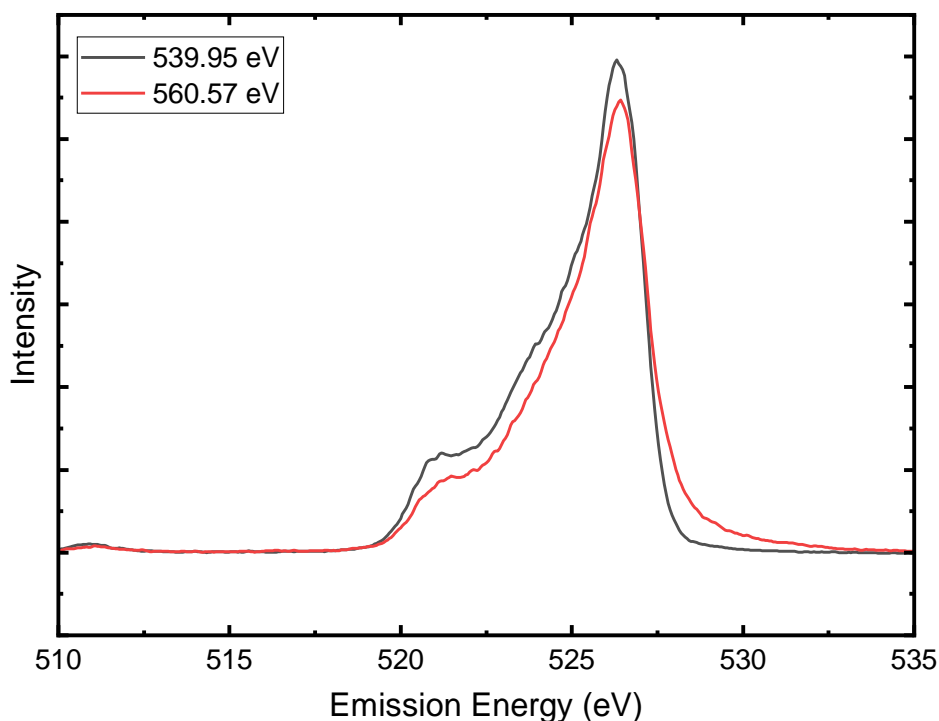
Figure 6.13. The non-resonant spectra measured at excitation energies of 539.95 eV (black) and 560.57 eV (red). The spectra measured with 560.57 eV have an additional satellite structure at ~ 528 eV.

One possible explanation would be Wentzel-Druyvesteyn (WD) satellites that appear when the system is doubly-ionized (as in H_2O as reported in ref.[195]). Such satellites would complicate the subtraction procedure, the spectrum at ~ 540 eV was taken.

Then, its maximum fraction is subtracted from each RIXS spectrum, such that there are no negative intensities. The resulting coherent fraction is then compared with the calculated RIXS spectra, as shown in Figure 6.14 for one of the spectrums as an example. The calculated RIXS spectra have an arbitrary emission energy scale so they were shifted and stretched (by a factor of 1.1) to align with the energy scale of the experimental spectra for the best correspondence of the spectral features. The shift and stretch was the same for all spectra.
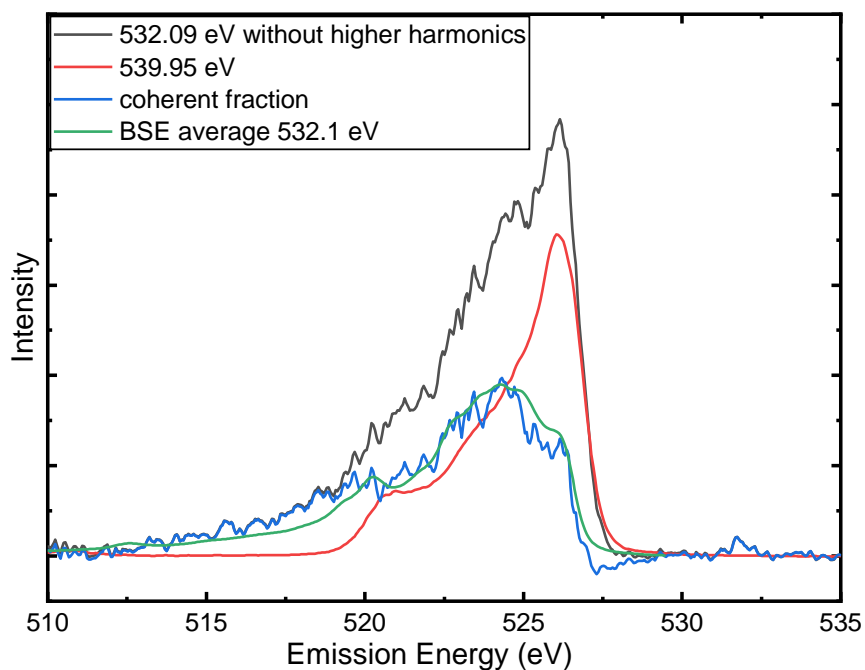
Figure 6.14. Example of subtracting the incoherent fraction for the RIXS spectrum at excitation energy 532.1 eV. (Black) original spectrum after subtracting higher harmonics from it, (red) non-resonant emission spectrum at excitation energy 540.0 eV, (blue) resulting coherent fraction, and (green) the BSE-calculated RIXS spectrum (with experimental and lifetime broadening) at excitation energy 532.1 eV. The RIXS spectra were calculated on an arbitrary emission energy scale and were shifted and stretched (factor of 1.1) to align with the energy scale of the experimental spectra for the best correspondence of the spectral features.

In addition to the procedure outlined above, for some spectra, particularly those within the vicinity of the absorption edge, the non-resonant spectrum had to be shifted to lower excitation energies (up to -0.8 eV) before it could be subtracted from the RIXS spectra. This effect could have several possible explanations, for example, interaction of the excited electron with the remaining electronic system.[196] Spectator shifts of similar magnitude in molecules have been reported in literature (such as gas-phase water[181], ammonia[191] or methanol[190] by our group, and CO[197] and N_2[198] by others). However, it would be hard to expect the same explanation for a single crystal as for molecules. Another possibility would be the Wentzel-Druyvesteyn (WD) satellites mentioned above. In general, this subtraction procedure does have its limitations, and the amount by which the spectrum has to be shifted is rather subjective.

Figures 6.15, 6.16, and 6.17 show the resulting comparison of the coherent fraction and calculated RIXS spectra for the 3 polarization directions:
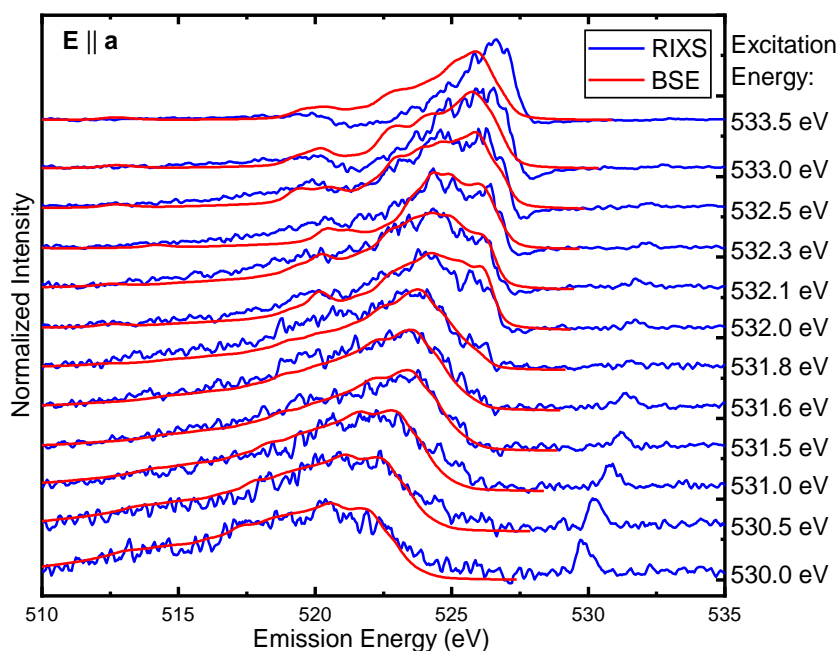
Figure 6.15. Coherent fraction of the RIXS spectra compared with the calculated RIXS spectra at selected excitation energies for **E‖ a**. The experimental spectra are normalized to the peak maxima, and the calculated spectra are scaled for the best correspondence to the experiment.
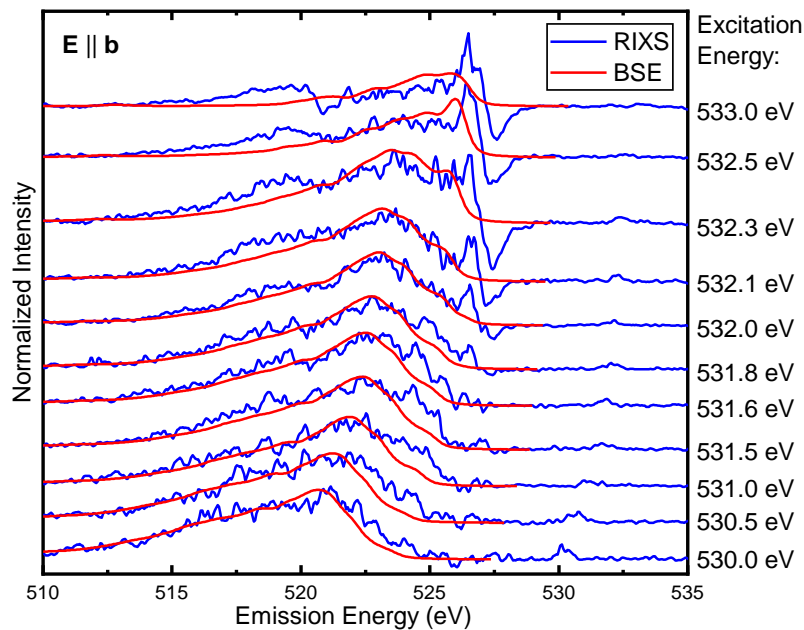
Figure 6.16. Coherent fraction of the RIXS spectra compared with the calculated RIXS spectra at selected excitation energies for **E ∥ *b***. The experimental spectra are normalized to the peak maxima, and the calculated spectra are scaled for the best correspondence to the experiment.
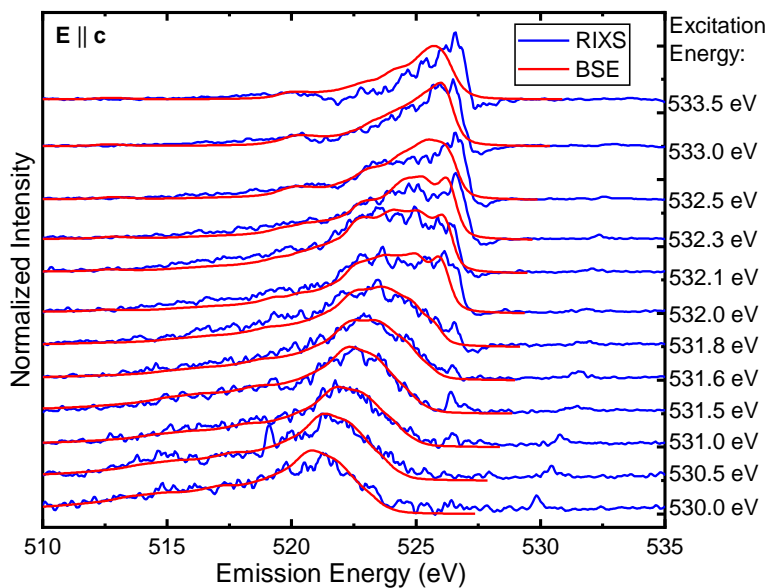
Figure 6.17. Coherent fraction of the RIXS spectra compared with the calculated RIXS spectra at selected excitation energies for **E ∥ *c***. The experimental spectra are normalized to the peak maxima, and the calculated spectra are scaled for the best correspondence to the experiment.

Overall, there is a very good agreement between experiment and calculations when the excitation energy is below or close to the absorption threshold (i.e., ≤ 532 eV) for all 3 polarization directions. The overall results/trends are also very similar for the 3 directions. Below the absorption edge (~532 eV), due to the linewidths of the intermediate state in the RIXS process (see formula 2.12 in Chapter 2), there is the possibility to excite electrons into "virtual" states with short lifetimes. For these excitations, the energy loss (i.e., difference between excitation and emission energy of the photon) must be constant. Thus, a Raman shift is observed, i.e., the emission energy shifts with excitation energy for the first several spectra below the absorption edge. The spectral shape is rather similar for these spectra as well.

Above the absorption edge at ~532 eV, the spectral shape changes significantly. For higher excitation energies, the coherent fraction decreases rapidly. This is because as the excitation energy is increased, there are more available states above the lowest conduction band to excite the electron into. The phase-space for scattering increases the higher in the conduction band the electron is excited to. Thus, the probability for electron-phonon scattering increases for the excitation and emission processes as well. This means that the relative amount of incoherent fraction subtracted increases rapidly, so it becomes more and more difficult to determine the coherent fraction accurately using this subtraction method. Thus, the agreement between experiment and calculations is not as good for the last few excitation energies. For all 3 polarization directions, there are also some discrepancies between experiment and calculations at the high emission energies, i.e., close to the VBM. This may indicate that there are additional scattering processes in this region that are not taken into account with this subtraction method, as was reported before.[194]

Overall, one can see that the spectra for E ∥ a are slightly broader, something that was seen before in the non-resonant XES spectra. The agreement between experiment and theory is slightly worse for E∥ b, with some additional intensity at emission energy ~524 eV. This is likely due to some additional satellites or scattering processes that were not taken into account. Nonetheless, overall, the BSE calculations are able to describe the RIXS spectra rather well, particularly for spectra with excitation energy close to the absorption edge. In the next section, a closer look is taken at the coherent fractions and how one can extract information about the dephasing time from them.

Figure 6.18 shows the coherent fraction as a function of the excitation energy for all 3 polarization directions:
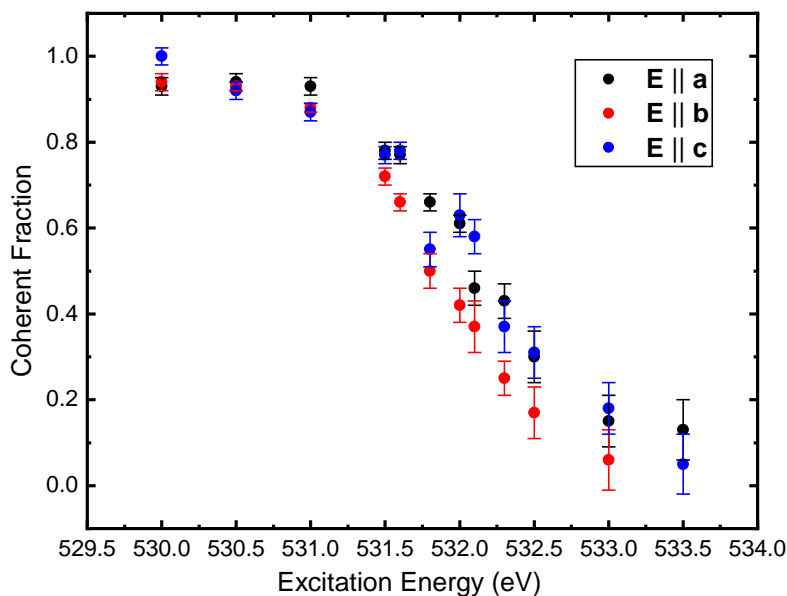
Figure 6.18. Coherent fraction as a function of the excitation energy for the 3 polarization directions: **E ‖ a** (black), **E ‖ b** (red) and **E ‖ c** (blue).

For spectra at lower excitation energies (below or around the absorption threshold), the error bars are determined as follows: more or less of the incoherent spectrum is subtracted (corresponding to a smaller or larger coherent fraction respectively) until the comparison of the theory and calculations still appears reasonable. The upper/lower limit of the error bars corresponds to the conditions where the experiment and calculations begin to have a poor agreement. For spectra at higher excitation energies, there are two effects: the estimation method described above leads to smaller error bars because the range at which the subtraction method gives a reasonable result is narrower. However, the agreement between experiment and calculations is worse at higher excitation energies. To take both into account, the uncertainty estimated by the first method is

multiplied by a factor between the coherent fraction for the lowest excitation energy and the coherent fraction for the given slice. Then the greater uncertainty in these data points is accounted for. In general, this estimation of the uncertainty is highly subjective and not a quantitative one.

As expected, the overall trend is the same for all polarization directions: as explained above, the coherent fraction decreases with increasing excitation energy. One can also see that the coherent fraction decreases more rapidly when $\mathbf{E} \parallel \mathbf{b}$ compared to the other directions.

Using the core-hole clock formalism,[199] the coherent fractions above the absorption edge can be converted to dephasing times, i.e. information about the time-scales of the electron-phonon scattering process can be obtained using the formula below:

$$\tau_{ph} = \frac{f}{R_c(1-f)}$$

Here, τ_{ph} is the lifetime of the electron-phonon scattering, i.e., the dephasing time, f is the coherent fraction, and R_c is the core-hole decay rate. Taking the core-hole lifetime, τ_c, of O 1s as 3.5 fs (lifetime width $\Gamma = \frac{\hbar}{\tau_{ph}} = 190$ meV)[75], $R_c \sim 0.29 \cdot 10^{15}$ Hz), the dephasing time is calculated and plotted as a function of the excitation energy (together with the coherent fractions) for all 3 polarization directions in Figure 6.19:
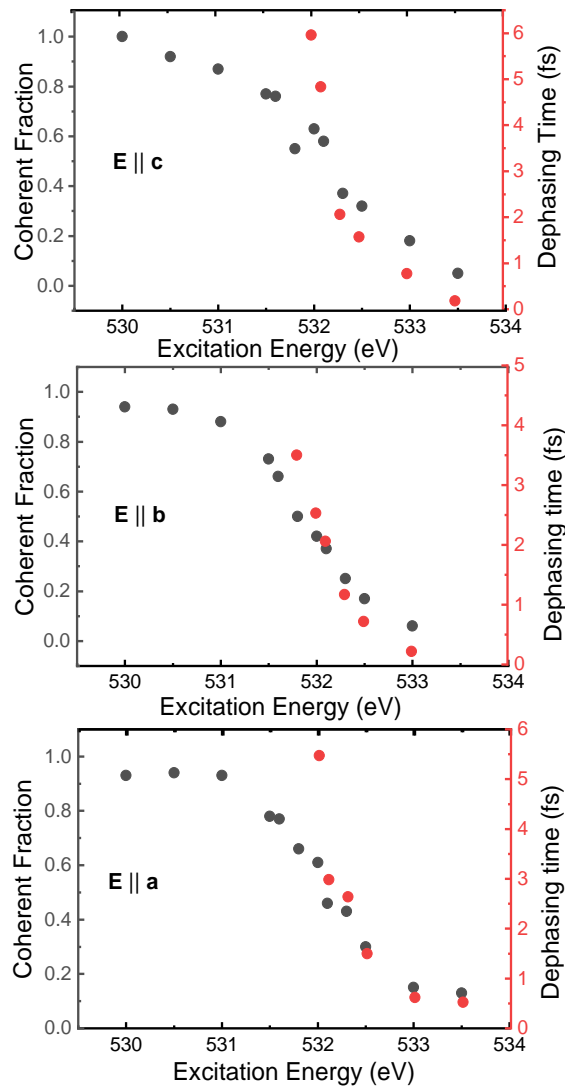
Figure 6.19. Coherent fraction (black) and dephasing time (red) of the RIXS spectra as a function of the excitation energy for the 3 polarization directions.

At the absorption edge, the phonon-scattering time is almost twice as large as the core-hole lifetime. So the absorption-emission transitions can be treated as a coherent inelastic-scattering process. Above the absorption edge, τ_{ph} rapidly decreases, and already at 532.5 eV, it is smaller than τ_c. So RIXS spectra at and above this excitation energy can be treated as non-resonant emission spectra. The results are similar for the 3 directions. The main differences are due to the limitations of the subtraction procedure to determine the coherent fraction (and hence τ_{ph}). Thus,

we see that the electron-phonon scattering happens on a femtosecond timescale, in the range of 3 $\pm$ 2 fs. This corresponds to results obtained in literature for the electron-phonon scattering times of β-Ga$_2$O$_3$, e.g., the electron-photon scattering time was more precisely determined from ultrafast transmission spectroscopy measurements as 4.5 $\pm$ 0.4 fs[200].

6.5 Conclusion and outlook

In this chapter, the polarization-dependent XES, XAS, and RIXS spectra of β-Ga$_2$O$_3$ single crystals were presented. By rotating the samples, it was possible to perform measurements where the polarization of the incoming x-ray photon was oriented parallel to each of the unit cell vectors. Calculations of the spectra corresponding to each experimental configuration using the BSE method in the OCEAN code were also performed. It was found that the calculations are able to reproduce the main features in the experimental spectra. Clear signatures of the core-exciton formation in all of the experimental RIXS spectra were observed. Most strikingly, significant differences in all spectra for the different polarization directions, both in the experiment and in the calculations were seen. These differences can be qualitatively explained by the differences in the dipole transition matrix elements, which depend on the polarization of the incoming photon, as well as which inequivalent O atom (O1, O2, O3) the electron originates from. Finally, the electron-photon scattering lifetimes from the coherent fractions of the experimental RIXS spectra were obtained, which are 3 $\pm$ 2 fs, in accordance with literature values.

For future research, the focus would be on describing the spectra of β-Ga$_2$O$_3$ powder, for which the first result is presented below.

6.5.1 Preliminary results for β-Ga₂O₃ powder

In addition to the two single crystals described in this chapter, measurements were also performed on β-Ga$_2$O$_3$ in powdered form. Figure 6.20 shows the resulting XAS spectrum, compared with the average spectra of the 3 polarization directions (Figure 6.9 with the XAS spectra of the 3 polarization directions is also reproduced here for clarity):
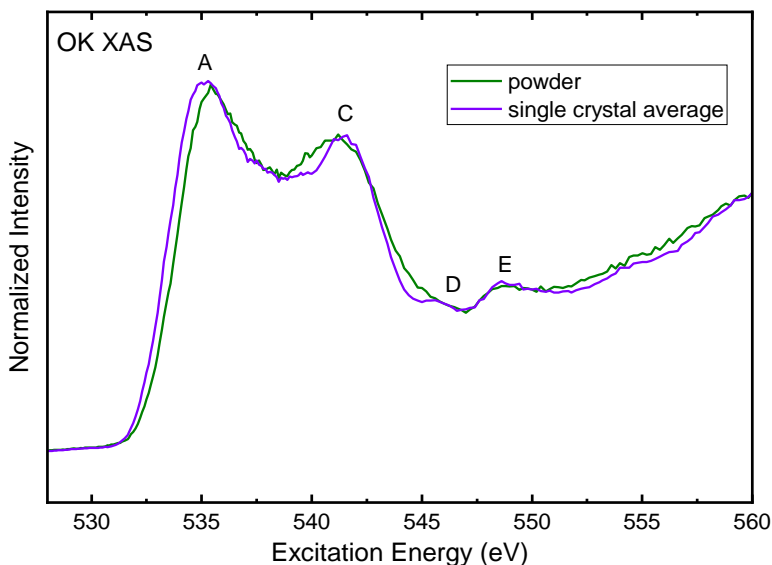
Figure 6.20. Partial fluorescence yield (PFY) O K absorption spectra of β-Ga$_2$O$_3$ powder (green), and the average of the spectra for the 3 polarization directions (purple). The spectra were normalized to the peak maximum of the feature at 560 eV. Prominent absorption resonance features are labeled (A-E).
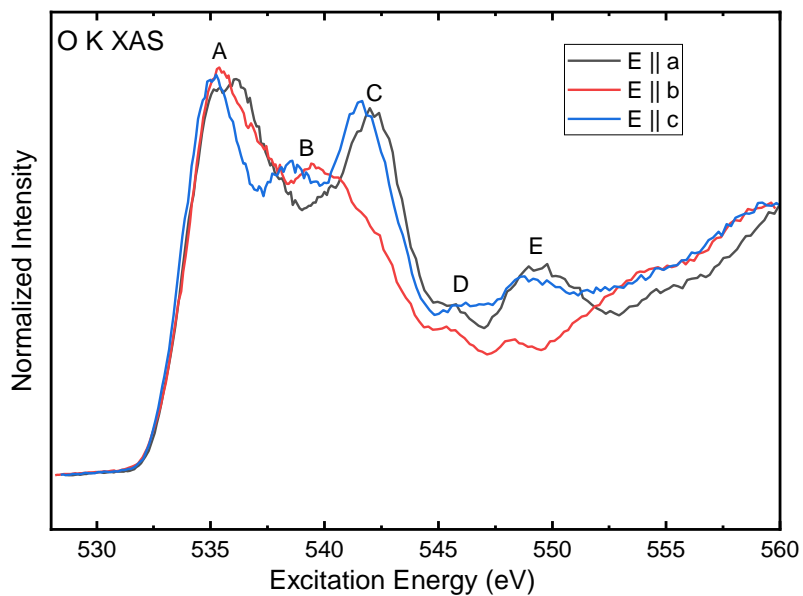
Figure 6.21. Figure 6.9 reproduced.

One can see that the spectrum averaged over the 3 polarization directions already describes the powder well, even though the powder is polycrystalline, i.e., it consists of many different randomly-oriented β-Ga_2O_3 crystallites. The next steps would be to calculate spectra of polycrystalline or even amorphous Ga_2O_3.

7 Summary

Ga_2O_3 is an UWBG material that is highly relevant for a variety of applications in electronics, gas-sensors, and photovoltaics, with the amount of research published about Ga_2O_3 exponentially increasing in the last decade.[17] In this thesis, the chemical and electronic structure of Ga_2O_3 samples of different morphology, i.e., β-Ga_2O_3 single crystals and nanocrystalline thin-films, were studied using a variety of electron and x-ray spectroscopic techniques, which allowed to obtain complimentary bulk and surface-sensitive information. Ab-initio theoretical calculations were performed as well, which gave further insights into the electronic properties of Ga_2O_3.

In the first part of this thesis, the chemical structure of the Ga_2O_3/CIGSe interface in thin-film solar cells was investigated by XPS, XAES, and HAXPES. Particular focus was placed on understanding the impact of the RbF PDT and ammonia-based rinsing step on the CIGSe absorber and Ga_2O_3 buffer surfaces, as well as on the Ga_2O_3/CIGSe interface. Rb and F were found on the non-rinsed RbF-treated CIGSe surface, which were then partially (Rb) and completely (F) removed by the rinse. In addition, the rinse removed Ga-F, Ga-O, and In-O surface bonds. The surface GGI ratio was reduced as a result of the rinse as well. With the sputter-deposition of Ga_2O_3, the formation of In-O bonds, and the diffusion of Rb, and small amounts of F into the Ga_2O_3 buffer layer could be identified for both samples with the rinsed and non-rinsed CIGSe. The chemical composition of Ga_2O_3 buffer layer was found to not depend on the buffer layer thickness and the rinsing of the absorber.

The large amounts of Rb-F on the non-rinsed absorber and the diffusion of Rb and F into the buffer layer could potentially explain the significantly lower efficiencies (more than 8% reduction) observed in the complete solar cells with non-rinsed CIGSe absorbers. These changes in the chemical structure are likely to lead to changes in the electronic structure as well. Thus, in the future, one would conduct a detailed study of the band alignment, in particular, the conduction band alignment at the Ga_2O_3/CIGSe interface.

The electronic structure, specifically the VB and VBM of Ga_2O_3 was studied as well. The goal was to understand the impact of various factors, such as the morphology, crystal structure, and sample preparation on the VB and VBM of Ga_2O_3. Three different samples, namely the 100 nm Ga_2O_3/CIGSe samples, a UHV-cleaved β-Ga_2O_3 single crystal, and a mild Ar^+-ion treated β-

Ga$_2$O$_3$ single crystal, were measured with PES at a wide range of excitation energies: 70 eV – 6.3 keV. DFT calculations for β-Ga$_2$O$_3$ were also performed to add some insights on the PES spectra.

The VBM of the UHV-cleaved β-Ga$_2$O$_3$ single crystal was determined to be 4.8$\pm$0.1 eV, independent of the photon excitation energy, and in line with the results in literature. In contrast, the VBM of the rinsed and non-rinsed 100 nm Ga$_2$O$_3$/CIGSe samples was shown to be significantly different when measured at low and high photon excitation energies, i.e., the VBM is different for the surface and the bulk. A strong tail was observed, especially in the surface-sensitive measurements, which could not be explained by experimental and lifetime broadening. This is likely due to surface defects and/or C and O adsorbed at the surface. The VBM was also observed to shift away from E$_F$ for these samples. This is likely a result of band bending due to surface adsorbates. The shapes of the VBs of the 100 nm Ga$_2$O$_3$/CIGSe samples were much broader than that of the cleaved single crystal as well.

The VB spectra of the Ar$^+$-ion treated β-Ga$_2$O$_3$ single crystal measured at different photon excitation energies were observed to be somewhat intermediate between the other two samples. The VB shape was more similar to the 100 nm Ga$_2$O$_3$/CIGSe sample spectra, although some features from the cleaved β-Ga$_2$O$_3$ single crystal could be observed as well. A tail was also observed, although less strong than in the 100 nm Ga$_2$O$_3$/CIGSe sample spectra. Band bending effects, i.e., a shift of the VBM away from E$_F$ with increasing photon excitation energy, was observed for these samples as well. It was thus concluded that the Ar$^+$-ion treatment appears to introduce defects such as O vacancies to the surface.

In the future, more HAXPES measurements would need be performed for the samples where a significant tail was observed, particularly at higher photon excitation energies, to understand better the differences between the surface-sensitive and bulk-sensitive results. In addition, it would be important to carry out the most surface-sensitive ultra-violet PES (UPS) measurements (with photon excitation energies of 21.2 eV and 40.8 eV), and inverse PES (IPES) measurements, to determine the band edges relative to E$_F$ at the surface, as well as the valence band and conduction band alignments at the surface. As mentioned above, the conduction band alignment in particular affects the charge transport and directly influences the efficiencies of the devices. Thus, further insights into the device performance could be obtained.

It is also important to conduct a more fundamental study of the bulk electronic structure of β-Ga_2O_3. In the last part of the thesis, polarization-dependent XES, XAS, and RIXS spectra at the O K edge of β-Ga_2O_3 were obtained. The measurements were performed by rotating the samples with respect to the incoming x-ray polarization. Since the dipole transition matrix elements depend on the polarization of the incident x-ray beam with respect to the crystal orientation, polarization-dependent measurements allow to selectively probe different regions within the band structure of β-Ga_2O_3. In addition, β-Ga_2O_3 is highly anisotropic in its crystal structure, and the spectral differences can originate from different inequivalent O atoms. Calculations in the BSE method in the OCEAN code were performed, corresponding to each experimental configuration.

Differences in all spectra for all polarization directions were seen in both the experiments and the calculations. The calculations are able to correctly capture all the main features of the experimental spectra. Evidence for core-exciton formation was seen in all the experimental RIXS spectra as well. The electron-phonon scattering lifetimes were obtained from the coherent fractions of the experimental RIXS spectra as 3 ± 2 fs, corresponding to literature values. In the future, one could investigate the XES, XAS, and RIXS spectra of powdered β-Ga_2O_3 in detail. For a more detailed understanding of the bulk electronic structure of the Ga_2O_3 used as the buffer layer in CIGSe-based solar cells, some other future investigations could be measuring and calculating the RIXS maps for nanocrystalline (or even amorphous) Ga_2O_3.

Overall, detailed and depth-varied results on the chemical and electronic structure of Ga_2O_3 were obtained in this thesis, which allowed to gain insights into the properties of applied and fundamental Ga_2O_3 systems. The results could potentially be used for optimizing the efficiencies and performance of Ga_2O_3 devices as well.

List of Figures

127

List of Tables

List of Abbreviations and Symbols

α'	Modified Auger Parameter
ACS	American Chemical Society
ALS	Advanced Light Source
ARPES	Angle-Resolved Photoemission Spectroscopy
BSE	Bethe-Salpeter Equation
CIF	Crystallographic Information Files
CB	Conduction Band
CBD	Chemical Bath Deposition
CBM	Conduction Band Minimum
CL	Core Level
CIGSe	$Cu(In,Ga)Se_2$
DCM	Double Crystal Monochromator
DFT	Density Functional Theory
DOS	Density of States
E_{bin}	Binding Energy
E_F	Fermi level
E_{kin}	Kinetic Energy
E_g	Bandgap
E_{vac}	Vacuum level
ELNES	Energy-Loss Near-Edge Fine Structure
FET	Field-effect transistor
FF	Fill Factor
FVLS-PGM	Focusing Variable-line-space Plane-grating Monochromator
Γ	Lifetime broadening
GGA	Generalized Gradient Approximation
GGI	Ga/(Ga+In) ratio
GMRES	Generalized Minimal Residual Method
$h\nu$	Photon excitation energy
HAXPES	Hard x-ray Photoelectron Spectroscopy
HOMO	Highest Occupied Molecular Orbital
ICP-MS	Inductively-coupled Plasma-mass Spectrometry
IMFP	Inelastic Mean Free Path
IPES	Inverse Photoelectron Spectroscopy
ITO	Indium Tin Oxide
J_{sc}	Short circuit current density
LAPW	Linearized Augmented Plane Wave
LDA	Local Density Approximation
LUMO	Lowest Unoccupied Molecular Orbital
MFE lab	Materials for Energy laboratory

NIST	National Institute of Standards and Technology
PAW	Projector Augmented Wave
PBE	Perdew-Burke-Ernzerhof
PES	Photoelectron spectroscopy
PDT	Postdeposition treatment
PFY	Partial fluorescence yield
RF	Radio-frequency
RIXS	Resonant Inelastic X-ray Scattering
SCF	Self-consistent field cycle
SGM	Spherical Grating Monochromator
τ_{ph}	Electron-phonon scattering lifetime
TCO	Transparent Conductive Oxide
TPP2M	Tanuma Powell and Penn algorithm
UHV	Ultra-high vacuum
UPS	Ultra-violet photoelectron spectroscopy
UV	Ultra-violet
UWBG	Ultrawide-bandgap
V_{oc}	Open-circuit Voltage
VB	Valence Band
VBM	Valence Band Maximum
WD	Wentzel-Druyvesteyn
XAES	X-ray Auger Electron Spectroscopy
XAS	X-ray Absorption Spectroscopy
XES	X-ray Emission Spectroscopy
XPS	X-ray Photoelectron Spectroscopy
XRF	X-ray Fluorescence
ZSW	Zentrum für Sonnenenergie-und Wasserstoff-Forschung Baden-Württemberg

References

(1)   *The Nobel Prize in Physics 1956*. NobelPrize.org.
        https://www.nobelprize.org/prizes/physics/1956/summary/ (accessed 2023-10-16).
(2)   Sze, S. M. *The Physics of Semiconductor Devices*, 3rd ed.; Wilez: New York, 1969.
(3)   Blakemore, J. S. Semiconducting and Other Major Properties of Gallium Arsenide. *J. Appl. Phys.*
        1982, *53* (10), R123–R181. https://doi.org/10.1063/1.331665.
(4)   Tsao, J. Y.; Chowdhury, S.; Hollis, M. A.; Jena, D.; Johnson, N. M.; Jones, K. A.; Kaplar, R. J.; Rajan,
        S.; Van de Walle, C. G.; Bellotti, E.; Chua, C. L.; Collazo, R.; Coltrin, M. E.; Cooper, J. A.; Evans, K. R.;
        Graham, S.; Grotjohn, T. A.; Heller, E. R.; Higashiwaki, M.; Islam, M. S.; Juodawlkis, P. W.; Khan,
        M. A.; Koehler, A. D.; Leach, J. H.; Mishra, U. K.; Nemanich, R. J.; Pilawa-Podgurski, R. C. N.;
        Shealy, J. B.; Sitar, Z.; Tadjer, M. J.; Witulski, A. F.; Wraback, M.; Simmons, J. A. Ultrawide-
        Bandgap Semiconductors: Research Opportunities and Challenges. *Adv. Electron. Mater.* **2018**, *4*
        (1), 1600501. https://doi.org/10.1002/aelm.201600501.
(5)   Higashiwaki, M.; Sasaki, K.; Kuramata, A.; Masui, T.; Yamakoshi, S. Gallium Oxide (Ga_2O_3) Metal-
        Semiconductor Field-Effect Transistors on Single-Crystal β-Ga_2O_3 (010) Substrates. *Appl. Phys.
        Lett.* **2012**, *100* (1), 013504. https://doi.org/10.1063/1.3674287.
(6)   Higashiwaki, M.; Sasaki, K.; Kuramata, A.; Masui, T.; Yamakoshi, S. Development of Gallium Oxide
        Power Devices. *Phys. Status Solidi A* **2014**, *211* (1), 21–26.
        https://doi.org/10.1002/pssa.201330197.
(7)   Liu, A.-C.; Hsieh, C.-H.; Langpoklakpam, C.; Singh, K. J.; Lee, W.-C.; Hsiao, Y.-K.; Horng, R.-H.; Kuo,
        H.-C.; Tu, C.-C. State-of-the-Art β-Ga_2O_3 Field-Effect Transistors for Power Electronics. *ACS Omega*
        2022, *7* (41), 36070–36091. https://doi.org/10.1021/acsomega.2c03345.
(8)   Kokubun, Y.; Miura, K.; Endo, F.; Nakagomi, S. Sol-Gel Prepared β-Ga_2O_3 Thin Films for Ultraviolet
        Photodetectors. *Appl. Phys. Lett.* **2007**, *90* (3), 031912. https://doi.org/10.1063/1.2432946.
(9)   Chen, X.; Ren, F.-F.; Ye, J.; Gu, S. Gallium Oxide-Based Solar-Blind Ultraviolet Photodetectors.
        Semicond. Sci. Technol. **2020**, *35* (2), 023001. https://doi.org/10.1088/1361-6641/ab6102.
(10)   Guo, D. Y.; Wu, Z. P.; An, Y. H.; Guo, X. C.; Chu, X. L.; Sun, C. L.; Li, L. H.; Li, P. G.; Tang, W. H.
        Oxygen Vacancy Tuned Ohmic-Schottky Conversion for Enhanced Performance in β-Ga_2O_3 Solar-
        Blind Ultraviolet Photodetectors. *Appl. Phys. Lett.* **2014**, *105* (2), 023507.
        https://doi.org/10.1063/1.4890524.
(11)   Wang, J.; Ye, L.; Wang, X.; Zhang, H.; Li, L.; Kong, C.; Li, W. High Transmittance Ga_2O_3 Thin Films
        Deposited by Magnetron Sputtering and Post-Annealing for Solar-Blind Ultraviolet Photodetector.
        J. Alloys Compd. **2019**, *803*, 9–15. https://doi.org/10.1016/j.jallcom.2019.06.224.
(12)   Ogita, M.; Higo, K.; Nakanishi, Y.; Hatanaka, Y. Ga_2O_3 Thin Film for Oxygen Sensor at High
        Temperature. *Appl. Surf. Sci.* **2001**, *175–176*, 721–725. https://doi.org/10.1016/S0169-
        4332(01)00080-0.
(13)   Zhai, H.; Wu, Z.; Fang, Z. Recent Progress of Ga_2O_3-Based Gas Sensors. *Ceram. Int.* **2022**, *48* (17),
        24213–24233. https://doi.org/10.1016/j.ceramint.2022.06.066.
(14)   Pandeeswari, R.; Jeyaprakash, B. G. High Sensing Response of β-Ga_2O_3 Thin Film towards
        Ammonia Vapours: Influencing Factors at Room Temperature. *Sens. Actuators B Chem.* **2014**,
        195, 206–214. https://doi.org/10.1016/j.snb.2014.01.025.
(15)   Garud, S.; Gampa, N.; Allen, T. G.; Kotipalli, R.; Flandre, D.; Batuk, M.; Hadermann, J.; Meuris, M.;
        Poortmans, J.; Smets, A.; Vermang, B. Surface Passivation of CIGS Solar Cells Using Gallium Oxide.
        Phys. Status Solidi A **2018**, *215* (7), 1700826. https://doi.org/10.1002/pssa.201700826.

(16) Witte, W.; Paetel, S.; Menner, R.; Bauer, A.; Hariskos, D. The Application of Sputtered Gallium Oxide as Buffer for Cu(In,Ga)Se₂ Solar Cells. *Phys. Status Solidi RRL – Rapid Res. Lett.* **2021**, *15* (9), 2100180. https://doi.org/10.1002/pssr.202100180.

(17) *Gallium Oxide: Materials Properties, Crystal Growth, and Devices*; Higashiwaki, M., Fujita, S., Eds.; Springer Series in Materials Science; Springer International Publishing: Cham, 2020; Vol. 293. https://doi.org/10.1007/978-3-030-37153-1.

(18) Onuma, T.; Saito, S.; Sasaki, K.; Masui, T.; Yamaguchi, T.; Honda, T.; Higashiwaki, M. Valence Band Ordering in β-Ga₂O₃ Studied by Polarized Transmittance and Reflectance Spectroscopy. *Jpn. J. Appl. Phys.* **2015**, *54* (11), 112601. https://doi.org/10.7567/JJAP.54.112601.

(19) Tippins, H. H. Optical Absorption and Photoconductivity in the Band Edge of β-Ga₂O₃. *Phys. Rev.* **1965**, *140* (1A), A316–A319. https://doi.org/10.1103/PhysRev.140.A316.

(20) Orita, M.; Ohta, H.; Hirano, M.; Hosono, H. Deep-Ultraviolet Transparent Conductive β-Ga₂O₃ Thin Films. *Appl. Phys. Lett.* **2000**, *77* (25), 4166–4168. https://doi.org/10.1063/1.1330559.

(21) He, H.; Orlando, R.; Blanco, M. A.; Pandey, R.; Amzallag, E.; Baraille, I.; Rérat, M. First-Principles Study of the Structural, Electronic, and Optical Properties of Ga₂O₃ in Its Monoclinic and Hexagonal Phases. *Phys. Rev. B* **2006**, *74* (19), 195123. https://doi.org/10.1103/PhysRevB.74.195123.

(22) Duncan, D. A.; Mendelsberg, R.; Mezher, M.; Horsley, K.; Rosenberg, S. G.; Blum, M.; Xiong, G.; Weinhardt, L.; Gloeckler, M.; Heske, C. A New Look at the Electronic Structure of Transparent Conductive Oxides—A Case Study of the Interface between Zinc Magnesium Oxide and Cadmium Telluride. *Adv. Mater. Interfaces* **2016**, *3* (22), 1600418. https://doi.org/10.1002/admi.201600418.

(23) Witte, W.; Hempel, W.; Paetel, S.; Menner, R.; Hariskos, D. Influence of Sputtered Gallium Oxide as Buffer or High-Resistive Layer on Performance of Cu(In,Ga)Se₂-Based Solar Cells. *J. Mater. Res.* **2022**, *37* (11), 1825–1834. https://doi.org/10.1557/s43578-022-00608-z.

(24) Lowry, A. *High-Voltage Gallium Oxide Devices for Space Power Electronics, Phase I*. https://techport.nasa.gov/view/113274 (accessed 2023-10-21).

(25) Bauman, D. A.; Borodkin, A. I.; Petrenko, A. A.; Panov, D. I.; Kremleva, A. V.; Spiridonov, V. A.; Zakgeim, D. A.; Silnikov, M. V.; Odnoblyudov, M. A.; Romanov, A. E.; Bougrov, V. E. On Improving the Radiation Resistance of Gallium Oxide for Space Applications. *Acta Astronaut.* **2021**, *180*, 125–129. https://doi.org/10.1016/j.actaastro.2020.12.010.

(26) Galazka, Z. β-Ga₂O₃ for Wide-Bandgap Electronics and Optoelectronics. *Semicond. Sci. Technol.* **2018**, *33* (11), 113001. https://doi.org/10.1088/1361-6641/aadf78.

(27) Mu, W.; Jia, Z.; Yin, Y.; Hu, Q.; Li, Y.; Wu, B.; Zhang, J.; Tao, X. High Quality Crystal Growth and Anisotropic Physical Characterization of β-Ga₂O₃ Single Crystals Grown by EFG Method. *J. Alloys Compd.* **2017**, *714*, 453–458. https://doi.org/10.1016/j.jallcom.2017.04.185.

(28) Hoshikawa, K.; Ohba, E.; Kobayashi, T.; Yanagisawa, J.; Miyagawa, C.; Nakamura, Y. Growth of β-Ga₂O₃ Single Crystals Using Vertical Bridgman Method in Ambient Air. *J. Cryst. Growth* **2016**, *447*, 36–41. https://doi.org/10.1016/j.jcrysgro.2016.04.022.

(29) Fu, B.; Jian, G.; Mu, W.; Li, Y.; Wang, H.; Jia, Z.; Li, Y.; Long, S.; Shi, Y.; Tao, X. Crystal Growth and Design of Sn-Doped β-Ga₂O₃ : Morphology, Defect and Property Studies of Cylindrical Crystal by EFG. *J. Alloys Compd.* **2022**, *896*, 162830. https://doi.org/10.1016/j.jallcom.2021.162830.

(30) Galazka, Z. Growth of Bulk β-Ga₂O₃ Single Crystals by the Czochralski Method. *J. Appl. Phys.* **2022**, *131* (3), 031103. https://doi.org/10.1063/5.0076962.

(31) Ueda, N.; Hosono, H.; Waseda, R.; Kawazoe, H. Anisotropy of Electrical and Optical Properties in β-Ga₂O₃ Single Crystals. *Appl. Phys. Lett.* **1997**, *71* (7), 933–935. https://doi.org/10.1063/1.119693.

(32) Ricci, F.; Boschi, F.; Baraldi, A.; Filippetti, A.; Higashiwaki, M.; Kuramata, A.; Fiorentini, V.; Fornari, R. Theoretical and Experimental Investigation of Optical Absorption Anisotropy in β-Ga$_2$O$_3$. *J. Phys. Condens. Matter* **2016**, *28* (22), 224005. https://doi.org/10.1088/0953-8984/28/22/224005.

(33) Matsumoto, T.; Aoki, M.; Kinoshita, A.; Aono, T. Absorption and Reflection of Vapor Grown Single Crystal Platelets of β-Ga$_2$O$_3$. *Jpn. J. Appl. Phys.* **1974**, *13* (10), 1578–1582. https://doi.org/10.1143/JJAP.13.1578.

(34) Song, Y.; Ranga, P.; Zhang, Y.; Feng, Z.; Huang, H.-L.; Santia, M. D.; Badescu, S. C.; Gonzalez-Valle, C. U.; Perez, C.; Ferri, K.; Lavelle, R. M.; Snyder, D. W.; Klein, B. A.; Deitz, J.; Baca, A. G.; Maria, J.-P.; Ramos-Alvarado, B.; Hwang, J.; Zhao, H.; Wang, X.; Krishnamoorthy, S.; Foley, B. M.; Choi, S. Thermal Conductivity of β-Phase Ga$_2$O$_3$ and (Al$_x$Ga$_{1-x}$)$_2$O$_3$ Heteroepitaxial Thin Films. *ACS Appl. Mater. Interfaces* **2021**, *13* (32), 38477–38490. https://doi.org/10.1021/acsami.1c08506.

(35) Zheng, Y.; Swinnich, E.; Seo, J.-H. Investigation of Thermal Properties of β-Ga$_2$O$_3$ Nanomembranes on Diamond Heterostructure Using Raman Thermometry. *ECS J. Solid State Sci. Technol.* **2020**, *9* (5), 055007. https://doi.org/10.1149/2162-8777/ab981e.

(36) Ghadbeigi, L.; Sun, R.; Jesenovec, J.; Bhattacharyya, A.; McCloy, J.; Krishnamoorthy, S.; Scarpulla, M. A.; Sensale-Rodriguez, B. Electronic and Ionic Conductivity in β-Ga$_2$O$_3$ Single Crystals. *J. Appl. Phys.* **2022**, *131* (8), 085102. https://doi.org/10.1063/5.0073395.

(37) Lorenz, M. R.; Woods, J. F.; Gambino, R. J. Some Electrical Properties of the Semiconductor β-Ga$_2$O$_3$. *J. Phys. Chem. Solids* **1967**, *28* (3), 403–404. https://doi.org/10.1016/0022-3697(67)90305-8.

(38) Nagarajan, L.; De Souza, R. A.; Samuelis, D.; Valov, I.; Börger, A.; Janek, J.; Becker, K.-D.; Schmidt, P. C.; Martin, M. A Chemically Driven Insulator–Metal Transition in Non-Stoichiometric and Amorphous Gallium Oxide. *Nat. Mater.* **2008**, *7* (5), 391–398. https://doi.org/10.1038/nmat2164.

(39) Hariskos, D.; Hempel, W.; Menner, R.; Witte, W. Influence of Substrate Temperature during In$_x$S$_y$ Sputtering on Cu(In,Ga)Se$_2$ /Buffer Interface Properties and Solar Cell Performance. *Appl. Sci.* **2020**, *10* (3), 1052. https://doi.org/10.3390/app10031052.

(40) Soni, P.; Raghuwanshi, M.; Wuerz, R.; Berghoff, B.; Knoch, J.; Raabe, D.; Cojocaru-Mirédin, O. Sputtering as a Viable Route for In$_2$S$_3$ Buffer Layer Deposition in High Efficiency Cu(In,Ga)Se$_2$ Solar Cells. *Energy Sci. Eng.* **2019**, *7* (2), 478–487. https://doi.org/10.1002/ese3.295.

(41) Hauschild, D.; Mezher, M.; Schnabel, T.; Spiering, S.; Kogler, W.; Carter, J.; Blum, M.; Yang, W.; Ahlswede, E.; Heske, C.; Weinhardt, L. Intermixing at the In$_x$S$_y$/Cu$_2$ZnSn(S,Se)$_4$ Heterojunction and Its Impact on the Chemical and Electronic Interface Structure. *ACS Appl. Energy Mater.* **2019**, *2* (6), 4098–4104. https://doi.org/10.1021/acsaem.9b00263.

(42) Yousfi, E. B.; Asikainen, T.; Pietu, V.; Cowache, P.; Powalla, M.; Lincot, D. Cadmium-Free Buffer Layers Deposited by Atomic Later Epitaxy for Copper Indium Diselenide Solar Cells. *Thin Solid Films* **2000**, *361–362*, 183–186. https://doi.org/10.1016/S0040-6090(99)00860-3.

(43) Nakamura, M.; Yamaguchi, K.; Kimoto, Y.; Yasaki, Y.; Kato, T.; Sugimoto, H. Cd-Free Cu(In,Ga)(Se,S)$_2$ Thin-Film Solar Cell With Record Efficiency of 23.35%. *IEEE J. Photovolt.* **2019**, *9* (6), 1863–1867. https://doi.org/10.1109/JPHOTOV.2019.2937218.

(44) Mezher, M.; Garris, R.; Mansfield, L. M.; Blum, M.; Hauschild, D.; Horsley, K.; Duncan, D. A.; Yang, W.; Bär, M.; Weinhardt, L.; Ramanathan, K.; Heske, C. Soft X-Ray Spectroscopy of a Complex Heterojunction in High-Efficiency Thin-Film Photovoltaics: Intermixing and Zn Speciation at the Zn(O,S)/Cu(In,Ga)Se$_2$ Interface. *ACS Appl. Mater. Interfaces* **2016**, *8* (48), 33256–33263. https://doi.org/10.1021/acsami.6b09245.

(45) Minemoto, T.; Hashimoto, Y.; Satoh, T.; Negami, T.; Takakura, H.; Hamakawa, Y. Cu(In,Ga)Se$_2$ Solar Cells with Controlled Conduction Band Offset of Window/Cu(In,Ga)Se$_2$ Layers. *J. Appl. Phys.* **2001**, *89* (12), 8327–8330. https://doi.org/10.1063/1.1366655.

(46) Nishimura, T.; Chantana, J.; Kawano, Y.; Yamada, A.; Kimoto, Y.; Kato, T.; Sugimoto, H.; Minemoto, T. Interfacial Modification Mechanism by Aging Effect for High-Performance Cd-Free and All-Dry Process Cu(In,Ga)(S,Se)$_2$ Solar Cells. *Appl. Phys. Lett.* **2020**, *117* (22), 223501. https://doi.org/10.1063/5.0031241.

(47) Erfurth, F.; Hußmann, B.; Schöll, A.; Reinert, F.; Grimm, A.; Lauermann, I.; Bär, M.; Niesen, Th.; Palm, J.; Visbeck, S.; Weinhardt, L.; Umbach, E. Chemical Structure of the $(Zn_{1-x}Mg_x)O/CuIn(S,Se)_2$ Interface in Thin Film Solar Cells. *Appl. Phys. Lett.* **2009**, *95* (12), 122104. https://doi.org/10.1063/1.3230071.

(48) Salomé, P. M. P.; Keller, J.; Törndahl, T.; Teixeira, J. P.; Nicoara, N.; Andrade, R.-R.; Stroppa, D. G.; González, J. C.; Edoff, M.; Leitão, J. P.; Sadewasser, S. CdS and $Zn_{1-x}Sn_xO_y$ Buffer Layers for CIGS Solar Cells. *Sol. Energy Mater. Sol. Cells* **2017**, *159*, 272–281. https://doi.org/10.1016/j.solmat.2016.09.023.

(49) Lindahl, J.; Wätjen, J. T.; Hultqvist, A.; Ericson, T.; Edoff, M.; Törndahl, T. The Effect of $Zn_{1-x}Sn_xO_y$ Buffer Layer Thickness in 18.0% Efficient Cd-Free Cu(In,Ga)Se$_2$ Solar Cells. *Prog. Photovolt. Res. Appl.* **2013**, *21* (8), 1588–1597. https://doi.org/10.1002/pip.2239.

(50) Löckinger, J.; Nishiwaki, S.; Bissig, B.; Degutis, G.; Romanyuk, Y. E.; Buecheler, S.; Tiwari, A. N. The Use of HfO$_2$ in a Point Contact Concept for Front Interface Passivation of Cu(In,Ga)Se$_2$ Solar Cells. *Sol. Energy Mater. Sol. Cells* **2019**, *195*, 213–219. https://doi.org/10.1016/j.solmat.2019.03.009.

(51) Kotipalli, R.; Vermang, B.; Joel, J.; Rajkumar, R.; Edoff, M.; Flandre, D. Investigating the Electronic Properties of Al$_2$O$_3$/Cu(In,Ga)Se$_2$ Interface. *AIP Adv.* **2015**, *5* (10), 107101. https://doi.org/10.1063/1.4932512.

(52) Werner, F.; Veith-Wolf, B.; Spindler, C.; Barget, M. R.; Babbe, F.; Guillot, J.; Schmidt, J.; Siebentritt, S. Oxidation as Key Mechanism for Efficient Interface Passivation in Cu(In,Ga)Se$_2$ Thin-Film Solar Cells. *Phys. Rev. Appl.* **2020**, *13* (5), 054004. https://doi.org/10.1103/PhysRevApplied.13.054004.

(53) Koida, T.; Kamikawa-Shimizu, Y.; Yamada, A.; Shibata, H.; Niki, S. Cu(In,Ga)Se$_2$ Solar Cells With Amorphous Oxide Semiconducting Buffer Layers. *IEEE J. Photovolt.* **2015**, *5* (3), 956–961. https://doi.org/10.1109/JPHOTOV.2015.2396356.

(54) Heinemann, M. D.; van Hest, M. F. a. M.; Contreras, M.; Perkins, J. D.; Zakutayev, A.; Kaufmann, C. A.; Unold, T.; Ginley, D. S.; Berry, J. J. Amorphous Oxides as Electron Transport Layers in Cu(In,Ga)Se$_2$ Superstrate Devices. *Phys. Status Solidi A* **2017**, *214* (5), 1600870. https://doi.org/10.1002/pssa.201600870.

(55) Larsson, F.; Keller, J.; Olsson, J.; Donzel-Gargand, O.; Martin, N. M.; Edoff, M.; Törndahl, T. Amorphous Tin-Gallium Oxide Buffer Layers in (Ag,Cu)(In,Ga)Se$_2$ Solar Cells. *Sol. Energy Mater. Sol. Cells* **2020**, *215*, 110647. https://doi.org/10.1016/j.solmat.2020.110647.

(56) Kumar, S. S.; Rubio, E. J.; Noor-A-Alam, M.; Martinez, G.; Manandhar, S.; Shutthanandan, V.; Thevuthasan, S.; Ramana, C. V. Structure, Morphology, and Optical Properties of Amorphous and Nanocrystalline Gallium Oxide Thin Films. *J. Phys. Chem. C* **2013**, *117* (8), 4194–4200. https://doi.org/10.1021/jp311300e.

(57) Swallow, J. E. N.; Vorwerk, C.; Mazzolini, P.; Vogt, P.; Bierwagen, O.; Karg, A.; Eickhoff, M.; Schörmann, J.; Wagner, M. R.; Roberts, J. W.; Chalker, P. R.; Smiles, M. J.; Murgatroyd, P.; Razek, S. A.; Lebens-Higgins, Z. W.; Piper, L. F. J.; Jones, L. A. H.; Thakur, P. K.; Lee, T.-L.; Varley, J. B.; Furthmüller, J.; Draxl, C.; Veal, T. D.; Regoutz, A. Influence of Polymorphism on the Electronic Structure of Ga$_2$O$_3$. *Chem. Mater.* **2020**, *32* (19), 8460–8470. https://doi.org/10.1021/acs.chemmater.0c02465.

(58) Swallow, J. E. N.; Varley, J. B.; Jones, L. A. H.; Gibbon, J. T.; Piper, L. F. J.; Dhanak, V. R.; Veal, T. D. Transition from Electron Accumulation to Depletion at β-Ga$_2$O$_3$ Surfaces: The Role of Hydrogen

and the Charge Neutrality Level. *APL Mater.* **2019**, *7* (2), 022528. https://doi.org/10.1063/1.5054091.

(59) Navarro-Quezada, A.; Galazka, Z.; Alamé, S.; Skuridina, D.; Vogt, P.; Esser, N. Surface Properties of Annealed Semiconducting β-Ga_2O_3 (100) Single Crystals for Epitaxy. *Appl. Surf. Sci.* **2015**, *349*, 368–373. https://doi.org/10.1016/j.apsusc.2015.04.225.

(60) Navarro-Quezada, A.; Alamé, S.; Esser, N.; Furthmüller, J.; Bechstedt, F.; Galazka, Z.; Skuridina, D.; Vogt, P. Near Valence-Band Electronic Properties of Semiconducting β-Ga_2O_3 (100) Single Crystals. *Phys. Rev. B* **2015**, *92* (19), 195306. https://doi.org/10.1103/PhysRevB.92.195306.

(61) Yang, J.; Sparks, Z.; Ren, F.; Pearton, S. J.; Tadjer, M. Effect of Surface Treatments on Electrical Properties of β-Ga_2O_3. *J. Vac. Sci. Technol. B Nanotechnol. Microelectron. Mater. Process. Meas. Phenom.* **2018**, *36* (6), 061201. https://doi.org/10.1116/1.5052229.

(62) Weinhardt, L.; Steininger, R.; Kreikemeyer-Lorenzo, D.; Mangold, S.; Hauschild, D.; Batchelor, D.; Spangenberg, T.; Heske, C. X-SPEC: A 70 eV to 15 keV Undulator Beamline for X-Ray and Electron Spectroscopies. *J. Synchrotron Radiat.* **2021**, *28* (2), 609–617. https://doi.org/10.1107/S1600577520016318.

(63) Vinson, J. Advances in the OCEAN -3 Spectroscopy Package. *Phys. Chem. Chem. Phys.* **2022**, *24* (21), 12787–12803. https://doi.org/10.1039/D2CP01030E.

(64) Siegbahn, K.; Edvarson, K. β-RAY SPECTROSCOPY IN THE PRECISION RANGE OF 1 : 10 s. *Nucl. Phys. 1* **1956**. https://doi.org/10.1016/S0029-5582(56)80022-9.

(65) Siegbahn, K. *ESCA Atomic, Molecular and Solid State Structure Studies by Means of Electron Spectroscopy*; Almqvist & Wiksell: Uppsala, 1967.

(66) Siegbahn, K. Electron Spectroscopy - an Outlook. *J. Electron Spectrosc. Relat. Phenom.* **1974**, *5* (1), 3–97. https://doi.org/10.1016/0368-2048(74)85005-X.

(67) *The Nobel Prize in Physics 1981*. NobelPrize.org. https://www.nobelprize.org/prizes/physics/1981/siegbahn/lecture/?iframe=true&width=100%25 &height=100%25 (accessed 2023-09-08).

(68) Winter, B. Liquid Microjet for Photoelectron Spectroscopy. *Nucl. Instrum. Methods Phys. Res. Sect. Accel. Spectrometers Detect. Assoc. Equip.* **2009**, *601* (1–2), 139–150. https://doi.org/10.1016/j.nima.2008.12.108.

(69) Hüfner, S. *Photoelectron Spectroscopy: Principles and Applications*, 3rd ed.; Springer: Berlin; New York, 2003.

(70) Briggs, D.; Seah, M. P. *Practical Surface Analysis by Auger and X-Ray Photoelectron Spectroscopy*; John Wiley & Sons Ltd., 1983.

(71) Fermi, E. *Nuclear Physics*; Universty of Chicago Press, 1950.

(72) Seah, M. P.; Anthony, M. T. Quantitative XPS: The Calibration of Spectrometer Intensity—Energy Response Functions. 1—The Establishment of Reference Procedures and Instrument Behaviour. *Surf. Interface Anal.* **1984**, *6* (5), 230–241. https://doi.org/10.1002/sia.740060506.

(73) Seah, M. P.; Dench, W. A. Quantitative Electron Spectroscopy of Surfaces: A Standard Data Base for Electron Inelastic Mean Free Paths in Solids. *Surf. Interface Anal.* **1979**, *1* (1), 2–11. https://doi.org/10.1002/sia.740010103.

(74) Wojdyr, M. Fityk: A General-Purpose Peak Fitting Program. *J. Appl. Crystallogr.* **2010**, *43* (5), 1126–1128. https://doi.org/10.1107/S0021889810030499.

(75) Krause, M. O. Atomic Radiative and Radiationless Yields for *K* and *L* Shells. *J. Phys. Chem. Ref. Data* **1979**, *8* (2), 307–327. https://doi.org/10.1063/1.555594.

(76) *NIST X-ray Photoelectron Spectroscopy (XPS) Database Main Search Menu*. https://srdata.nist.gov/xps/main_search_menu.aspx (accessed 2022-04-07).

(77) Wagner, C. D. Auger Lines in X-Ray Photoelectron Spectrometry. *Anal. Chem.* **1972**, *44* (6), 967–973. https://doi.org/10.1021/ac60314a015.

(78) Dolbilkin, B. S.; Ratner, B. S. V I Veksler and the Development of Nuclear Physics in the Soviet Union. *Phys.-Uspekhi* **2007**, *50* (8), 853. https://doi.org/10.1070/PU2007v050n08ABEH006357.

(79) Author. *KIT - IBPT - Discover - Test Facilities - KARA*. https://www.ibpt.kit.edu/kara.php (accessed 2023-08-31).

(80) *MERIL*. https://portal.meril.eu/meril/view/facilitys/15648# (accessed 2023-08-31).

(81) Gilmore, K.; Kas, J. J.; Liang, Y.; Pemmaraju, D.; Prendergast, D.; Rehr, J.; Shirley, E. L.; Vila, F.; Vinson, J. *User's Guide, OCEAN Version 2.0*; 2017.

(82) *CXRO X-Ray Interactions With Matter*. https://henke.lbl.gov/optical_constants/ (accessed 2023-08-31).

(83) Ma, Y. X-Ray Absorption, Emission, and Resonant Inelastic Scattering in Solids. *Phys. Rev. B* **1994**, *49* (9), 5799–5805. https://doi.org/10.1103/PhysRevB.49.5799.

(84) Ma, Y.; Wassdahl, N.; Skytt, P.; Guo, J.; Nordgren, J.; Johnson, P. D.; Rubensson, J.-E.; Boske, T.; Eberhardt, W.; Kevan, S. D. Soft-x-Ray Resonant Inelastic Scattering at the C *K* Edge of Diamond. *Phys. Rev. Lett.* **1992**, *69* (17), 2598–2601. https://doi.org/10.1103/PhysRevLett.69.2598.

(85) Sakurai, J. J. *Advanced Quantum Mechanics*; Addison Wesley: Menlo Park, California, 1967.

(86) Kramers, H. A.; Heisenberg, W. Über die Streuung von Strahlung durch Atome. *Z. Für Phys.* **1925**, *31* (1), 681–708. https://doi.org/10.1007/BF02980624.

(87) Weisskopf, V.; Wigner, E. Berechnung der natürlichen Linienbreite auf Grund der Diracschen Lichttheorie. *Z. Für Phys.* **1930**, *63* (1), 54–73. https://doi.org/10.1007/BF01336768.

(88) Fuchs, O. Soft X-Ray Spectroscopy of Organic Molecules and Liquids, Julius-Maximilians-Universität Würtzburg, Würtzburg, Germany, 2009.

(89) Weinhardt, L.; Fuchs, O.; Blum, M.; Bär, M.; Weigand, M.; Denlinger, J. D.; Zubavichus, Y.; Zharnikov, M.; Grunze, M.; Heske, C.; Umbach, E. Resonant X-Ray Emission Spectroscopy of Liquid Water: Novel Instrumentation, High Resolution, and the "Map" Approach. *J. Electron Spectrosc. Relat. Phenom.* **2010**, *177* (2–3), 206–211. https://doi.org/10.1016/j.elspec.2009.02.014.

(90) Cottenier, S. Density Functional Theory and the Family of (L)APW-Methods: A Step-by-Step Introduction.

(91) Scholl, D.; Steckel, J. *Density Functional Theory: A Practical Introduction*; Wiley, 2009.

(92) Slater, J. C. A Simplification of the Hartree-Fock Method. *Phys. Rev.* **1951**, *81* (3), 385–390. https://doi.org/10.1103/PhysRev.81.385.

(93) Hohenberg, P.; Kohn, W. Inhomogeneous Electron Gas. *Phys. Rev.* **1964**, *136* (3B), B864–B871. https://doi.org/10.1103/PhysRev.136.B864.

(94) Kohn, W.; Sham, L. J. Self-Consistent Equations Including Exchange and Correlation Effects. *Phys. Rev.* **1965**, *140* (4A), A1133–A1138. https://doi.org/10.1103/PhysRev.140.A1133.

(95) Vinson, J. Bethe-Salpeter Equation Approach for Calculations of X-Ray Spectra, University of Washington, Washington, USA, 2012.

(96) Perdew, J. P.; Burke, K.; Ernzerhof, M. Generalized Gradient Approximation Made Simple. *Phys. Rev. Lett.* **1996**, *77* (18), 3865–3868. https://doi.org/10.1103/PhysRevLett.77.3865.

(97) *--Opium-- Pseudopotential generation project*. https://opium.sourceforge.net/ (accessed 2023-09-15).

(98) Kotochigova, S.; Levine, Z. H.; Shirley, E. L.; Stiles, M. D.; Clark, C. W. Local-Density-Functional Calculations of the Energy of Atoms. *Phys. Rev. A* **1997**, *55* (1), 191–199. https://doi.org/10.1103/PhysRevA.55.191.

(99) Shirley, E. L. Ti 1s Pre-Edge Features in Rutile: A Bethe-Salpeter Calculation. *J. Electron Spectrosc. Relat. Phenom.* **2004**, *136* (1–2), 77–83. https://doi.org/10.1016/j.elspec.2004.02.134.

(100) Blöchl, P. E. Projector Augmented-Wave Method. *Phys. Rev. B* **1994**, *50* (24), 17953–17979. https://doi.org/10.1103/PhysRevB.50.17953.

(101) Schwarz, D. K. An Augmented Plane Wave + Local Orbitals Program for Calculating Crystal Properties.

(102) Mahan, G. D. Final-State Potential in x-Ray Spectra. *Phys. Rev. B* **1980**, *21* (4), 1421–1431. https://doi.org/10.1103/PhysRevB.21.1421.

(103) Grebennikov, V. I.; Babanov, Yu. A.; Sokolov, O. B. Extra-Atomic Relaxation and X-Ray Spectra of Narrow-Band Metals. I. Formalism. *Phys. Status Solidi B* **1977**, *79* (2), 423–432. https://doi.org/10.1002/pssb.2220790204.

(104) Von Barth, U.; Grossmann, G. Dynamical Effects in X-Ray Spectra and the Final-State Rule. *Phys. Rev. B* **1982**, *25* (8), 5150–5179. https://doi.org/10.1103/PhysRevB.25.5150.

(105) Weinhardt, L.; Hauschild, D.; Steininger, R.; Jiang, N.; Blum, M.; Yang, W.; Heske, C. Sulfate Speciation Analysis Using Soft X-Ray Emission Spectroscopy. *Anal. Chem.* **2021**, *93* (23), 8300–8308. https://doi.org/10.1021/acs.analchem.1c01187.

(106) Weinhardt, L.; Hauschild, D.; Fuchs, O.; Steininger, R.; Jiang, N.; Blum, M.; Denlinger, J. D.; Yang, W.; Umbach, E.; Heske, C. Satellite-Dominated Sulfur $L_{2,3}$ X-Ray Emission of Alkaline Earth Metal Sulfides. *ACS Omega* **2023**, *8* (5), 4921–4927. https://doi.org/10.1021/acsomega.2c07228.

(107) Salpeter, E. E.; Bethe, H. A. A Relativistic Equation for Bound-State Problems. *Phys. Rev.* **1951**, *84* (6), 1232–1242. https://doi.org/10.1103/PhysRev.84.1232.

(108) Vinson, J.; Rehr, J. J.; Kas, J. J.; Shirley, E. L. Bethe-Salpeter Equation Calculations of Core Excitation Spectra. *Phys. Rev. B* **2011**, *83* (11), 115106. https://doi.org/10.1103/PhysRevB.83.115106.

(109) Sander, T.; Maggio, E.; Kresse, G. Beyond the Tamm-Dancoff Approximation for Extended Systems Using Exact Diagonalization. *Phys. Rev. B* **2015**, *92* (4), 045209. https://doi.org/10.1103/PhysRevB.92.045209.

(110) Gilmore, K.; Vinson, J.; Shirley, E. L.; Prendergast, D.; Pemmaraju, C. D.; Kas, J. J.; Vila, F. D.; Rehr, J. J. Efficient Implementation of Core-Excitation Bethe–Salpeter Equation Calculations. *Comput. Phys. Commun.* **2015**, *197*, 109–117. https://doi.org/10.1016/j.cpc.2015.08.014.

(111) Kim, S.; Hoang, V. Q.; Bark, C. W. Silicon-Based Technologies for Flexible Photovoltaic (PV) Devices: From Basic Mechanism to Manufacturing Technologies. *Nanomaterials* **2021**, *11* (11), 2944. https://doi.org/10.3390/nano11112944.

(112) *Best Research-Cell Efficiency Chart*. https://www.nrel.gov/pv/cell-efficiency.html (accessed 2023-09-08).

(113) Carlson, D. E.; Wronski, C. R. Amorphous Silicon Solar Cell. *Appl. Phys. Lett.* **1976**, *28* (11), 671–673. https://doi.org/10.1063/1.88617.

(114) Bonnet, D.; Rabenhorst, H. New Results on the Development of a Thin Film P-CdTe-n-CdS Heterojunction Solar Cell. In *Proceedings of the 9th Photovoltaic Specialists Conference*; Silver Spring, MD, USA, 1972; pp 129–131.

(115) Shay, J. L.; Wagner, S.; Kasper, H. M. Efficient CuInSe₂/CdS Solar Cells. *Appl. Phys. Lett.* **1975**, *27* (2), 89–90. https://doi.org/10.1063/1.88372.

(116) Wei, S.-H.; Zunger, A. Band Offsets and Optical Bowings of Chalcopyrites and Zn-Based II-VI Alloys. *J. Appl. Phys.* **1995**, *78* (6), 3846–3856. https://doi.org/10.1063/1.359901.

(117) Rife, J. C. - Copper Gallium Sulfide (CuGaS₂). In *Handbook of Optical Constants of Solids*; Palik, E. D., Ed.; Academic Press: Burlington, 1997; pp 459–471. https://doi.org/10.1016/B978-012544415-6.50112-6.

(118) Mansfield, L. *Copper Indium Gallium Diselenide Solar Cells*. https://www.nrel.gov/pv/copper-indium-gallium-diselenide-solar-cells.html (accessed 2023-09-08).

(119) Hedström, J.; Ohlsen, H.; Bodegard, M.; Kylner, A.; Stolt, L.; Hariskos, D.; Ruckh, M.; Schock, H.-W. ZnO/CdS/Cu(In,Ga)Se₂ Thin Film Solar Cells with Improved Performance. In *Conference Record of*

the Twenty Third IEEE Photovoltaic Specialists Conference - 1993 (Cat. No.93CH3283-9); 1993; pp 364–371. https://doi.org/10.1109/PVSC.1993.347154.

(120) Chirilă, A.; Reinhard, P.; Pianezzi, F.; Bloesch, P.; Uhl, A. R.; Fella, C.; Kranz, L.; Keller, D.; Gretener, C.; Hagendorfer, H.; Jaeger, D.; Erni, R.; Nishiwaki, S.; Buecheler, S.; Tiwari, A. N. Potassium-Induced Surface Modification of Cu(In,Ga)Se$_2$ Thin Films for High-Efficiency Solar Cells. *Nat. Mater.* **2013**, *12* (12), 1107–1111. https://doi.org/10.1038/nmat3789.

(121) Jackson, P.; Wuerz, R.; Hariskos, D.; Lotter, E.; Witte, W.; Powalla, M. Effects of Heavy Alkali Elements in Cu(In,Ga)Se$_2$ Solar Cells with Efficiencies up to 22.6%. *Phys. Status Solidi RRL – Rapid Res. Lett.* **2016**, *10* (8), 583–586. https://doi.org/10.1002/pssr.201600199.

(122) Hynes, K. M.; Newham, J. A Comparison of Window/Buffer Layer Materials for CdTe Thin Film Modules Using Environmental Risk Assessment. In *Conference Record of the Twenty-Eighth IEEE Photovoltaic Specialists Conference - 2000 (Cat. No.00CH37036)*; 2000; pp 1513–1516. https://doi.org/10.1109/PVSC.2000.916182.

(123) Hariskos, D.; Spiering, S.; Powalla, M. Buffer Layers in Cu(In,Ga)Se$_2$ Solar Cells and Modules. *Thin Solid Films* **2005**, *480–481*, 99–109. https://doi.org/10.1016/j.tsf.2004.11.118.

(124) *New world record for CIGS efficiency*. Avancis. https://www.avancis.de/en/magazine/pr-efficiency (accessed 2022-11-03).

(125) Roy, R.; Hill, V. G.; Osborn, E. F. Polymorphism of Ga$_2$O$_3$ and the System Ga$_2$O$_3$-H$_2$O. **1952**, *74*.

(126) Geller, S. Crystal Structure of β-Ga$_2$O$_3$. *J. Chem. Phys.* **1960**, *33* (3), 676–684. https://doi.org/10.1063/1.1731237.

(127) Åhman, J.; Svensson, G.; Albertsson, J. A Reinvestigation of β-Gallium Oxide. *Acta Crystallogr. Sect. C* **1996**, *52* (6), 1336–1338. https://doi.org/10.1107/S0108270195016404.

(128) Peelaers, H.; Van de Walle, C. G. Brillouin Zone and Band Structure of β-Ga$_2$O$_3$. *Phys. Status Solidi B* **2015**, *252* (4), 828–832. https://doi.org/10.1002/pssb.201451551.

(129) Cocchi, C.; Zschiesche, H.; Nabok, D.; Mogilatenko, A.; Albrecht, M.; Galazka, Z.; Kirmse, H.; Draxl, C.; Koch, C. T. Atomic Signatures of Local Environment from Core-Level Spectroscopy in β-Ga$_2$O$_3$. *Phys. Rev. B* **2016**, *94* (7), 075147. https://doi.org/10.1103/PhysRevB.94.075147.

(130) Momma, K.; Izumi, F. VESTA 3 for Three-Dimensional Visualization of Crystal, Volumetric and Morphology Data. *J. Appl. Crystallogr.* **2011**, *44* (6), 1272–1276. https://doi.org/10.1107/S0021889811038970.

(131) Wei, S.-H.; Zunger, A. Role of Metal *d* States in II-VI Semiconductors. *Phys. Rev. B* **1988**, *37* (15), 8958–8981. https://doi.org/10.1103/PhysRevB.37.8958.

(132) Mengle, K. A.; Shi, G.; Bayerl, D.; Kioupakis, E. First-Principles Calculations of the near-Edge Optical Properties of β-Ga$_2$O$_3$. *Appl. Phys. Lett.* **2016**, *109* (21), 212104. https://doi.org/10.1063/1.4968822.

(133) Crowley, J. M.; Tahir-Kheli, J.; Goddard, W. A. I. Resolution of the Band Gap Prediction Problem for Materials Design. *J. Phys. Chem. Lett.* **2016**, *7* (7), 1198–1203. https://doi.org/10.1021/acs.jpclett.5b02870.

(134) Yeh, J. J.; Lindau, I. Atomic Subshell Photoionization Cross Sections and Asymmetry Parameters: 1 ⩽ Z ⩽ 103. *At. Data Nucl. Data Tables* **1985**, *32* (1), 1–155. https://doi.org/10.1016/0092-640X(85)90016-6.

(135) Hunt, A. Understanding the Electronic Structure of LiFePO$_4$ and FePO$_4$. Doctoral Thesis, University of Saskatchewan, Saskatoon, 2007.

(136) Blum, M.; Weinhardt, L.; Fuchs, O.; Bär, M.; Zhang, Y.; Weigand, M.; Krause, S.; Pookpanratana, S.; Hofmann, T.; Yang, W.; Denlinger, J. D.; Umbach, E.; Heske, C. Solid and Liquid Spectroscopic Analysis (SALSA)–a Soft x-Ray Spectroscopy Endstation with a Novel Flow-through Liquid Cell. *Rev. Sci. Instrum.* **2009**, *80* (12), 123102. https://doi.org/10.1063/1.3257926.

(137) Fuchs, O.; Weinhardt, L.; Blum, M.; Weigand, M.; Umbach, E.; Bär, M.; Heske, C.; Denlinger, J.; Chuang, Y.-D.; McKinney, W.; Hussain, Z.; Gullikson, E.; Jones, M.; Batson, P.; Nelles, B.; Follath, R. High-Resolution, High-Transmission Soft x-Ray Spectrometer for the Study of Biological Samples. *Rev. Sci. Instrum.* **2009**, *80* (6), 063103. https://doi.org/10.1063/1.3133704.

(138) Scofield, J. H.; Asher, S.; Albin, D.; Tuttle, J.; Contreras, M.; Niles, D.; Reedy, R.; Tennant, A.; Noufi, R. Sodium Diffusion, Selenization, and Microstructural Effects Associated with Various Molybdenum Back Contact Layers for CIS-Based Solar Cells. In *Proceedings of 1994 IEEE 1st World Conference on Photovoltaic Energy Conversion - WCPEC (A Joint Conference of PVSC, PVSEC and PSEC)*; IEEE: Waikoloa, HI, USA, 1994; Vol. 1, pp 164–167. https://doi.org/10.1109/WCPEC.1994.519833.

(139) Heske, C.; Fink, R.; Umbach, E.; Riedl, W.; Karg, F. Na-induced Effects on the Electronic Structure and Composition of Cu(In,Ga)Se$_2$ Thin-film Surfaces. *Appl. Phys. Lett.* **1996**, *68* (24), 3431–3433. https://doi.org/10.1063/1.115783.

(140) Niles, D. W.; Al-Jassim, M.; Ramanathan, K. Direct Observation of Na and O Impurities at Grain Surfaces of CuInSe$_2$ Thin Films. *J. Vac. Sci. Technol. Vac. Surf. Films* **1999**, *17* (1), 291–296. https://doi.org/10.1116/1.581583.

(141) Rockett, A.; Granath, K.; Asher, S.; Al Jassim, M. M.; Hasoon, F.; Matson, R.; Basol, B.; Kapur, V.; Britt, J. S.; Gillespie, T.; Marshall, C. Na Incorporation in Mo and CuInSe$_2$ from Production Processes. *Sol. Energy Mater. Sol. Cells* **1999**, *59* (3), 255–264. https://doi.org/10.1016/S0927-0248(99)00026-4.

(142) Handick, E.; Reinhard, P.; Wilks, R. G.; Pianezzi, F.; Kunze, T.; Kreikemeyer-Lorenzo, D.; Weinhardt, L.; Blum, M.; Yang, W.; Gorgoi, M.; Ikenaga, E.; Gerlach, D.; Ueda, S.; Yamashita, Y.; Chikyow, T.; Heske, C.; Buecheler, S.; Tiwari, A. N.; Bär, M. Formation of a K—In—Se Surface Species by NaF/KF Postdeposition Treatment of Cu(In,Ga)Se$_2$ Thin-Film Solar Cell Absorbers. *ACS Appl. Mater. Interfaces* **2017**, *9* (4), 3581–3589. https://doi.org/10.1021/acsami.6b11892.

(143) Keller, J.; Aboulfadl, H.; Stolt, L.; Donzel-Gargand, O.; Edoff, M. Rubidium Fluoride Absorber Treatment for Wide-Gap (Ag,Cu)(In,Ga)Se$_2$ Solar Cells. *Sol. RRL* **2022**, *6* (6), 2200044. https://doi.org/10.1002/solr.202200044.

(144) Reinhard, P.; Bissig, B.; Pianezzi, F.; Hagendorfer, H.; Sozzi, G.; Menozzi, R.; Gretener, C.; Nishiwaki, S.; Buecheler, S.; Tiwari, A. N. Alkali-Templated Surface Nanopatterning of Chalcogenide Thin Films: A Novel Approach Toward Solar Cells with Enhanced Efficiency. *Nano Lett.* **2015**, *15* (5), 3334–3340. https://doi.org/10.1021/acs.nanolett.5b00584.

(145) Erfurth, Felix. Elektronenspektroskopie an Cd-Freien Pufferschichten Und Deren Grenzflächen in Cu(In,Ga)(S,Se)$_2$. Doctoral Thesis, Universität Würzburg, 2010.

(146) Kylner, A. The Chemical Bath Deposited CdS/Cu(In,Ga)Se$_2$ Interface as Revealed by X-Ray Photoelectron Spectroscopy. *J. Electrochem. Soc.* **1999**, *146* (5), 1816. https://doi.org/10.1149/1.1391849.

(147) Weinhardt, L.; Fuchs, O.; Groß, D.; Umbach, E.; Heske, C.; Dhere, N. G.; Kadam, A. A.; Kulkarni, S. S. Surface Modifications of Cu(In,Ga)S$_2$ Thin Film Solar Cell Absorbers by KCN and H$_2$O$_2$∕H$_2$SO$_4$ Treatments. *J. Appl. Phys.* **2006**, *100* (2), 024907. https://doi.org/10.1063/1.2216367.

(148) Jackson, P.; Hariskos, D.; Wuerz, R.; Kiowski, O.; Bauer, A.; Friedlmeier, T. M.; Powalla, M. Properties of Cu(In,Ga)Se$_2$ Solar Cells with New Record Efficiencies up to 21.7%. *Phys. Status Solidi RRL – Rapid Res. Lett.* **2015**, *9* (1), 28–31. https://doi.org/10.1002/pssr.201409520.

(149) Ramanathan, K.; Contreras, M. A.; Perkins, C. L.; Asher, S.; Hasoon, F. S.; Keane, J.; Young, D.; Romero, M.; Metzger, W.; Noufi, R.; Ward, J.; Duda, A. Properties of 19.2% Efficiency ZnO/CdS/Cu(In,Ga)Se$_2$ Thin-Film Solar Cells. *Prog. Photovolt. Res. Appl.* **2003**, *11* (4), 225–230. https://doi.org/10.1002/pip.494.

(150) Kessler, J.; Wennerberg, J.; Bodegård, M.; Stolt, L. Highly Efficient Cu(In,Ga)Se$_2$ Mini-Modules. *Sol. Energy Mater. Sol. Cells* **2003**, *75* (1), 35–46. https://doi.org/10.1016/S0927-0248(02)00102-2.

(151) Gutzler, R.; Witte, W.; Kanevce, A.; Hariskos, D.; Paetel, S. V$_{OC}$-Losses across the Band Gap: Insights from a High-Throughput Inline Process for CIGS Solar Cells. *Prog. Photovolt. Res. Appl.* **2023**, *n/a* (n/a), 1–9. https://doi.org/10.1002/pip.3707.

(152) Moulder, John F.; Stickle, William F.; Sobol, Peter E.; Bomben, Kenneth D. *Handbook of X-Ray Photoelectron Spectroscopy: A Reference Book of Standard Spectra for Identification and Interpretation of XPS Data*; Perkin Elmer Cooperation: Minnesota, USA, 1992.

(153) Seah, M. P. Post-1989 Calibration Energies for X-Ray Photoelectron Spectrometers and the 1990 Josephson Constant. *Surf. Interface Anal.* **1989**, *14* (8), 488–488. https://doi.org/10.1002/sia.740140813.

(154) Tanuma, S.; Powell, C. J.; Penn, D. R. Calculations of Electorn Inelastic Mean Free Paths. II. Data for 27 Elements over the 50–2000 eV Range. *Surf. Interface Anal.* **1991**, *17* (13), 911–926. https://doi.org/10.1002/sia.740171304.

(155) Tanuma, S.; Powell, C. J.; Penn, D. R. Calculations of Electron Inelastic Mean Free Paths. V. Data for 14 Organic Compounds over the 50–2000 eV Range. *Surf. Interface Anal.* **1994**, *21* (3), 165–176. https://doi.org/10.1002/sia.740210302.

(156) Kreikemeyer-Lorenzo, D.; Hauschild, D.; Jackson, P.; Friedlmeier, T. M.; Hariskos, D.; Blum, M.; Yang, W.; Reinert, F.; Powalla, M.; Heske, C.; Weinhardt, L. Rubidium Fluoride Post-Deposition Treatment: Impact on the Chemical Structure of the Cu(In,Ga)Se$_2$ Surface and CdS/Cu(In,Ga)Se$_2$ Interface in Thin-Film Solar Cells. *ACS Appl. Mater. Interfaces* **2018**, *10* (43), 37602–37608. https://doi.org/10.1021/acsami.8b10005.

(157) Bourque, J. L.; Biesinger, M. C.; Baines, K. M. Chemical State Determination of Molecular Gallium Compounds Using XPS. *Dalton Trans.* **2016**, *45* (18), 7678–7696. https://doi.org/10.1039/C6DT00771F.

(158) Bär, M.; Repins, I.; Contreras, M. A.; Weinhardt, L.; Noufi, R.; Heske, C. Chemical and Electronic Surface Structure of 20%-Efficient Cu(In,Ga)Se$_2$ Thin Film Solar Cell Absorbers. *Appl. Phys. Lett.* **2009**, *95* (5), 052106. https://doi.org/10.1063/1.3194153.

(159) Bombsch, J.; Avancini, E.; Carron, R.; Handick, E.; Garcia-Diez, R.; Hartmann, C.; Félix, R.; Ueda, S.; Wilks, R. G.; Bär, M. NaF/RbF-Treated Cu(In,Ga)Se$_2$ Thin-Film Solar Cell Absorbers: Distinct Surface Modifications Caused by Two Different Types of Rubidium Chemistry. *ACS Appl. Mater. Interfaces* **2020**, *12* (31), 34941–34948. https://doi.org/10.1021/acsami.0c08794.

(160) Maticiuc, N.; Kodalle, T.; Lauche, J.; Wenisch, R.; Bertram, T.; Kaufmann, C. A.; Lauermann, I. In Vacuo XPS Investigation of Cu(In,Ga)Se$_2$ Surface after RbF Post-Deposition Treatment. *Thin Solid Films* **2018**, *665*, 143–147. https://doi.org/10.1016/j.tsf.2018.09.026.

(161) Kim, J.-M.; Yoo, S.-J.; Moon, C.-K.; Sim, B.; Lee, J.-H.; Lim, H.; Kim, J. W.; Kim, J.-J. N-Type Molecular Doping in Organic Semiconductors: Formation and Dissociation Efficiencies of a Charge Transfer Complex. *J. Phys. Chem. C* **2016**, *120* (17), 9475–9481. https://doi.org/10.1021/acs.jpcc.6b01175.

(162) van Maris, V. R.; Hauschild, D.; Niesen, T. P.; Eraerds, P.; Dalibor, T.; Palm, J.; Blum, M.; Yang, W.; Heske, C.; Weinhardt, L. Impact of UV-Induced Ozone and Low-Energy Ar$^+$-Ion Cleaning on the Chemical Structure of Cu(In,Ga)(S,Se)$_2$ Absorber Surfaces. *J. Appl. Phys.* **2020**, *128* (15), 155301. https://doi.org/10.1063/5.0020253.

(163) Zhang, Y.; Yan, J.; Zhao, G.; Xie, W. First-Principles Study on Electronic Structure and Optical Properties of Sn-Doped β-Ga$_2$O$_3$. *Phys. B Condens. Matter* **2010**, *405* (18), 3899–3903. https://doi.org/10.1016/j.physb.2010.06.024.

(164) Víllora, E. G.; Shimamura, K.; Yoshikawa, Y.; Ujiie, T.; Aoki, K. Electrical Conductivity and Carrier Concentration Control in β-Ga$_2$O$_3$ by Si Doping. *Appl. Phys. Lett.* **2008**, *92* (20), 202120. https://doi.org/10.1063/1.2919728.

(165) Du, X.; Li, Z.; Luan, C.; Wang, W.; Wang, M.; Feng, X.; Xiao, H.; Ma, J. Preparation and Characterization of Sn-Doped β-Ga$_2$O$_3$ Homoepitaxial Films by MOCVD. *J. Mater. Sci.* **2015**, *50* (8), 3252–3257. https://doi.org/10.1007/s10853-015-8893-4.

(166) Ahlberg, P.; Johansson, F. O. L.; Zhang, Z.-B.; Jansson, U.; Zhang, S.-L.; Lindblad, A.; Nyberg, T. Defect Formation in Graphene during Low-Energy Ion Bombardment. *APL Mater.* **2016**, *4* (4), 046104. https://doi.org/10.1063/1.4945587.

(167) Gleim, T.; Heske, C.; Umbach, E.; Schumacher, C.; Gundel, S.; Faschinger, W.; Fleszar, A.; Ammon, C.; Probst, M.; Steinrück, H.-P. Formation of the ZnSe/(Te/)GaAs() Heterojunction. *Surf. Sci.* **2003**, *531* (1), 77–85. https://doi.org/10.1016/S0039-6028(03)00439-4.

(168) Aida, H.; Nishiguchi, K.; Takeda, H.; Aota, N.; Sunakawa, K.; Yaguchi, Y. Growth of β-Ga$_2$O$_3$ Single Crystals by the Edge-Defined, Film Fed Growth Method. *Jpn. J. Appl. Phys.* **2008**, *47* (11), 8506–8509. https://doi.org/10.1143/JJAP.47.8506.

(169) Li, G.-L.; Zhang, F.; Cui, Y.-T.; Oji, H.; Son, J.-Y.; Guo, Q. Electronic Structure of β-Ga$_2$O$_3$ Single Crystals Investigated by Hard X-Ray Photoelectron Spectroscopy. *Appl. Phys. Lett.* **2015**, *107* (2), 022109. https://doi.org/10.1063/1.4926919.

(170) Blaha, P.; Schwarz, K.; Tran, F.; Laskowski, R.; Madsen, G. K. H.; Marks, L. D. WIEN2k: An APW+lo Program for Calculating the Properties of Solids. *J. Chem. Phys.* **2020**, *152* (7), 074101. https://doi.org/10.1063/1.5143061.

(171) Bagheri, M.; Blaha, P. DFT Calculations of Energy Dependent XPS Valence Band Spectra. *J. Electron Spectrosc. Relat. Phenom.* **2019**, *230*, 1–9. https://doi.org/10.1016/j.elspec.2018.11.002.

(172) Trzhaskovskaya, M. B.; Nefedov, V. I.; Yarzhemsky, V. G. PHOTOELECTRON ANGULAR DISTRIBUTION PARAMETERS FOR ELEMENTS Z=1 TO Z=54 IN THE PHOTOELECTRON ENERGY RANGE 100–5000 eV. *At. Data Nucl. Data Tables* **2001**, *77* (1), 97–159. https://doi.org/10.1006/adnd.2000.0849.

(173) Trzhaskovskaya, M. B.; Nikulin, V. K.; Nefedov, V. I.; Yarzhemsky, V. G. Non-Dipole Second Order Parameters of the Photoelectron Angular Distribution for Elements Z=1–100 in the Photoelectron Energy Range 1–10keV. *At. Data Nucl. Data Tables* **2006**, *92* (2), 245–304. https://doi.org/10.1016/j.adt.2005.12.002.

(174) Jain, A.; Ong, S. P.; Hautier, G.; Chen, W.; Richards, W. D.; Dacek, S.; Cholia, S.; Gunter, D.; Skinner, D.; Ceder, G.; Persson, K. A. Commentary: The Materials Project: A Materials Genome Approach to Accelerating Materials Innovation. *APL Mater.* **2013**, *1* (1), 011002. https://doi.org/10.1063/1.4812323.

(175) Mohamed, M.; Janowitz, C.; Unger, I.; Manzke, R.; Galazka, Z.; Uecker, R.; Fornari, R.; Weber, J. R.; Varley, J. B.; Van de Walle, C. G. The Electronic Structure of β-Ga$_2$O$_3$. *Appl. Phys. Lett.* **2010**, *97* (21), 211903. https://doi.org/10.1063/1.3521255.

(176) Mohamed, M.; Unger, I.; Janowitz, C.; Manzke, R.; Galazka, Z.; Uecker, R.; Fornari, R. The Surface Band Structure of β-Ga$_2$O$_3$. *J. Phys. Conf. Ser.* **2011**, *286*, 012027. https://doi.org/10.1088/1742-6596/286/1/012027.

(177) Janowitz, C.; Scherer, V.; Mohamed, M.; Krapf, A.; Dwelk, H.; Manzke, R.; Galazka, Z.; Uecker, R.; Irmscher, K.; Fornari, R.; Michling, M.; Schmeißer, D.; Weber, J. R.; Varley, J. B.; Walle, C. G. V. D. Experimental Electronic Structure of In$_2$O$_3$ and Ga$_2$O$_3$. *New J. Phys.* **2011**, *13* (8), 085014. https://doi.org/10.1088/1367-2630/13/8/085014.

(178) Mohamed, M.; Irmscher, K.; Janowitz, C.; Galazka, Z.; Manzke, R.; Fornari, R. Schottky Barrier Height of Au on the Transparent Semiconducting Oxide β-Ga$_2$O$_3$. *Appl. Phys. Lett.* **2012**, *101* (13), 132106. https://doi.org/10.1063/1.4755770.

(179) Vorwerk, C. W. Theoretical Spectroscopy of Ga_2O_3. Doctoral Thesis, Humbolt-Universität zu Berlin, Berlin, Germany, 2020.

(180) Vorwerk, C.; Sottile, F.; Draxl, C. All-Electron Many-Body Approach to Resonant Inelastic X-Ray Scattering. *Phys. Chem. Chem. Phys.* **2022**, *24* (29), 17439–17448. https://doi.org/10.1039/D2CP00994C.

(181) Weinhardt, L.; Benkert, A.; Meyer, F.; Blum, M.; Wilks, R. G.; Yang, W.; Bär, M.; Reinert, F.; Heske, C. Nuclear Dynamics and Spectator Effects in Resonant Inelastic Soft X-Ray Scattering of Gas-Phase Water Molecules. *J. Chem. Phys.* **2012**, *136* (14), 144311. https://doi.org/10.1063/1.3702644.

(182) Schwarz, K.; Neckel, A.; Nordgren, J. On the X-Ray Emission Spectra from FeAl. *J. Phys. F Met. Phys.* **1979**, *9* (12), 2509–2521. https://doi.org/10.1088/0305-4608/9/12/023.

(183) Schwarz, K.; Wimmer, E. Electronic Structure and X-Ray Emission Spectra of YS in Comparison with NbC. *J. Phys. F Met. Phys.* **1980**, *10* (5), 1001–1012. https://doi.org/10.1088/0305-4608/10/5/028.

(184) Blaha, P.; Schwarz, K.; Madsen, G. K. H.; Kvasnicka, D.; Luitz, J.; Laskowski, R.; Tran, F.; Marks, L. D. *Wien2k An Augmented Plane Wave Plus Local Orbitals Program for Calculating Crystal Properties User's Guide, WIEN2k_23.1*; 2023.

(185) Giannozzi, P.; Baroni, S.; Bonini, N.; Calandra, M.; Car, R.; Cavazzoni, C.; Ceresoli, D.; Chiarotti, G. L.; Cococcioni, M.; Dabo, I.; Dal Corso, A.; De Gironcoli, S.; Fabris, S.; Fratesi, G.; Gebauer, R.; Gerstmann, U.; Gougoussis, C.; Kokalj, A.; Lazzeri, M.; Martin-Samos, L.; Marzari, N.; Mauri, F.; Mazzarello, R.; Paolini, S.; Pasquarello, A.; Paulatto, L.; Sbraccia, C.; Scandolo, S.; Sclauzero, G.; Seitsonen, A. P.; Smogunov, A.; Umari, P.; Wentzcovitch, R. M. QUANTUM ESPRESSO: A Modular and Open-Source Software Project for Quantum Simulations of Materials. *J. Phys. Condens. Matter* **2009**, *21* (39), 395502. https://doi.org/10.1088/0953-8984/21/39/395502.

(186) Saad, Y.; Schultz, M. H. GMRES: A Generalized Minimal Residual Algorithm for Solving Nonsymmetric Linear Systems. *SIAM J. Sci. Stat. Comput.* **1986**, *7* (3), 856–869. https://doi.org/10.1137/0907058.

(187) Benedict, L. X.; Shirley, E. L. Ab Initio Calculation of $\varepsilon_2(\omega)$ Including the Electron-Hole Interaction: Application to GaN and CaF_2.

(188) Gražulis, S.; Daškevič, A.; Merkys, A.; Chateigner, D.; Lutterotti, L.; Quirós, M.; Serebryanaya, N. R.; Moeck, P.; Downs, R. T.; Le Bail, A. Crystallography Open Database (COD): An Open-Access Collection of Crystal Structures and Platform for World-Wide Collaboration. *Nucleic Acids Res.* **2012**, *40* (D1), D420–D427. https://doi.org/10.1093/nar/gkr900.

(189) McGuinness, C.; Stagarescu, C. B.; Ryan, P. J.; Downes, J. E.; Fu, D.; Smith, K. E.; Egdell, R. G. Influence of Shallow Core-Level Hybridization on the Electronic Structure of Post-Transition-Metal Oxides Studied Using Soft X-Ray Emission and Absorption. *Phys. Rev. B* **2003**, *68* (16), 165104. https://doi.org/10.1103/PhysRevB.68.165104.

(190) Benkert, A.; Meyer, F.; Hauschild, D.; Blum, M.; Yang, W.; Wilks, R. G.; Bär, M.; Reinert, F.; Heske, C.; Weinhardt, L. Isotope Effects in the Resonant Inelastic Soft X-Ray Scattering Maps of Gas-Phase Methanol. *J. Phys. Chem. A* **2016**, *120* (14), 2260–2267. https://doi.org/10.1021/acs.jpca.6b02636.

(191) Weinhardt, L.; Ertan, E.; Iannuzzi, M.; Weigand, M.; Fuchs, O.; Bär, M.; Blum, M.; Denlinger, J. D.; Yang, W.; Umbach, E.; Odelius, M.; Heske, C. Probing Hydrogen Bonding Orbitals: Resonant Inelastic Soft X-Ray Scattering of Aqueous NH_3. *Phys. Chem. Chem. Phys.* **2015**, *17* (40), 27145–27153. https://doi.org/10.1039/C5CP04898B.

(192) Weinhardt, L.; Fuchs, O.; Batchelor, D.; Bär, M.; Blum, M.; Denlinger, J. D.; Yang, W.; Schöll, A.; Reinert, F.; Umbach, E.; Heske, C. Electron-Hole Correlation Effects in Core-Level Spectroscopy

Probed by the Resonant Inelastic Soft x-Ray Scattering Map of C_{60}. *J. Chem. Phys.* **2011**, *135* (10), 104705. https://doi.org/10.1063/1.3633953.

(193) Lüning, J.; Rubensson, J.-E.; Ellmers, C.; Eisebitt, S.; Eberhardt, W. Site- and Symmetry-Projected Band Structure Measured by Resonant Inelastic Soft x-Ray Scattering. *Phys. Rev. B* **1997**, *56* (20), 13147–13150. https://doi.org/10.1103/PhysRevB.56.13147.

(194) Eich, D.; Fuchs, O.; Groh, U.; Weinhardt, L.; Fink, R.; Umbach, E.; Heske, C.; Fleszar, A.; Hanke, W.; Gross, E. K. U.; Bostedt, C.; v. Buuren, T.; Franco, N.; Terminello, L. J.; Keim, M.; Reuscher, G.; Lugauer, H.; Waag, A. Resonant Inelastic Soft X-Ray Scattering of Be Chalcogenides. *Phys. Rev. B* **2006**, *73* (11), 115212. https://doi.org/10.1103/PhysRevB.73.115212.

(195) Rubensson, J.; Petersson, L.; Wassdahl, N.; Bäckström, M.; Nordgren, J.; Kvalheim, O. M.; Manne, R. Radiative Decay of Multiply Excited Core Hole States in H_2O. *J. Chem. Phys.* **1985**, *82* (10), 4486–4491. https://doi.org/10.1063/1.448701.

(196) Ågren, H.; Luo, Y.; Gelmukhanov, F.; Jensen, H. J. Aa. Screening in Resonant X-Ray Emission of Molecules. *J. Electron Spectrosc. Relat. Phenom.* **1996**, *82* (1), 125–134. https://doi.org/10.1016/S0368-2048(96)03041-1.

(197) Skytt, P.; Glans, P.; Gunnelin, K.; Guo, J.; Nordgren, J.; Luo, Y.; Ågren, H. Role of Screening and Angular Distributions in Resonant X-Ray Emission of CO. *Phys. Rev. A* **1997**, *55* (1), 134–145. https://doi.org/10.1103/PhysRevA.55.134.

(198) Glans, P.; Skytt, P.; Gunnelin, K.; Guo, J.-H.; Nordgren, J. Selectively Excited X-Ray Emission Spectra of N_2. *J. Electron Spectrosc. Relat. Phenom.* **1996**, *82* (3), 193–201. https://doi.org/10.1016/S0368-2048(96)03065-4.

(199) Björneholm, O.; Nilsson, A.; Sandell, A.; Hernnäs, B.; Mrtensson, N. Determination of Time Scales for Charge-Transfer Screening in Physisorbed Molecules. *Phys. Rev. Lett.* **1992**, *68* (12), 1892–1895. https://doi.org/10.1103/PhysRevLett.68.1892.

(200) Marcinkevičius, S.; Speck, J. S. Electron-Phonon Scattering in β-Ga_2O_3 Studied by Ultrafast Transmission Spectroscopy. *Appl. Phys. Lett.* **2021**, *118* (24), 242107. https://doi.org/10.1063/5.0053845.

Acknowledgements

This dissertation would never exist without the mentorship, guidance, and support of many people around me.

I would like to thank Prof. Dr. Clemens Heske, for giving me the opportunity to work on this exciting research topic in the X-ray Spectroscopy group at KIT. Thank you for your mentorship, and all our discussions throughout the years.

I would also like to thank Prof. Tilo Baumbach, for agreeing to be my advisor from the Physics Faculty.

Thank you to Prof. Clemens Heske, Dr. Lothar Weinhardt and Dr. Dirk Hauschild for teaching me all about spectroscopy. Thank you for always being open to answer my questions, and for all of our discussions about my research work. Thank you for all your guidance about how to perform measurements, data analysis, how to best present my data, and what kind of research questions I should be asking not only you, but also myself, when I am evaluating my results. Thank you for always providing me with detailed and constructive feedback. I learnt a lot from all of you throughout the years and I am really grateful.

Thank you to Lothar and Dr. John Vinson for teaching me about DFT and BSE calculations. Thank you to Lothar for spending time and going through the Wien2k calculations with me, and thank you to John for explaining all the steps in OCEAN, so I could do the calculations. Thank you to John to continuing to work with me after your 2 months stay at KIT, and always answering my questions, no matter how trivial they were.

I would also like to thank Dr. Wolfram Witte and Dr. Dimitrios Hariskos, not only for preparing the solar cell samples, but also for your help and support in discussions of the paper draft, and of my conference presentations. Thank you to everyone in the EFFCIS II project for the fruitful discussions at the regular EFFCIS meetings. It was a great opportunity to see what other CIGSe research is done and to broaden my horizons, as well as to network with people.

I would like to thank everyone at the Spectroscopy group at KIT, for your support. Thank you to Dr. Constantin Wansorra for helping me with measurements in the laboratory and X-SPEC and for your great cleaving sample holder. :) Thank you to Dr. Ralph Steininger for all your support